Systematic Characterization of Catalytic Active Sites and Complete Catalytic Cycles for Methane to Methanol Transformation

by

Noor Md Shahriar Khan

A dissertation submitted to the Graduate Faculty of
Auburn University
in partial fulfillment of the
requirements for the degree of
Doctor of Philosophy

Auburn, Alabama
December 11, 2021

Keywords: quantum chemistry, C-H bond activation, methane to methanol transformation

Approved by

Evangelos Miliordos, Chair, J. E. Land Assistant Professor of Chemistry and Biochemistry
J. Vincent Ortiz, Ruth W. Molette Professor of Chemistry and Biochemistry
Konrad Patkowski, Professor of Chemistry and Biochemistry
Byron H. Farnum, Assistant Professor of Chemistry and Biochemistry
Stuart Loch, Professor of Physics

Abstract

Methane to methanol (MTM) transformation is a very significant chemical transformation for its scientific, industrial, and commercial importance. Currently, MTM transformation is done by following a high energy procedure which is economically viable only in a large industrial scale. Despite of a search of half a century, an effective low energy MTM transformation is still formidable and active research is ongoing in search of that holy grail. In this project, we have employed high-level electronic structure theory calculations to elucidate some of the profound complexities of MTM transformation and theoretically investigated a new complete catalytic cycle for MTM transformation.

Transition metal oxides have attracted considerable attention for their catalytic potency for MTM transformation. Specially FeO and its charged variants have been considered the best potential candidates for MTM transformation because of their presence in the biocatalytic active sites for MTM transformation. To provide a deeper understanding of its catalytic activity at the electronic structure level, we have studied the ground and excited states FeO^{2+} using high-level electronic structure theory. The ground electronic state of FeO^{2+} is $^3\Delta$ which is of oxyl character followed by the low-lying excited states $^5\Delta$ and $^5\Sigma^+$ which have oxo electronic configuration. Then we have introduced ligands in the system and found that the strong field ligands such as NH_3 stabilize both the oxo and oxyl states whereas the weak field ligands such as H_2O has stabilized only the oxo states. For the methane activation mechanism, the oxo states undergo oxidative addition route and oxyl states follow the radical mechanism. So, it is possible to direct the reaction mechanism by the choice of ligands coordinating the catalytic active site.

2

We have also investigated the ground and excited states of a second-row transition metal oxide dication, RhO^{2+} using electronic structure theory and found that the ground state is $^2\Pi$ which is of oxo character. RhO^{2+} coordinated by four NH_3 ligands has exceptionally low activation barrier (13.6 kcal/mol) for MTM transformation because of the rearrangement of electronic configuration.

One of the prominent limitations of the MTM transformation using transition metal oxide catalysts is the selectivity issue that means the product methanol is more susceptible to further oxidation that causes over oxidation of methanol and catalyst poisoning. To address this limitation, we have studied a new complete catalytic cycle for MTM transformation using metal methoxide as a catalyst. At first, we have employed $FeOCH_3^+$ as a catalyst and used N_2O as an oxidant. This combination of catalyst and oxidant has produced a promising energy landscape for MTM transformation. Then we have further optimized the catalytic cycle by incorporating ligands with the active site $((NH_3)_4FeOCH_3^{2+})$ and using a more potent oxidant (O_3). Also, a comparison of the C-H bond activation energy between methane and methanol is studied for the complete catalytic cycle. The presence of four NH_3 ligands has destabilized the methanol activation channel and the activation barrier of the C-H bond activation of methanol is found higher than the C-H activation of methane.

Acknowledgement

First, I would like to place my sincere gratitude to my Ph.D. supervisor, Dr. Evangelos Miliordos, for his ceaseless support in the entire course of my Ph.D. research for the last five years. It has been an exciting journey for me only because of his excellent research ideas and his patience has allowed me to think about and solve difficult research questions. In my future research career, he will be the greatest source of motivation.

Second, I would like to thank my Ph.D. committee members: Prof. Vincent Ortiz, Prof. Konrad Patkowski and Asst. Prof. Byron Farnum for their consistent guidance and research ideas towards the fulfilment of this project.

Also, I am grateful to Auburn University for the financial assistance and Auburn University HOPPER cluster, Alabama Supercomputer Center for the computational facility.

In this journey, I have received tremendous support from my wife Tasnuba Hasin and my beloved parents. I believe, I couldn't have achieved anything without their sacrifice and encouragement. I am blessed to have them in my life.

Table of Contents

Appendix A Supporting Material for Chapter 2

Appendix B Supporting Material for Chapter 3

List of Figures

8

<h1 style="text-align:center">List of Tables</h1>

Chapter One

1. Computational Chemistry

Computational Chemistry refers to the general term for the study of chemical problems by using any form of computing. The root of computational chemistry lies in physics (quantum mechanics) and mathematics. By using the techniques of computational chemistry, it is possible to predict molecular properties, compare with experimental results, explain ambiguous experimental data, and model unstable intermediates such as transition states which are beyond experimental observations.

The roots of computational chemistry can be traced back in the beginning of 1928 when the theoretical physicists attempted to solve the Schrödinger equation using primitive calculating machines. Then by 1950s, two factors, namely the advent of digital computers and the application of numerical approximations to the solution of Schrödinger equation, allowed the scientists to produce highly accurate quantitative data regarding the chemical behavior of molecules. By the end of the last century, the field of computational chemistry has witnessed revolutionary expansion in terms of the scope and capability. The rise of computing powers and better approximations allowed us to expand the application of computational chemistry in drug design, bio-catalytic reactions, and catalysis which incorporates thousands of atoms.

In the next section, I provide a brief description of the methods at the fundamental level and this account doesn't serve as a complete/detailed description of the methods since there are numerous more complete accounts such as *Modern Quantum Chemistry* by Szabo and Ostlund.

1.1 Electronic Structure Theory

Quantum Chemistry is the specific area of computational chemistry for which the methods stem from the basic principles of quantum mechanics (Schrödinger equation). The concept of quantum chemistry is divided into two broad areas-

1. Methods which treat the nuclei of a molecule as fixed/stationary particles with respect to the movement of electrons. As these methods primarily deal with the electronic motion so it is called the electronic structure theory.

2. Methods those can model the molecular behavior with respect to time. These chemical dynamical methods consider the motions of both electrons and the nuclei. The laws of quantum dynamics, molecular dynamics (Newtonian mechanics) or a combination (semiclassical dynamics) are the bedrocks for these methods.

All the areas of quantum chemistry can be further divided into two more branches namely method development and application. One of the prime goals of the electronic structure theory is to solve the non-relativistic time independent Schrödinger equation (Eq 1.1) which sits in the heart of the electronic structure theory.

$$\hat{H}|\Psi\rangle = E|\Psi\rangle \qquad (1.1)$$

Where, $\hat{H}$ is the Hamiltonian operator for many particles system, Ψ is the wavefunction that depends on the position and spin variables of the particles and E is energy of the system.

The Hamiltonian operator can be written as the summation of kinetic and potential energy terms of the system. Consider the following system (Figure 1.1) with two nuclei (A and B) and two electrons (i and j) where $\vec{R}_A$, $\vec{R}_B$, $\vec{r}_i$, and $\vec{r}_j$ are the position vectors of them respectively.
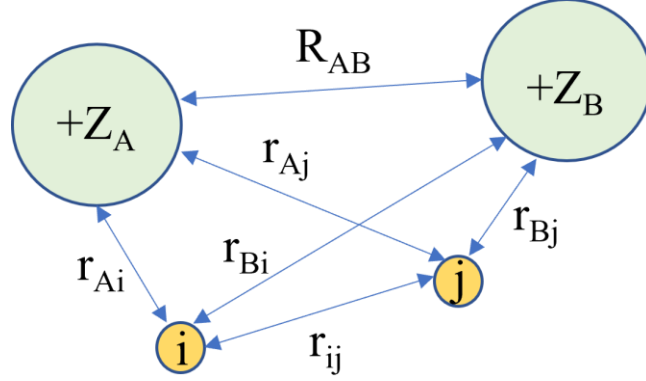
Figure 1.1: A system with two nuclei and two electrons. The distance between i and j electron is $r_{ij} = |\vec{r}_i - \vec{r}_j|$, and the distance between A and B nuclei is $R_{AB} = |\vec{R}_A - \vec{R}_B|$

In general, the Hamiltonian terms can be written as (Eq 1.2)-

$$\hat{H} = \hat{T}_N (\vec{R}) + \hat{T}_e (\vec{r}) + \hat{V}_{eN} (\vec{r}, \vec{R}) + \hat{V}_{ee} (\vec{r}) + \hat{V}_{NN} (\vec{R}) \qquad (1.2)$$

Where, $\hat{T}_N (\vec{R})$ is the kinetic energy of the nuclei, $\hat{T}_e (\vec{r})$ is the kinetic energy of the electrons, $\hat{V}_{eN}$ $(\vec{r}, \vec{R})$ is the electron-nuclear attraction, $\hat{V}_{ee} (\vec{r})$ is the electron-electron repulsion and $\hat{V}_{NN} (\vec{R})$ is the nuclear-nuclear repulsion. $\vec{R}$ and $\vec{r}$ are the position vectors of the nuclei and electrons respectively.

Nuclei are more massive than electrons and a very first approximation of a system can be the assumption that due to the differences of masses, the nuclear motion and the motion of the electrons can be decoupled. This approximation which is called the Born-Oppenheimer approximation, allows us to consider the nuclear motion and the motion of the electrons separately under which we can eliminate the nuclear kinetic energy term ($\hat{T}_N (\vec{R})$) from the Hamiltonian (Eq 1.2) and consider the nuclear-nuclear repulsion term, $\hat{V}_{NN} (\vec{R})$ a constant. With the help of the Born-Oppenheimer approximation we can focus on the electronic part of the Schrödinger equation (Eq 1.1) with electronic Hamiltonian and electronic wavefunction (Eq 1.3)-

$$\hat{H}_{elec}\Phi_{elec} = E_{elec}\Phi_{elec} \tag{1.3}$$

The total energy E_{tot}, which is the addition of E_{elec} plus the nuclear-nuclear repulsion term $\hat{V}_{NN}$ $(\vec{R})$, provides a potential for the motion of the nuclei. We can construct a potential energy surface (PES) using the E_{tot} as a function of the position of nuclei $(\vec{R})$. Figure 1.2 depicts a one-dimensional PES that is called potential energy curve (PEC).
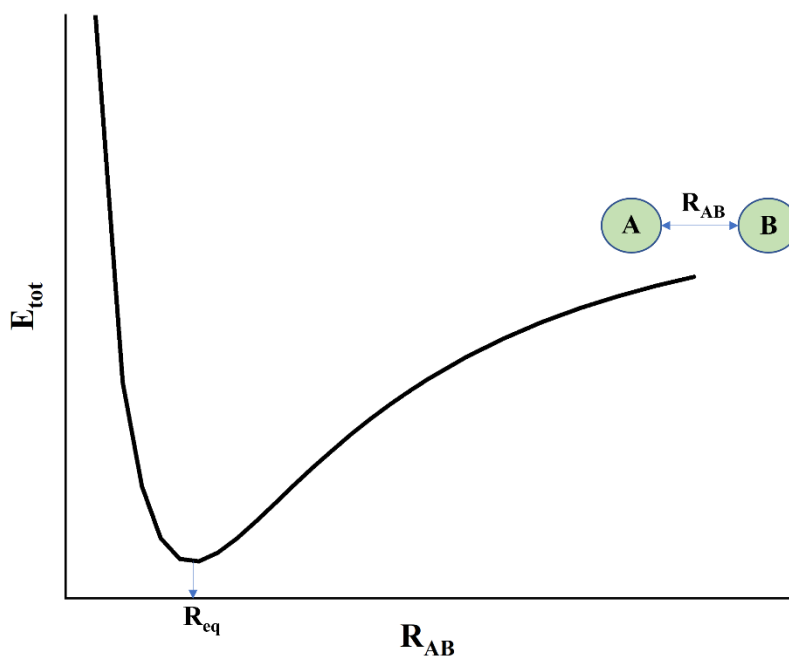
Figure 1.2: Representative diagram of PEC where the energy is a function of the nuclear distances (R). R_{eq} is the equilibrium bond distance for the nuclei A and B.

This representation of PECs can be extended to multi-dimensional PES for polyatomic systems and using two- or three-dimensional plots, it is possible to elucidate the reactivity of chemical reactions. Local or global minima and saddle point on a PES can be interpreted as reactant/product and transition state respectively. For example, figure 1.3 presents two and three-dimensional PES for the oxidation reaction of ethylene (C_2H_4) with iodosobenzene (C_6H_5IO). The

PESs present quantitative idea about the reaction energy and activation barrier.[1] One of our goals in the catalysis project (see chapter 2 & 3) is to identify such reactant, product and transition state to explain the reactivity of the system.
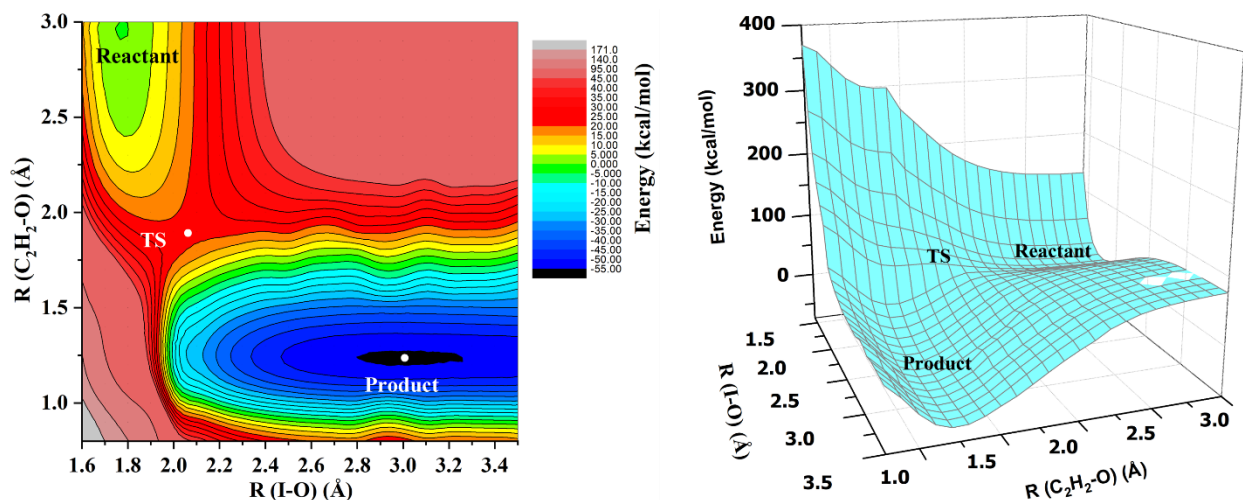
Figure 1.3: Two (left) and three-dimensional (right) PES for the oxidation reaction of ethylene with iodosobenzene.

1.2 Hartree-Fock Method

The accuracy as well as the complexity of the electronic structure theory depends on the methods of writing the electronic wavefunction. The simplest method of the electronic structure theory is the Hartree-Fock (HF) method where the wave function is written in terms of a Slater determinant. Consider a case of a closed shell system (S=0) with four electrons. For the HF

method, the wave function in terms of Slater determinant will be a four-by-four determinant as shown below-

$$\Psi = 1/\sqrt{4!} \begin{vmatrix} \psi_1(1)\alpha(1) & \psi_1(1)\beta(1) & \psi_2(1)\alpha(1) & \psi_2(1)\beta(1) \\ \psi_1(2)\alpha(2) & \psi_1(2)\beta(2) & \psi_2(2)\alpha(2) & \psi_2(2)\beta(2) \\ \psi_1(3)\alpha(3) & \psi_1(3)\beta(3) & \psi_2(3)\alpha(3) & \psi_2(3)\beta(3) \\ \psi_1(4)\alpha(4) & \psi_1(4)\beta(4) & \psi_2(4)\alpha(4) & \psi_2(4)\beta(4) \end{vmatrix}$$

Where the indices correspond to the electrons and ψ and α/β are the spatial and spin functions shared by the four electrons. The Slater determinants also incorporate a normalization constant which is $1/\sqrt{N!}$ (N is the number of electrons). Each component of the Slater determinant is called the spin orbital which comprises of spatial function and spin function. The spatial orbitals ψ_i can be written as a linear combination of basis functions (Eq 1.4).

$$\psi_i = \sum_{\mu=1}^{K} C_{\mu i} \Phi_\mu \tag{1.4}$$

Where K is the number of basis functions, $C_{\mu i}$ is the coefficient and Φ_μ is the basis function. The basis functions are atom centered Slater-type or Gaussian functions which are known (designed) but the unknowns are the coefficients ($C_{\mu i}$) and the objective is to optimize these coefficients.

Using HF method, the energy of a system can be obtained by utilizing the variational principle with the following equation (Eq 1.5)-

$$E_{HF} = \frac{\int \Psi^* \hat{H} \Psi \, d\tau}{\int \Psi^* \Psi \, d\tau} \tag{1.5}$$

Where, Ψ and Ψ^* is the wave function and the complex conjugate of the wave function and dτ is the integration over all space considering all electronic coordinates and spin variables. The introduction of basis set converts the complex differential equation to an algebraic problem which can be solved readily by using modern computers.

In the HF method, only one electronic configuration (one Slater determinant), which is often the ground state of the system, is considered to construct the wavefunction. For this limitation, HF is known to be unable to account accurately for the interaction between the electrons (electron correlation energy). The difference of the energy between the exact solution of the nonrelativistic Schrödinger equation and the HF energy is called the correlation energy. Figure 1.3 depicts the hierarchy of methods towards the exact energy.
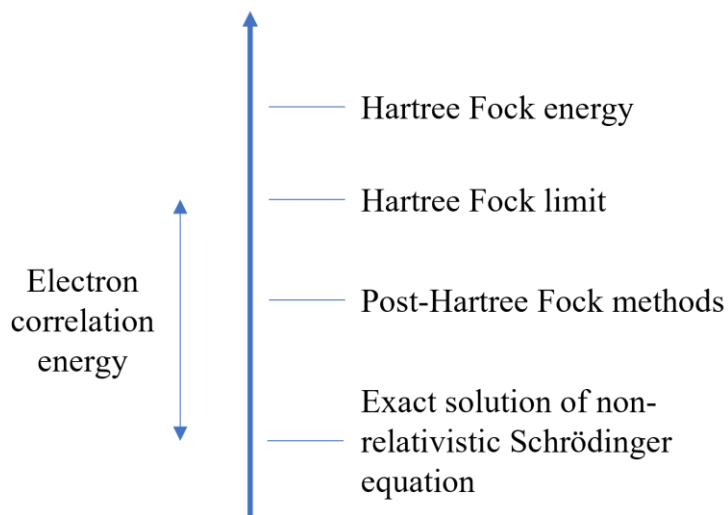
Figure 1.4: Electron Correlation Energy

It is required to go beyond HF method (post-HF methods), to capture the electron correlation energy. Two of the post-HF methods are Complete Active Space Self-Consistent Field

(CASSCF) and Multireference Configuration Interaction (MRCI). Unlike HF methods, in these methods a linear combination of determinants (electronic configurations) is used to construct the wavefunction. Incorporation of multiple electronic configurations allow the methods to account for the so-called static (CASSCF) and dynamic (MRCI) electron correlation energy of the system.

1.3 Post Hartree-Fock Methods

CASSCF and MRCI are the examples of two conceptually simple post HF methods which can account for the electron correlation energy. These methods are also termed as multi-reference methods as they utilize a linear combination of multiple electronic configurations to construct the wavefunction. To study systems which contains transition metals, usually have low lying excited states, and to precisely model the dissociation of a chemical bond, these multireference methods are the most appropriate techniques of electronic structure theory.

In CASSCF, the orbitals are divided into three groups namely closed, active, and virtual (figure 1.5). The closed orbitals ($\psi_1, \psi_2,$ and ψ_3) of a system are the core orbitals which kept frozen (always doubly occupied). But in the active orbitals (usually comprised of occupied and unoccupied orbitals in the HF determinant such as $\psi_4, \psi_5, \psi_6,$ and ψ_7), every possible occupation of electrons (0, 1, or 2) are considered and each of the substitution produces one distinct electronic configuration. A linear combination of these electronic configurations (determinants) is used to construct the wavefunction in CASSCF. In CASSCF, not only the molecular orbitals but also the weight of every determinant is optimized. The virtual orbitals are the unoccupied orbitals ($\psi_8, \psi_9,$ and *beyond*) and the promotion of electrons in the virtual orbitals is excluded in the CASSCF wavefunction but it is included at the MRCI level. For that reason, MRCI has more determinants

in the linear combination to construct the wavefunction than CASSCF hence computationally more demanding and performs better to account electron correlation. But MRCI is not size extensive, which means, for two isolated system A and B, energy of the system A and energy of the system B is not additive for the combined system (A+B). In terms of equation, $E(A) + E(B) \neq E(A+B)$ where $E(A)$, $E(B)$, and $E(A+B)$ stands for the energy of system A, energy of system B and energy of the combined system (A+B) respectively. To minimize this size extensivity error, correction to the MRCI method is used which is known as Davidson Correction (MRCI+Q).
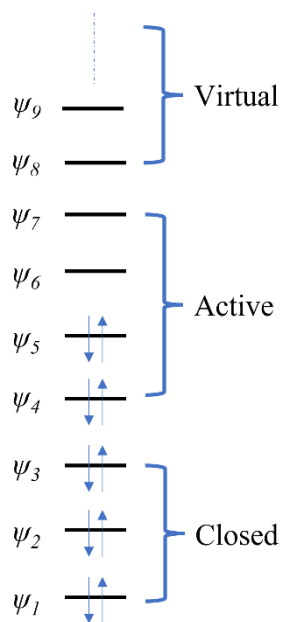
Figure 1.5: General representation of a typical grouping of orbitals for CASSCF method

There is other widely used post-HF methods such as MP2, Coupled Cluster (CC). The MP2 method utilizes many-body perturbation theory and the wavefunction is constructed with higher order perturbation (second order for MP2) to the ground state/reference wavefunction (HF). In the CC method, HF wavefunction is used as the reference wavefunction and electron correlation is

incorporated by constructing the wavefunction using an exponential cluster operator. The method CCSD accounts only the single and double electronic substitution whereas CCSD(T) approximates the triple substitution perturbatively. CCSD(T) is termed as the golden standard of electronic structure theory.

1.4 Density Functional Theory

Apart from the wavefunction based methods, other philosophy such as the Density Functional Theory (DFT) is a very popular method because of its ease of application. DFT assumes an exact/direct correspondence between the electronic density and the energy (functional) of a given system and optimization of the electronic density is done by minimizing the energy. The exact functional is unknown and different forms have been suggested in the literature. As a result, the method is often characterized as semi-empirical which is not as accurate as the previous methods but the advantage of DFT is it allows the calculation of larger systems.

1.5 Outline of the Following Chapters

Chapter 2 is organized with the ground and excited states calculations of transition metal oxide dications. First, we have presented a detail study of the electronic structure of FeO^{2+}. Then we have introduced ligands (NH_3, H_2O) in the system to study the ligand field effects on the electronic states of FeO^{2+}. Second, we have calculated the ground and excited states of RhO^{2+}, which is a second-row transition metal oxide dication. Then we have studied the C-H activation of CH_4 using RhO^{2+} as a catalytic active site in coordination with (1-5) NH_3 ligands.

Chapter 3 is the representation of a complete catalytic cycle for MTM transformation using $FeOCH_3^+$ as a catalyst and N_2O as an oxidant. This catalytic cycle is further optimized by introducing ligands in the system and using O_3 as an oxidant. Finally, the C-H bond activation energy for methane and methanol is compared to address the selectivity issue.

Chapter Two

2. Electronic Structure of the Transition Metal Oxide Active Sites, Ligand Field Effects, and Their Potency to Activate C-H Bonds

Transition metals and their oxides are prominent catalytic active sites for numerous chemical reactions. Specifically, the metal-oxo (MO^{2+}) units of the first-row transition metals have been found instrumental for the activation of C-H bonds of organic molecules.[2-10] To harness the catalytic power of the transition metal oxide active units, laboratory synthesis of the first-row transition metal oxides are common[11-16] due to their low-cost and availability.

In natural/biological systems, especially in enzyme driven catalytic reactions, transition metal-oxides act as the active site. Higher oxidation states of the metal such as metal-oxo (MO^{2+}) units serve as reaction intermediates and they are stabilized by the presence of bulky ligands.[17] The effect of ligands on the metal-oxide active site depends on the electronic structure of the species. Meticulous research is done on the electronic structure of the ground and low-lying excited states for the first-row transition metal-oxides considering neutral, anion, and cation using high level quantum mechanical calculations.[18-27] Also, the effect of ligands on the electronic structure of the metal-oxides and their role in the mechanism of the activation of chemical bonds have been elucidated in theoretical explorations.[28-32] But unfortunately, in depth knowledge on the electronic structure of transition metal-oxide di-cation is sporadic in both theoretical and experimental front.[33-38]

A recent publication on the theoretical study of the ground and excited states of the first-row transition metal oxide di-cations has provided a solid theoretical understanding in terms of their electronic structures.[39] This article has also shed light on the catchphrase 'oxo wall' for the inorganic community.[40] The di-cationic unit of the metal oxide (MO^{2+}) can be in two forms namely metal-oxo ($M^{4+}O^{2-}$) or metal-oxyl ($M^{3+}O^-$). For the oxyl form, the oxygen terminal has at least one unpaired electron thus very reactive and relatively less stable than the oxo form for the early transition metals. This stability of the oxo species is present until Fe in the periodic table and replaced by stable oxyl form for the heavier metals. Hence the term coined as 'oxo wall' placed in between Fe and Co.[40] The oxo form usually undergoes two mechanism namely oxidative addition (OA) and proton coupled electron transfer (PCET). On the other hand, the oxyl form performs radical abstraction (hydrogen atom transfer or HAT) with a low activation barrier.[40]

Because of its role in the reaction mechanism, the oxo and oxyl form demands conceptual clarity. It can be simply explained by utilizing molecular orbitals of the involved metal oxide. For the neutral transition metal oxides, the most contributing valence orbitals are five d and three p orbitals of the metal and oxygen respectively. Figure 2.1 depicts typical contours of these eight molecular orbitals namely σ, π (bonding and anti-bonding) and δ (non-bonding). However, the remaining valence orbital 4s, is omitted (not populated in di-cations) and almost always polarized on the metal. Oxygen, due to its higher electronegativity, is electron rich and polarize the molecular orbitals except the δ orbitals which are non-bonding. The effect of this polarization is often denoted as ($M^{2+}O^{2-}$) picture for the neutral metal oxides (MO). For the cationic species (MO^+), for which one electron is removed from MO, it is more favorable to eject one electron form the metal terminal specifically from the pure metallic orbitals (4s or δ) rather than from the oxygen terminal due to the lower ionization energy of the metals (6.56 – 7.73 eV for first row transition metal vs. 13.62

eV for oxygen).[41] For neutral and cationic transition metal oxides, the current scenario prevails, and oxygen always remains electron rich which favors the oxo form. But, for the di-cationic species, second ionization of the metal is required which is very high in energy from the metal terminal. Instead, ionization form the π orbitals (polarized toward oxygen) might be more favorable. Indeed, the theoretical calculations reveal that for the early transtion metal oxide di-cation prefers the second ionization from pure metallic orbitals (oxo form) whereas the late transition metals chose to liberate one unpaired electron on the oxygen terminal (oxyl form). Fe sits on the border with competetive oxo and oxyl caracters.[39]
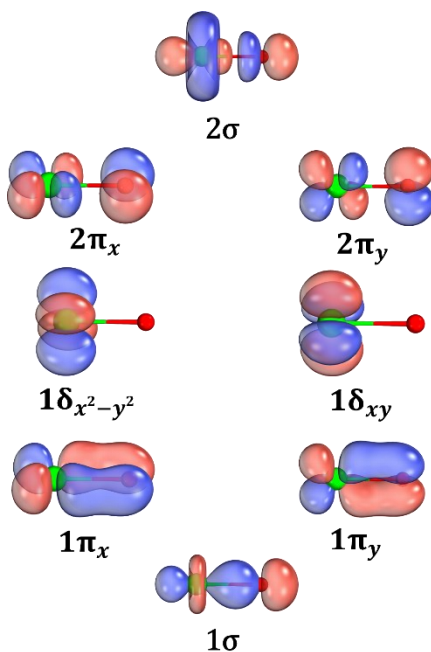
Figure 2.1: Typical molecular orbital contours for RhO^{2+} (Green ball=Rh, Red ball=oxygen)

In this chapter, the electronic structure of the ground and low-lying excited states for FeO^{2+} and RhO^{2+} is presented to demnostrate the difference between first and second row transition

metals and to account their catalytic potency, a model case of C-H activation mechanism followed by methane to methanol transformation is performed incorporating with the effects of ligands on these dicationic species. The choice of Fe and Rh is also explained in the respective section.

2.1 Ligand Field Effects on the Ground and Excited States of Reactive FeO^{2+} Species

2.1.1 Rationale Behind the Choice of FeO^{2+}

Selective functionalization of the C-H bond is regarded as still illusive but very demanding process for numerous inductrial applications.[42-45] Although, nature has developed a series of heme and non-heme enzymes with metal oxo active sites for the controlled oxidation of organic materials. Mono and dineuclear iron act as the active sites which form iron oxo intermediates to activate strong C-H bonds.[46-48] As an example, high valent Fe(IV)-oxo intermediates from α-ketoglutarate dependent taurine dioxygenase (TauD)[49, 50] and syringomycin halogenase (SyrB2)[51, 52] cleaves the C-H bond by hydrogen atom abstraction. Following nature, a variety of non-heme model complexes are prepared in laboratory with characterizing Fe(IV)-oxo intermediates.[53-57] Also, these reactive intermediates have been stabilized in the coordination environment of metal organic frameworks (MOFs) and zeolites with excellent catalytic activity for methane and ethane functionalization.[58-62] For the neutral species, the high spin (S=2) Fe(IV)-oxo form is more stable and the stability is attributed to the presence of ligands in the system.[60, 62-64] On the other hand, the synthetic model complex prefers an intermediate spin (S=1).[53, 57, 65]

In this section, we present detailed electronic structure calculations of the bare FeO^{2+} to reveal the electronic structure of the ground and excited states of the titled species. Also, the effect of strong and weak field ligands on the ground and low-lying excited states is assessed with state-of-the-art quantum mechanical calculations.

2.1.2 Computational Details

For FeO^{2+}, three spin multiplicities namely triplet, quintet, and septet (S=1, S=2, and S=3 respectively) are considered for the construction of the potential energy curves (PECs). At first, state average calculations utilizing complete active space self-consistent field (CASSCF)[66, 67] are performed to generate the reference wave function for the ground and low-lying excited states using C_{2v} symmetry (the largest Abelian subgroup of the original $C_{\infty v}$ symmetry of the molecule). The active space is chosen as 4s, 3d orbitals of Fe and 2p orbitals of O. To tackle the convergence issues and correct dissociation of the PECs, a second set of d orbital is included in the active space, but it didn't change the morphology of the PECs around the equilibrium. In total, there are 10 electrons in 14 orbitals and every possible electronic configuration is allowed within this active space. Then using the reference wave function (CASSCF), multi reference configuration interaction (MRCI)[68, 69] calculations are done for the ground and low-lying excited states. Excitation from the 2s orbital of O is excluded at the CASSCF level because for all the electronic states it is almost always doubly occupied but it is included for electron correlation at the MRCI level. For these calculations, quintuple ζ quality basis set (cc-pV5Z for Fe and aug-cc-pV5Z for O)[70, 71] is used for the PECs around the equilibrium. An augmented basis set is used for O to account the bond polarization. But, to construct the full PECs, and for the mono coordinated

species $NH_3(FeO)^{2+}$, and $H_2O(FeO)^{2+}$, a triple ζ basis set is used. These multi reference calculations are performed using MOLPRO[72] electronic structure package.

2.1.3 Summary of the Results and Discussion

In the section most important findings reported in the following paper[73], provided in Appendix A, are summarized. Reprint is done with the permission form the Royal Society of Chemistry.

J. K. Kirkland, **S. N. Khan**, B. Casale, E. Miliordos and K. D. Vogiatzis, *Phys. Chem. Chem. Phys.*, 2018, **20**, 28786 **DOI:** 10.1039/C8CP05372C.

Molecular Orbitals and Reaction Channels

Considering C-H activation with FeO^{2+}, four possible reaction channels are considered based on the spin state of Fe(IV)-oxo and the molecular orbital that overlaps with the C-H bond for hydrogen abstraction. Regarding the electronic structure, not only the ground state but also the excited states have significant role for these reaction channels. The evolution of $Fe^{4+}O^{2-}$ (oxo) to $Fe^{3+}O^-$ (oxyl), that happens upon the elongation of the Fe-O bond, reveals a different C-H activation mechanism. The valence molecular orbitals (σ, π, δ, π^*, σ^*) of the Fe-O unit are shown in figure 2.2. In total, four possible reaction channels are considered depending on the spin of the Fe(IV)-oxo moiety (S = 1 or 2) and the molecular orbital (MO) populating σ^*, termed as $^5\sigma$, $^5\pi$, $^3\sigma$, and $^3\pi$. Figure 2.3 presents all four mechanisms with MO diagrams. For near-trigonal pyramidal field, both δ and π^* orbitals are degenerate hence can accommodate four unpaired electrons in δ,

and π^* orbitals which in turn favors $^5\sigma/^5\pi$ mechanisms. Whereas in near-octahedral field, only the

π^* orbitals are degenerate, so it favors the triplet spin multiplicity and promotes $^3\sigma/^3\pi$ mechanisms.
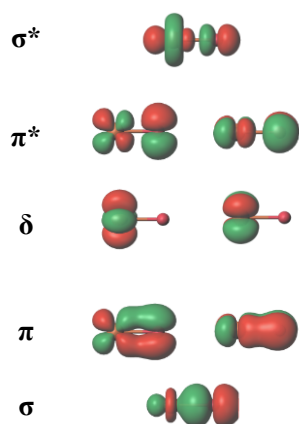
Figure 2.2: Valence molecular orbitals of bare FeO^{2+} ($R_{Fe-O} = 1.64$ Å).
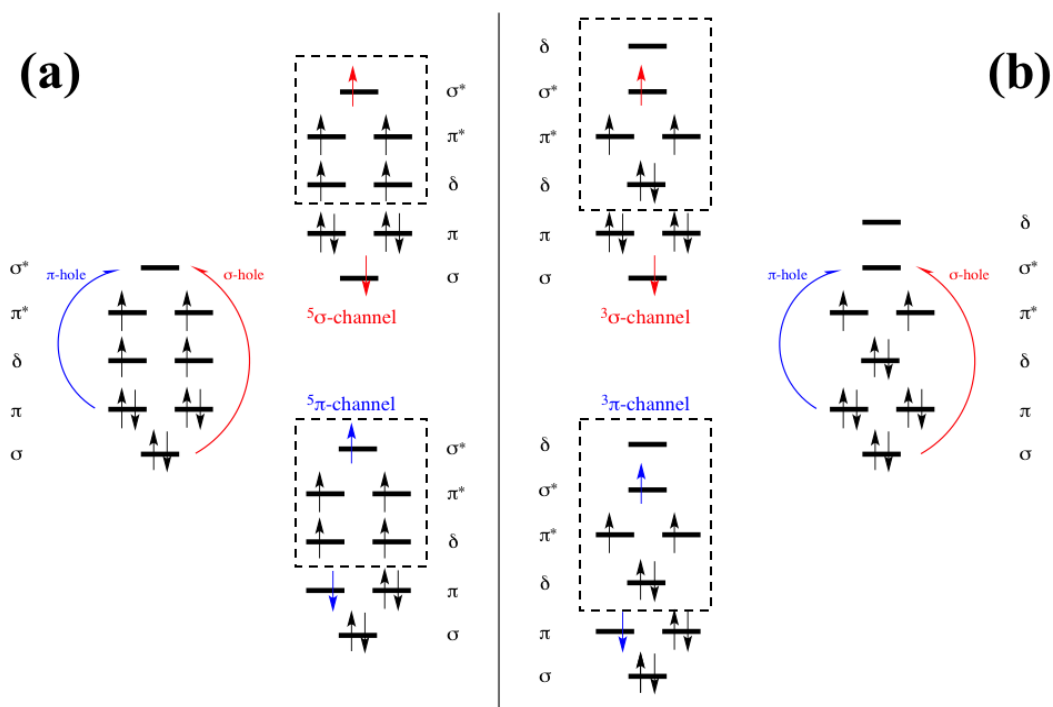
Figure 2.3: Molecular orbital diagram for (a) high-spin S = 2 Fe(IV)-oxo species in a near-trigonal pyramidal field and (b) intermediate-spin S = 1 Fe(IV)-oxo species in a near-tetragonal pyramidal field. Curvy arrows show the electron transferred upon Fe-O bond elongation for the formation of the Fe(III)-oxyl species that promote the hydrogen atom abstraction via (a) the $^5\sigma$ and $^5\pi$ channels and (b) the $^3\sigma$ and $^3\pi$ channels. Orbitals inside the dashed-line boxes have predominant iron character.

Bare and mono coordinated FeO^{2+}

The first two ionization energies of iron are 7.90 eV [Fe(^{5}D)→Fe$^+$(^{6}D)] and 16.19 eV [Fe$^+$(^{6}D)→Fe^{2+}(^{5}D)],[74] while for oxygen they are 13.62 eV [O(^{3}P)→O$^+$(^{4}S)] and 35.12 eV [O$^+$(^{4}S)→O^{2+}(^{3}P)].[74] These values set the lowest dissociation channel as Fe$^+$(^{6}D) + O$^+$(^{4}S) followed by Fe^{2+}(^{5}D;d^6) + O(^{3}P) at 2.57 eV. This energy range fits eight excited electronic states of Fe$^+$,[75]

but none for O^+. All $Fe^+ + O^+(^4S; 2s^2 2p^3)$ asymptotes generate dissociative PECs, and considering a $1/R(Fe-O)$ repulsion the $Fe^+ + O^+$ energies increase by as much as 1.44 eV at 10 Å. At the same distance, the $Fe^{2+} + O$ fragments interact only weakly. Thus, the $Fe^+(^6D) + O^+(^4S)$ and $Fe^{2+}(^5D; d^6)$
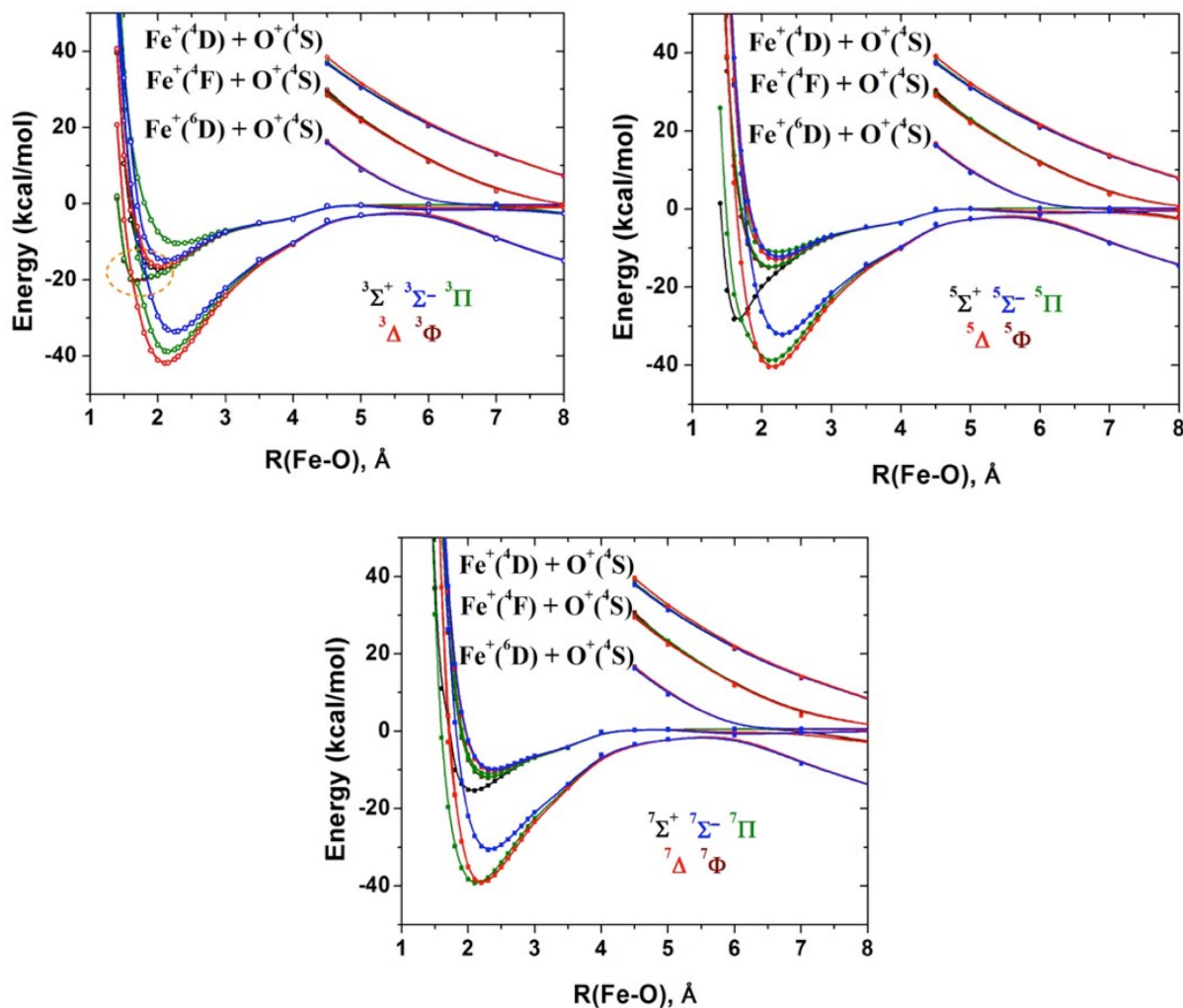
Figure 2.4: PECs for triplet (top left), quintet (top right), and septet (bottom) electronic states of FeO^{2+}.

$+ O(^3P)$ asymptotes approach to $2.57 - 1.44 = 1.13$ eV, which means that only three $Fe^+ + O^+$ channels are lower than $Fe^{2+} + O$ at 10 Å. All states (32 triplets, quintets, and septets) of these four channels are included in our PECs of Figure 2.4 which cover Fe-O distances shorter than 8 Å.

Applying further this simple model, the $Fe^+(^6D) + O^+(^4S)$ and $Fe^{2+}(^5D; d^6) + O(^3P)$ asymptotes are expected to cross at $1/R(Fe-O) = 2.57$ eV which yields $R(Fe-O) = 5.6$ Å. Indeed, our PECs present an avoided crossing region at 5.5-6 Å. Setting the zero of the energy scales equal to that of $Fe^{2+}(^5D) + O(^3P)$, the lowest energy fragments $Fe^+(^6D) + O^+(^4S)$ are at -2.57 eV = -59.3 kcal/mol. In the same scale the equilibrium energy of the ground $^3\Delta$ state is -42 kcal/mol (see figure 2.4) and -10 kcal/mol for our highest state ($^3\Pi$). Therefore, all equilibrium energies are lower than the $Fe^{2+} + O$ fragments but higher than the $Fe^+ + O^+$ ones, which means that bare FeO^{2+} is thermodynamically unstable, but kinetically stable because of the large dissociation barriers.

The PECs exhibit additional features. Specifically, the $^5\Sigma^+$ state of figure 2.4 follows its sister states for distances longer than 2.5 Å (same dissociation channel) and tending to form a minimum at 2.2 Å. It deviates though creating a minimum at 1.64 Å. Similar minima are found for $^3\Phi$ and $^3\Sigma^+$ which undergo an avoided crossing right at the region of their 1.6 Å minima with PEC of lower states (see the encircled region of figure 2.4 top left). Finally, $^5\Pi$ reveals a shoulder at the same distance (see figure 2.4 top right), which turns out to create gradually a clear minimum in the presence of ligands. Indeed, we added an ammonia or water ligand to the $[FeO]^{2+}$ diatomic and constructed the PECs in the Fe-O equilibrium region for the lowest quintet states ($^5\Sigma+$, $^5\Pi$, $^5\Delta$). The $[FeO(H_2O)]^{2+}$ and $[FeO(H_3N)]^{2+}$ structures were fully optimized at the MRCI level for the $^5\Sigma^+$ and then scanned over the Fe-O distance by keeping all other geometrical parameters fixed. The potential energy curves are shown in figure 2.5. In comparison to bare $[FeO]^{2+}$, the $^5\Sigma^+$ minimum (black line) is stabilized with the addition of a water molecule (weak ligand field), and even more so with an ammonia molecule (strong ligand field). The same is true for the shoulder of $^5\Pi$ which splits into two components due to symmetry lowering. In the case of ammonia, one of the $^5\Pi$ components becomes a very shallow local minimum. It is these minima that stabilize further upon

the addition of more ligands generating the ^5A and ^5E states (see the article).[73] Overall, the $^5\Sigma^+$ and $^5\Pi$ states have a Fe(IV)-oxo character at R(Fe-O)~1.6 Å which switches to Fe(III)-oxyl at R(Fe-O)~2.25 Å. This transition occurs at about 1.8 Å. Additionally, The Fe(IV)-oxo region is stabilized over the Fe(III)-oxyl region when adding a ligand, and this stabilization is larger for ammonia than water.
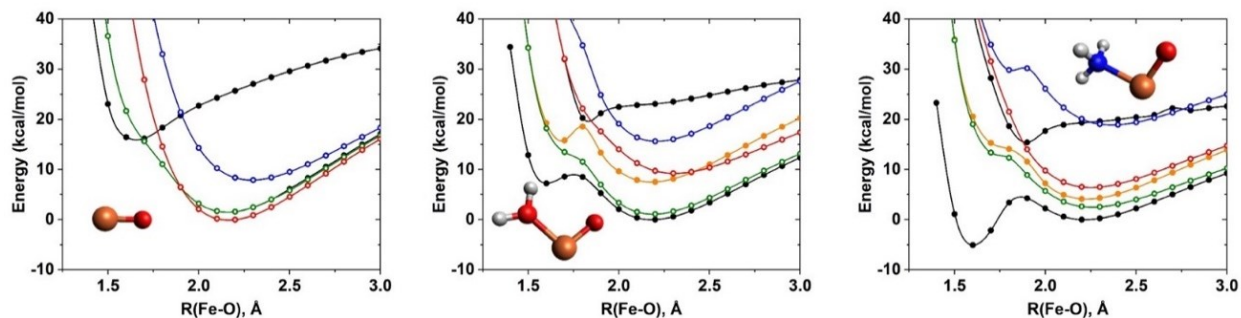
Figure 2.5: MRCI PECs for $[FeO]^{2+}$, $[(H_2O)FeO]^{2+}$, and $[(H_3N)FeO]^{2+}$ using the cc-pVTZ (Fe,NH$_3$,H$_2$O) aug-cc-pVQZ (terminal O) basis set. For the mono-coordinated complexes, solid circles correspond to $^5A''$ and open circles to $^5A'$ states.

2.1.4 Conclusion

High level electronic structure calculations are performed to study the electronic structure of FeO^{2+}. The ground state of FeO^{2+} is $^3\Delta$ followed by $^5\Delta$ and $^5\Pi$. The ground and low-lying excited states are of oxyl character with an equilibrium bond length around 2.1 Å. Also, another group of states with a shorter bond length such as $^5\Sigma^+$ has dominant oxo character. Introduction of ligands has significant effects on the electronic structure of FeO^{2+}. Strong field ligands such as NH$_3$ stabilize the oxo electronic configuration whereas, weak field ligands such as H$_2$O can stabilize both the oxo and oxyl states.

2.2 Electronic Structure of RhO^{2+}, Its Ammoniated Complexes (NH$_3$)$_{1-5}$RhO^{2+}, and Mechanistic Exploration of CH$_4$ Activation by Them

2.2.1 Rationale Behind the Choice of RhO^{2+}

Unlike the first-row transition metal oxides, second-row transition metal oxides are difficult to study specially by theoretical methods. The difficulty arises from many electrons correlation and relativistic effects associated with second-row transition metals. Dealing with the scarcity of the literature, only molybdenum, rhodium and palladium oxides are theoretically proposed as active sites for methane activation.[76-79] Though RhO has been studied before in both the experimental[80-84] and theoretical[85-90] front but to our best knowledge, we have little knowledge about the electronic structure of RhO^{2+}. Moreover, as we have discussed about the oxo wall[39, 40, 91] in the previous section, which is place between FeO^{2+} and CoO^{2+} which can be supported by the electronic structure of CoO^{2+} that has dominant oxyl character.[39] So, the study of the ground and excited states RhO^{2+}, which is analogous to CoO^{2+}, is going to unveil the validity of oxo wall for the second row transition metal oxides. It should be mention that previous study on the electronic structure of the neighboring RuO^{2+} has revealed an oxo form.[92]

Apart from the electronic structure of the ground and excited states of RhO^{2+}, spectroscopic constants and spin orbit calculation are performed to aide future experimental explorations. And effect of ligands is assessed by introducing 1-5 NH$_3$ ligands along with the C-H bond activation

mechanism utilizing the titled species. Finally, an energy landscape of a model system for methane to methanol transformation is presented to highlight the catalytic efficiency of the species.

2.2.2 Computational Details

For RhO^{2+}, three spin multiplicities namely doublet, quartet, and sextet (S=1/2, S=3/2, and S=5/2 respectively) are considered for the construction of the potential energy curves (PECs). At first, state average calculations utilizing complete active space self-consistent field (CASSCF)[66, 67] is performed to generate the reference wave function for the ground and low-lying excited states using C_{2v} symmetry (the largest Abelian subgroup of the original $C_{\infty v}$ symmetry of the molecule). The active space is chosen as 5s, 4d orbitals of Rh and 2p orbitals of O. In total, there are 11 electrons in 9 orbitals and every possible electronic configuration is allowed within this active space. Then using the reference wave function (CASSCF), multi reference configuration interaction (MRCI)[68, 69] calculations are done for the ground and low-lying excited states. Excitation from the 2s orbital of O is excluded at the CASSCF level because for all the states it is almost always doubly occupied but it is included for correlation at the MRCI level. To extract the spectroscopic constants, quintuple ζ quality basis set (cc-pV5Z-PP[93] for Rh and aug-cc-pV5Z for O)[70, 71] is used for the PECs around the equilibrium. An augmented basis set is used for O to account the bond polarization. But, to construct the full PECs, and for the coordinated species $(NH_3)_{1-5}RhO^{2+}$ a triple ζ basis set is used. To calculate the activation barriers and to construct the energy landscape of the C-H activation Density Functional Theory (DFT) is involved with MN15[94] functional. The multi reference calculations are performed using MOLPRO[72] and C-H activation is studied with Gaussian 16[95] electronic structure package.

2.2.3 Summary of the Results and Discussion

In the section most important findings reported in the following paper[96], provided in Appendix A, are summarized.

Reprinted (adapted) with permission from '**Khan, S. N.**; Miliordos, E., *Inorganic Chemistry* **2021,** *60*, 16111-16119.' Copyright 2021 American Chemical Society.

Electronic Structure of the bare RhO^{2+}

Considering all the spin mutiplicities together (figure 2.6 d), two different potential wells are present for the species RhO^{2+}. Potential energy wells with a shorter bond length 1.6−1.8 Å are steeper than the shallower ones with minima at distances longer than 2.0 Å. Also, the ground state $^2\Pi$ has an avoided crossing around 2.0 Å and for the first two excited states $1^{2,4}\Delta$, the avoided crossing happens around 2.2-2.3 Å. States of doublet and quartet spin multiplicities form stronger bond than sextet spin multiplicity. A closer look on the molecular orbitals is necessary to explain the bonding feature of the low-lying excited states. Also, for the full PECs covering the dissociation limit please see the supporting information of the article.[96]

Figure 2.7 depicts the valence molecular orbital contours of RhO^{2+} at equilibrium. The molecular orbitals 2σ, 3σ, 1π, and 2π has significant contribution from both the metal and the oxygen atom, whereas 1δ and 4σ orbital are mostly localized on the metal. The $2\sigma/3\sigma$ and $1\pi/2\pi$ orbitals represent the σ- and π-bonding/antibonding Rh−O orbitals ($3\sigma \sim \sigma_{RhO}^*$, $2\pi \sim \pi_{RhO}^*$). Table 2.1 lists the dominant electronic configurations and Table 2.2 tabulates spectroscopic constants for

the low-lying electronic states. The complete list of electronic configurations and spectroscopic constants of all the states those has been studied is presented in the reference article.[96]
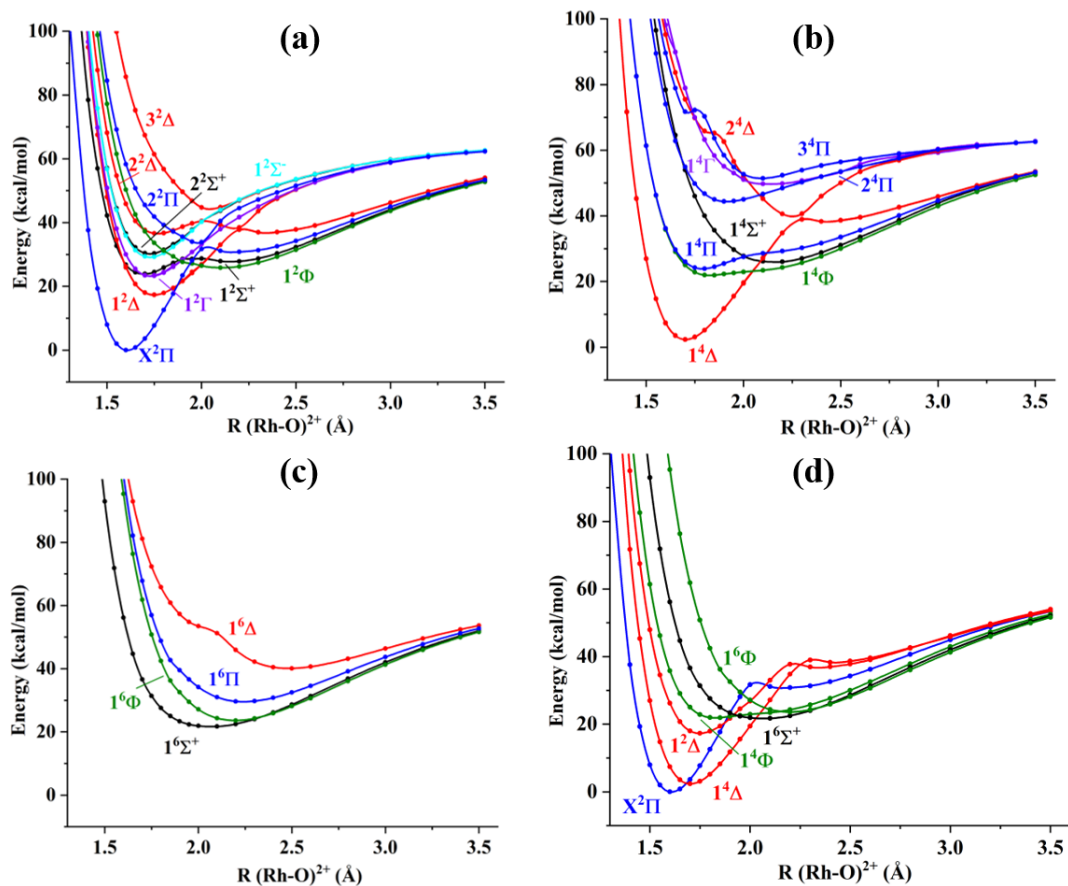
Figure 2.6: PECs of RhO^{2+} with respect to Rh-O distance for different spin multiplicity (a) doublet (b) quartet (c) sextet at MRCI+Q/5z level. The lower right graph (d) is the PECs of a few low-lying states of RhO^{2+} considering all the spins together.
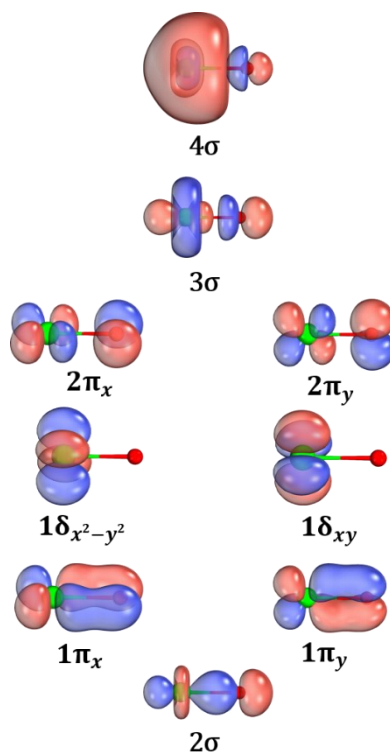
Figure 2.7: Selected valence molecular orbital contours of RhO^{2+} at equilibrium. The green sphere is Rh and the red one is oxygen. Only valence orbitals are numbered; 1σ (not shown here) corresponds to the 2s of oxygen.

The ground state $^2\Pi$ of RhO^{2+} has the shortest bond length of 1.608 Å (see Table 2.2, MRCI+Q) and only 0.1 eV lower in energy than the first excited state $^4\Delta$. The dominant CI coefficient and the electronic configuration of this state is $0.88 \left| 2\sigma^2 1\pi_x^2 \, 2\pi_x^1 \, 1\pi_y^2 \, 1\delta_{x^2-y^2}^2 \, 1\delta_{xy}^2 \right\rangle$ suggesting a single reference character and enabling the use of CCSD(T). At both CCSD(T) and C-CCSD(T), the equilibrium bond distance is found shorter than the corresponding MRCI+Q and C-MRCI+Q methods by 0.013 and 0.014 Å. The notations C-CCSD(T) and C-MRCI+Q stands for the core calculations where the electron correlations form the sub-valence orbitals are considered.

Table 2.1: Dominant electronic configuration for the lowest electronic states of RhO^{2+}. The A_1 and B_1 irreducible representation of the C_{2v} subgroup components for Δ and Γ (Π and Φ), respectively are only given.

State	Coef.	2σ	3σ	4σ	$1\pi_x$	$2\pi_x$	$1\pi_y$	$2\pi_y$	$1\delta_{x^2-y^2}$	$1\delta_{xy}$
$X^2\Pi$	0.88	2	0	0	2	α	2	0	2	2
$1^4\Delta$	0.92	2	0	0	2	α	2	α	2	α
$1^2\Delta$	0.71	2	0	0	2	α	2	α	2	β
	-0.35	2	0	0	2	α	2	β	2	α
	-0.35	2	0	0	2	β	2	α	2	α
$1^6\Sigma^+$	0.83	2	α	0	2	α	2	α	α	α
	-0.39	2	α	0	α	α	α	α	2	2
$1^4\Phi$	0.62	2	α	0	2	0	2	α	2	α
	-0.62	2	α	0	2	α	2	0	α	2
$1^2\Gamma$	0.44	2	0	0	2	0	2	2	2	α
	-0.44	2	0	0	2	2	2	0	2	α
	-0.44	2	0	0	2	α	2	β	α	2
	0.44	2	0	0	2	β	2	α	α	2
$1^6\Phi$	0.67	2	α	0	α	α	2	α	2	α
	-0.67	2	α	0	2	α	α	α	α	2
$1^4\Pi$	0.63	2	α	0	2	0	2	α	2	α
	0.63	2	α	0	2	α	2	0	α	2
$1^2\Sigma^+$	0.77	2	α	0	2	0	2	0	2	2

The first excited state $1^4\Delta$ has an equilibrium bond distance of 1.703 Å at the MRCI+Q level, almost 0.1 Å longer than the ground state, and it decreased to 1.687 Å at the CCSD(T) level. Alike the ground state, the first excited state is also single reference with a CI coefficient 0.92, and one 1δ (non-bonding) electron moved to the 2π (anti-bonding) orbital (see Table 2.1), which explains the elongation of the bond.

Table 2.2: Bond length r_e (Å), harmonic vibrational frequencies ω_e (cm^{-1}), anharmonicity $\omega_e x_e$ (cm^{-1}), $\Delta G_{1/2}$ (cm^{-1}) value, and excitation energy T_e (eV) for the lowest electronic states of RhO^{2+}. The energy order of the states is based on the MRCI+Q values.

State	Method	r_e	ω_e	$\omega_e x_e$	$\Delta G_{1/2}$	T_e
X$^2\Pi$	MRCI	1.610	951.4	7.8	935.9	0.000
	MRCI+Q	1.608	955.9	7.8	940.3	0.000
	C-MRCI	1.613	945.5	7.7	930.3	0.000
	C-MRCI+Q	1.612	953.8	7.4	939.1	0.000
	CCSD(T)	1.595	966.4	-4.6	975.9	0.000
	C-CCSD(T)	1.598	956.5	-7.1	969.7	0.000
1$^4\Delta$	MRCI	1.705	795.6	6.8	781.6	0.106
	MRCI+Q	1.703	798.9	6.8	785.0	0.102
	C-MRCI	1.708	787.1	7.0	772.1	0.153
	C-MRCI+Q	1.705	796.8	6.6	782.9	0.172
	CCSD(T)	1.687	878.5	7.2	863.1	0.147
	C-CCSD(T)	1.683	904.3	8.4	885.9	0.201
1$^2\Delta$	MRCI	1.754	666.7	6.6	653.7	0.751
	MRCI+Q	1.749	694.0	7.9	665.3	0.752
	C-MRCI	1.755	669.8	6.4	657.4	0.751
	C-MRCI+Q	1.745	711.6	7.7	686.0	0.767
1$^6\Sigma^+$	MRCI	2.122	304.1	0.5	306.0	0.828
	MRCI+Q	2.073	293.3	-1.7	291.8	0.942
1$^4\Phi$	MRCI	1.896	136.5	-12.5	140.3	0.892
	MRCI+Q	1.825	262.3	1.3	297.7	0.951
1$^2\Gamma$	MRCI	1.737	681.5	11.9	656.9	0.989
	MRCI+Q	1.722	697.8	11.7	681.2	1.010
1$^6\Phi$	MRCI	2.219	350.2	2.4	345.0	0.866
	MRCI+Q	2.196	349.4	2.3	344.7	1.026
1$^4\Pi$	MRCI	1.796	434.3	29.6	455.9	0.998
	MRCI+Q	1.789	614.2	40.7	534.3	1.037
1$^2\Sigma^+$	MRCI	1.698	316.4	18.7	393.8	0.994
	MRCI+Q	1.695	675.5	62.9	612.6	1.038

H₃C−H bond activation using (NH₃)₁-₅RhO²⁺

In this section we have presented the C-H activation mechanism using RhO^{2+} as the active unit. We have also introduced (1-5) NH_3 ligands in the system to study the effect of the number of NH_3 coordination in the C-H activation mechanism. NH_3 has been chosen as a representative of commonly used larger ligands coordinated to the metals with the lone pair of nitrogen.[4] Also, methane represents the saturated hydrocarbons with the strongest C-H bond and its small size is convenient for the computational study. Moreover, methane to methanol conversion is very important for its industrial and commercial applications.[97-100]

Geometry optimization of all the involved reactants, transition states, and products are done followed by the harmonic frequency calculation to ensure that all the species are at minima (for reactants, and products) or saddle point (for transition states) on the potential energy surface. Three spin multiplicities (doublet, quartet, and sextet) are considered to calculation the activation barriers.

To account the effect of ligands on the electronic structure of RhO^{2+}, the nature of the electronic configuration of Rh-O bond is monitored upon the gradual addition of the number of NH_3 ligation (Figure 2.8). The valence molecular orbitals of RhO^{2+} remains unaffected up to four ammonia coordination but it changes on the case of fifth ammonia. To accommodate the incoming fifth ammonia, one of the pure metallic orbitals $(1\delta_{x^2-y^2})$ is replaced with anti-bonding π orbital. Occupation of this anti-bonding orbital facilitates the weakens of Rh-O bond, and it has further consequences in the C-H bond activation. The comparison of the iso-surface of the molecular orbitals for the bonding and anti-bonding orbital of $(NH_3)_2RhO^{2+}$ and $(CH_4)(NH_3)RhO^{2+}$ shows the resemblance of methane and ammonia in terms of their approach towards the metal.
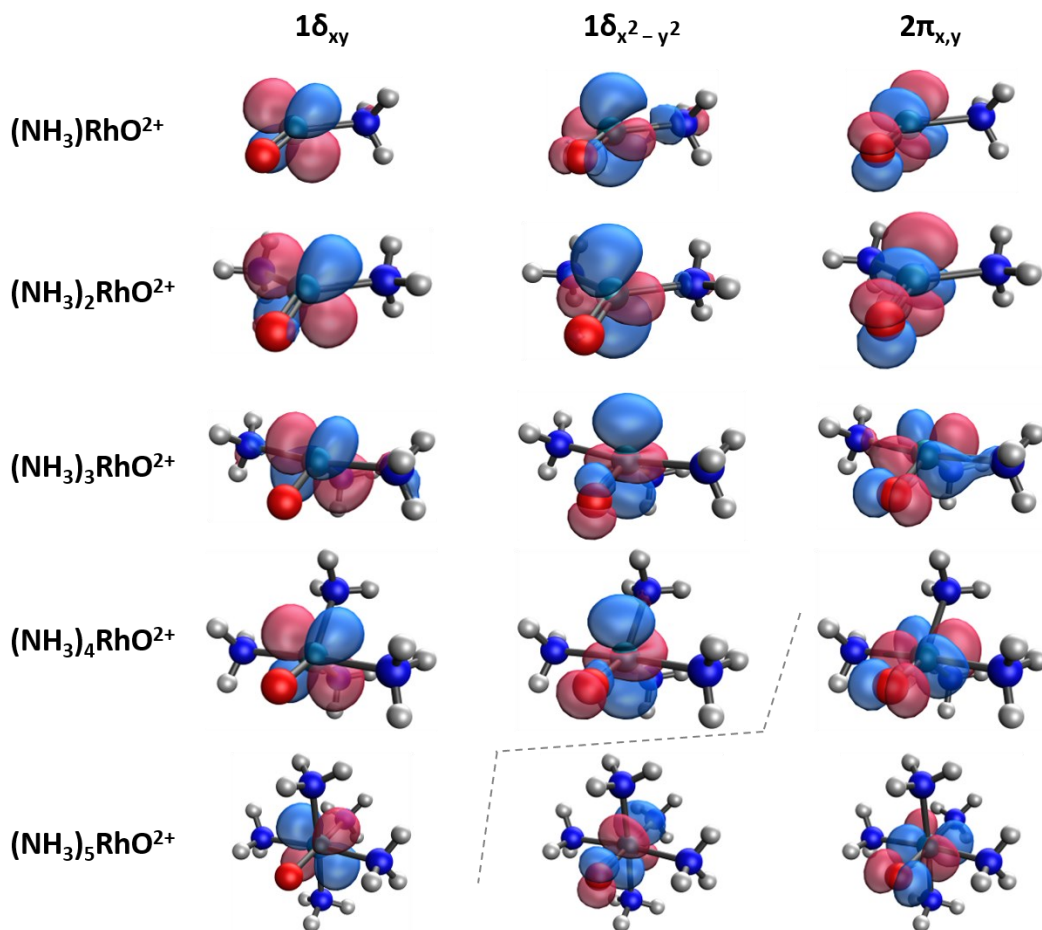
Figure 2.8: Electronic structure determining molecular orbitals (MN15/tz) of the $(NH_3)_{1-5}RhO^{2+}$. The notation follows that of plain RhO^{2+} for simplicity. The first two orbitals are doubly occupied and the last one singly occupied. Notice that ammonia ligands coordinate at specific orientations to minimize overlap with the occupied orbitals, and that $1\delta_{x^2-y^2}$ is replaced by a 2π orbital in the case of $(NH_3)_5RhO^{2+}$.

Ammonia coordinates with its lone pair and methane binds (binds weakly) using the C-H bonding orbital (Figure 2.9). Thus, CH_4 can act as a kind of ligand.

Table 2.3 tabulates the activation barriers for the C-H activation steps considering doublet, quartet, and sextet spin multiplicities in coordination with (1-5) NH_3 ligands. Two reaction mechanisms namely OA and HAT are involved in the case of doublet and quartet spin multiplication, but the sextet has only the HAT. The HAT has lower activation barriers ~ (10-20 kcal/mol) than the OA ~ (27-30 kcal/mol) but for the doublet spin multiplicity, the species $(NH_3)_4RhO^{2+}$, the OA mechanism has an exceptionally low activation barrier ~13 kcal/mol which is comparable/lower than the corresponding HAT which is very unexpected and unnatural for similar situations. The reason of this very low activation barrier is caused by the change of electronic structure for more than four ammonia conjugation. For this species, the approaching CH_4 towards $(NH_3)_4RhO^{2+}$ acts as the fifth ammonia (as we have discussed before). In this case, the C-H bond is not screened, and the metal breaks it apart. Figure 2.10 depicts the cartoons of the transition states for the HAT and OA mechanism. This catalytic active site has two major advantages. First, exceptionally low activation barrier, and second, the presence of four ligands is expected to help finding selective catalysts which will prevent methanol from entering the catalytic sphere. So, we have constructed a complete energy landscape for the C-H activation and recombination of the species to form methanol. (Figure 2.11) For the recombination step, the HAT mechanism has an activation barrier of 4.7 kcal/mol. The OA mechanism channel is thermodynamically lower in energy than the radical mechanism, but it has higher activation barrier of 22.4 kcal/mol. A comprehensive kinetic study of the competing reaction mechanism can be done in the future to select the more favorable reaction channel.

(NH₃)₂RhO²⁺   (CH₄)(NH₃)RhO²⁺
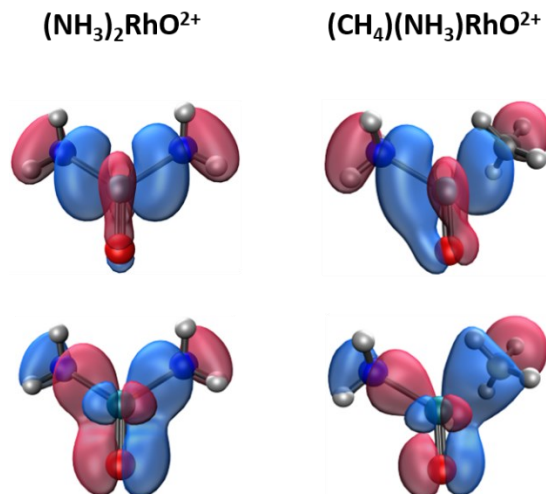
Figure 2.9: Molecular orbitals of the Rh−N bonds of $(NH_3)_2RhO^{2+}$ compared to those of the Rh−N and "Rh−C" bonds of $(CH_4)(NH_3)RhO^{2+}$.

Table 2.3: MN15 C−H bond activation energy barriers $\Delta E^{\neq}$ (kcal/mol) of the radical and [2+2] addition mechanisms for the $CH_4 + (NH_3)_nRhO^{2+}$ reaction with different spin (S) multiplicities.

n	S = ¹/₂		S = ³/₂		S = ⁵/₂
	Radical	**[2+2]**	**Radical**	**[2+2]**	**Radical**
R.M[b]	*PCET/HAT*	*OA*	*PCET/HAT*	*OA*	*HAT*
1		27.7		27.0	
2	0.4	22.9		27.8	24.9
3	15.3	30.9	17.7	27.5	10.5
4	14.8	13.6	16.7	40.8 [a]	14.3
5	12.8		20.0		16.7

[a] Single point energy calculation using the S=¹/₂ optimized structure.

[b] R.M (Reaction Mechanism)
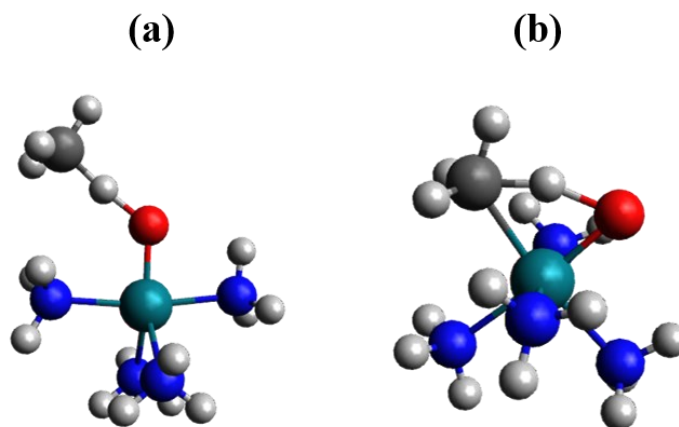
Figure 2.10: Transition state for the C−H bond activation of methane with $RhO^{2+}(NH_3)_4$ (S=$^1/_2$): (a) radical mechanism, (b) [2+2] addition mechanism.
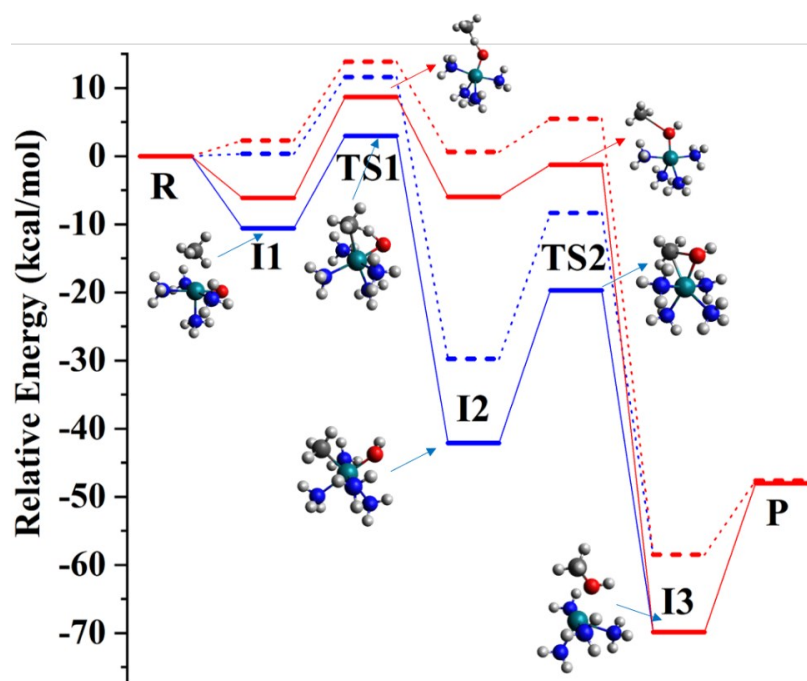
Figure 2.11: Energy landscape (S=1/2) for the $CH_4 + (NH_3)_4RhO^{2+} \rightarrow CH_3OH + (NH_3)_4Rh^{2+}$ reaction following [2+2] addition mechanism (blue lines) and radical mechanism (red lines) where R = Reactants ($CH_4 + (NH_3)_4RhO^{2+}$), I = Reaction intermediates, TS = Transition States, and P = products ($CH_3OH + (NH_3)_4Rh^{2+}$). Solid lines correspond to electronic energy and dashed lines to free energy (25 °C, 1 atm).

2.2.4 Conclusion

High level electronic structure theory is used to study the ground and excited states of naked RhO^{2+}. Construcution of the PECs for different spin multiplicities are done for the spectroscopic constants, vibrational frequencies, bond lengths, spin-orbit constants and excitation energies. The ground state of RhO^{2+} is $^2\Pi$ followed by $^4\Delta$ and $^2\Delta$. The ground state and the low-lying excited states are of oxo character. Comparing this results with CoO^{2+},[39] the validity of the concept of 'oxo wall' for the second row transition metal oxides is undermined. Also, we have investigated the bonding scheme of rhodium and oxygen for the coordination of (1-5) NH_3 ligands and it is found that the electronic confighuration of the Rh-O bond is unaffected upto four ammonia ligands but it takes a different configuration for five ammonia. This change of electrionic structure results in an exceptionally low barrier of C-H activation for the case of $(NH_3)_4RhO^{2+}$ with methane. A complete energy landscape of this reaction is presented considering the recombination of the species to form methanol. For the C-H activation, OA, PCET and HAT mechanisms are considered accounting different spin mulitiplicites. Also, the similarity of methane and ammonia are presented in terms of their approch towards the metal.

Chapter Three

3. Methane to Methanol Transformation Facilitated by Transition Metal Methoxides FeOCH$_3^{+/2+}$

Despite of significant development in the green/renewable energy sector which is sought to be the replacement of fossil fuel, fossil fuel still dominates the global economy because of its low-cost and availability. The popularity of fossil fuel such as natural gas and petroleum, is due to its high energy content that can be utilized both in large-scale (industrial) and small-scale (domestic) basis. Fossil fuels are the source of hydrocarbons those can be used to produce numerous platform chemicals. Methane, which is the smallest hydrocarbon, is the prime component of natural gas. In recent times, the production of methane has increased due to the process of hydraulic fracturing (fracking). The transformation of methane into methanol has scientific, industrial, economic, and environmental importance. Methane is a gas, and the gas fields (natural gas) are usually located in the remote areas which makes the transportation cost high due to the requirement of the installation of pipelines. Whereas, methanol is a liquid, and the transformation of methane into methanol can highly reduce the cost of transportation. Moreover, methane is the most potent greenhouse gas, that can trap heat in the atmosphere.[101, 102] Considering these major factors, active research is ongoing to develop an effective method to upgrade methane with functional groups. Owing to its importance, methane to methanol (MTM) transformation is long sought in the science community but despite of a search for half a century an effective low energy MTM method is still elusive.

For industrial application, methane is converted to liquid fuels following a high energy procedure. At first, methane is decomposed to $CO + H_2$ (synthetic gas) and then transformed into methanol using high energy (15 – 40 atm pressure, 700 – 1000º C).[103, 104] But this procedure is economically feasible only at large industrial scale. To avoid the syngas route, direct methane to methanol transformation is a subject of active research.[100, 105] Different techniques such as gas-phase and solution-phase homogenous catalysis, photocatalyst, biocatalyst (enzymes),[106] plasma technology, frustrated Lewis-pairs,[107, 108] Metal Organic Frameworks (MOFs)[109-111] have been proposed. Though all these techniques have a lot of encouraging progresses[112, 113] but each of them has their own drawbacks and limitations.[114] In reality, the proposed techniques for MTM suffers fundamental complexities[103, 115, 116] and a technique with high yield is yet to be discovered.[100, 114, 117-123]

For MTM transformation, transition metal oxides are considered as very effective catalysts for homogenous and heterogenous catalysis. Specially, FeO and their charged variants drew attention for both experimental and theoretical explorations to mimic the effective C-H bond activation scheme chosen by nature.[53-55, 57, 124, 125] For iron-oxide systems, FeO^{2+} acts as catalytic active site and the C-H activation proceeds through either creating a radical intermediate or following [2+2] addition mechanism. The metal-ligand personality dictates the route of the C-H bond activation mechanism.[126] From our previous work (see chapter 2) on the ligand field effects on the electronic structure of FeO^{2+} demonstrate that the strong field ligands stabilize the iron-oxo states hence favor the [2+2] addition mechanism whereas the weak field ligands stabilize both the oxo and oxyl states.[73] The productivity of the catalytic cycle depends on the following two factors-

1.The activation energy barrier for C-H activation

2.Selective oxidation of methane and not methanol

The second factor is very prominent and known as the selectivity issue for methane activation. Most of the catalytic systems those has been proposed for high yield methane activation suffers from this selectivity issue where the catalyst tends to activate the product methanol more easily than methane.[100, 105, 114, 124]

Considering the two mechanisms for methane activation namely [2+2] addition and radical formation, the later one usually has the lower activation barrier but suffers from the selectivity issues. By using a simple kinetic model, it has been shown that there is a fundamental tradeoff between the efficiency and selectivity of the methane activation with radical mechanism.[114] Higher C-H activation efficiency leads to less selectivity. For the radical mechanism, the problem has been explained as the activation barrier for the C-H bond of methane and methanol is catalyst-independent. As the C-H bond of methanol is slightly weaker than the C-H bond of methane, so the product methanol is more likely to be oxidized. From that study, the proposed solutions are the followings-

1. Use of a collector/solvent to withdraw methanol from the reaction site

2. Stabilize/optimize [2+2] addition mechanism over radical mechanism

3. Use of different catalyst rather than metal oxides

The first option is going to add the cost of separation of solvent and the product. The second option is contingent upon the sensitivity of the metal ligand combination that may lead to very complex reaction mechanism (as we have addressed in chapter 2). For these reasons we have considered the third option and shifted our focus from metal oxide catalysts and explored a complete catalytic cycle for MTM transformation using metal methoxide as a catalyst.

3.1 Complete Catalytic Cycle for Methane to Methanol Transformation using Metal Methoxides

Inspired by the work of Najafian and Cundari, we have investigated a complete catalytic cycle for MTM transformation using charged metal methoxide as a catalyst. Cundari *et al.* have used methoxides of the first-row transition metals for the C-H bond activation of methane.[127] Also, a recent study has demonstrated the effectiveness of metal methoxides in MTM conversion using copper-doped zeolites and H_2O as an oxidant.[113] Here, the oxidation reaction with H_2O is endothermic, so we have employed stronger oxidants (N_2O, O_3) in our catalytic cycle. N_2O and O_3 are often used in similar gas-phase catalytic reactions.[62, 128-130] Our research on MTM divided into two parts. In the first part we have employed $FeOCH_3^+$ as a catalyst and N_2O as an oxidant. With this combination we have studies the complete catalytic cycle. Then in the second part, we have further optimized the catalytic cycle by introducing ligands and replacing the oxidant N_2O with O_3. After the optimization of the catalytic cycle the best combination is found as $(NH_3)_4FeOCH_3^{2+}$ as a catalyst with the oxidant O_3. In this chapter, at first, we will present the results of the complete catalytic cycle using bare catalyst and N_2O oxidant. Then we will demonstrate the optimization of the catalytic cycle with ligated catalyst with an oxidant O_3.

3.1.1 Mechanistic Considerations of the Full Catalytic Cycle for the Catalyst FeOCH₃⁺ and N₂O as an Oxidant

Reprinted (adapted) with permission from '**Khan, S. N.**; Miliordos, E., *The Journal of Physical Chemistry A* **2019,** *123*, 5590-5599.' Copyright 2019 American Chemical Society.

The complete catalytic cycle that we have proposed has three main reactions and they are the followings-

Reaction 1: $FeOCH_3^+ + CH_4 \rightarrow FeCH_3^+ + CH_3OH$ (C-H bond activation)

Reaction 2: $FeCH_3^+ + N_2O \rightarrow OFeCH_3^+ + N_2$ (Oxidation)

Reaction 3: $OFeCH_3^+ \rightarrow FeOCH_3^+$ (Isomerization)
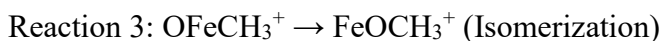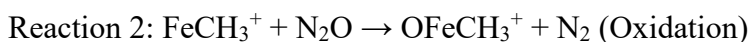
Cundari et al. has studied the C-H bond activation step utilizing uncharged L_nMOCH_3 where M=Ti-Cu and L_n= tridentate ligands using Density Functional Theory (DFT).[127] In our proposed complete catalytic cycle, we have utilized $FeOCH_3^+$ as a catalyst because in our initial assessment we have found the charge variant is more effective for a complete catalytic cycle (see results and discussion).

For Reaction 1, the C-H bond of methane cleaves, and the H atom binds to the methoxide produces methanol and the remaining methyl group coordinates to the iron. In the oxidation reaction (reaction 2), N_2O oxidizes the metal center and forms terminal FeO bond. Finally, in reaction 3 (isomerization) that O migrates between Fe and CH_3 unit and completes the catalytic cycle. Considering the feasibility of synthesis, the catalytic cycle can be initiated from reaction 2 with iron-methyl unit.[131]

The FeCH$_3^+$ and OFeCH$_3^+$ units can react with another CH$_4$ and activate C-H bond to produce byproducts. To account for those, we have also considered another three competing side reactions in the study, and we have compared the energy landscapes for all these reactions to assess the viability of the proposed catalytic cycle. The competing side reactions are the followings-

Reaction 4: FeCH$_3^+$ + CH$_4$ → (H$_3$C)$_2$FeH$^+$

Reaction 5: OFeCH$_3^+$ + CH$_4$ → H$_3$C…. HOFeCH$_3^+$

Reaction 6: OFeCH$_3^+$ + CH$_4$ → (H$_3$C)$_2$FeOH$^+$
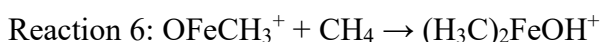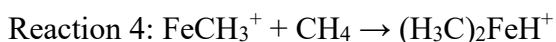
Figure 3.1 is the representation of the complete catalytic cycle with the solid lines represents the catalytic reactions (Reaction 1-3) and the dashed lines are alternative unfavorable routes (Reaction 4-6).
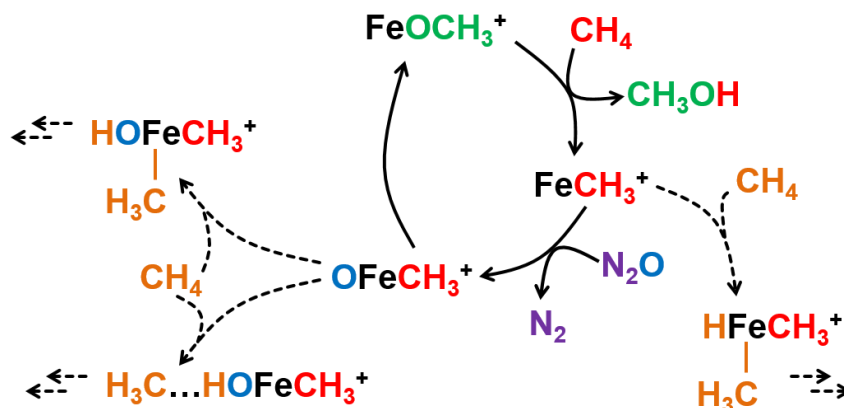
Figure 3.1: Solid lines show the proposed catalytic cycle, while dashed lines correspond to side routes, which need to be suppressed. Arrows represent all possible subsequent reaction steps.

For demonstrative purpose, an examplenary energy landscape of the complete catalytic cycle is presented in Figure 3.2 The transition states TS1, TS2, and TS3 corresponds to reaction

1-3 and TS4, TS5, and TS6 corresponds to the transition states of the initial steps of the unfavorable pathes (reaction 4-6). The energies for these structures and the products associated with them are drawn with dashed lines in Figure 3.2 For consistency, the energy of the "observer" molecules is added at every step. Ideally, TS4 must be much higher in energy than TS2 and both TS5 and TS6 much higher than TS3. It should be mentioned that both $FeCH_3^+$ and $OFeCH_3^+$ can in principle react with existing methanol, instead of CH_4 (steps (4)-(6)) and activate one of its $C-H$ bonds. The results will be either a poisoned catalyst or over-oxidation products. As opposed to the radical mechanism, the proposed mechanism necessitates the proximity of the substrate to the catalytic site. The use of molecular catalysts with proper ligands that exclude methanol from the active site can remedy this issue. The ligand effects will be explored in the second part of this chapter. Another important aspect in the theoretical study of catalytic cycles is the spin crossovers occurring along the reaction coordinate of some step. To account the submerged reaction barriers and two state reactivity, we constructed potential energy profiles for different spin multiplicities along the reaction coordinate of each step.
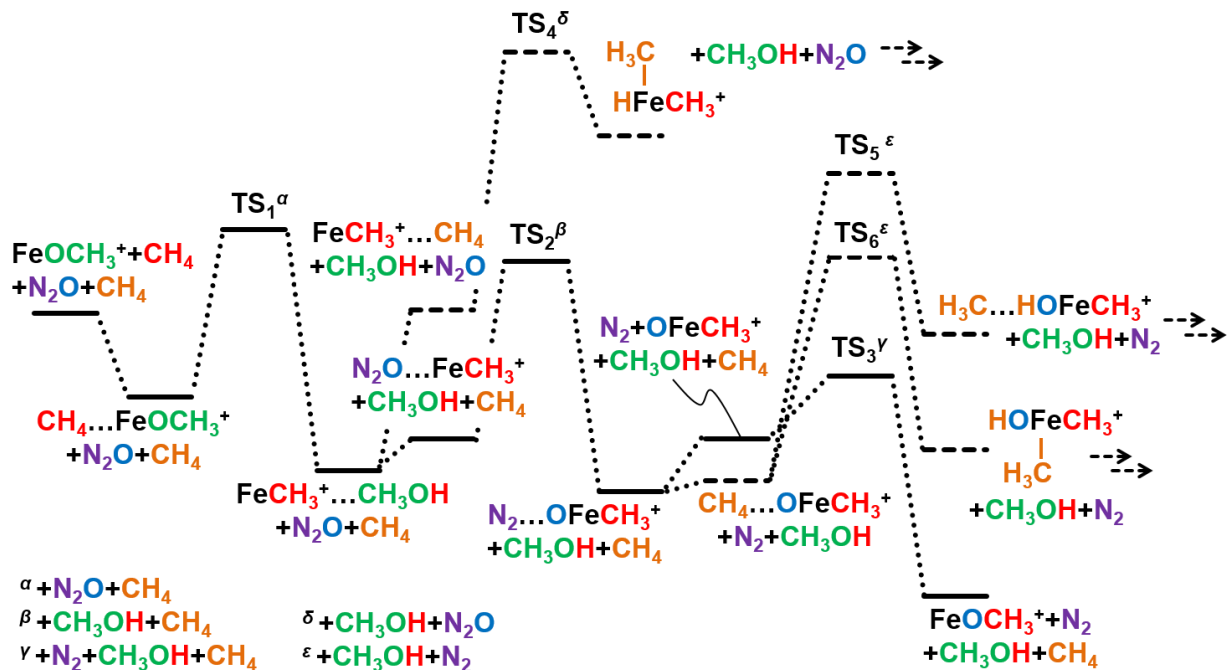
Figure 3.2: Ideal energy landscape for the proposed catalytic cycle. The A…B notation indicates the interacting complex of molecules A and B. Arrows represent all possible subsequent reaction steps.

3.1.2 Computational Details

A recent review demontrates the computational methodologies for the proper description of the electronic strucuture of transition metal compounds specially for catalytic application.[128] The authors emphasized the necessity of highly accurate approaches, such as multi-reference methodologies. Another recent work of Nakatani and Hada (on the similar reaction $FeO^+ + CH_4$) demonstrated that static-correlation-only multi-reference (complete active space self-consistent field or CASSCF) calculations can be quite misleading even if a large active space is used.[132] On

the other hand, density functional theory (DFT) should be subjected to careful evaluation of its ability to correctly grasp the required physical phenomena.[128, 131, 133] Therefore, three different types of calculations were performed to shed some additional light: CASSCF and multi-reference configuration interaction (MRCI), single reference coupled clusters (CCSD(T)), and DFT (unrestricted Kohn-Sham formulation) calculations. The MN15 functional is chosen in the latter case since it shows good performance for transition metals and non-covalent interactions.[134]

Correlation consistent triple-ζ (TZ) quality basis sets (cc-pVTZ)[132, 135] is used for the calculations. A series of diffused functions (aug-cc-pVTZ)[130] is employed on the oxygen center to account the ionic nature of the metal-oxygen bond.[70, 71, 94, 136-138] But for some computationally demanding cases, double-ζ (DZ) quality basis set are employed.

Reaction 3 is a unimolecular reaction (isomerization) of $OFeCH_3^+$ to $FeOCH_3^+$. We have selected this step to compare the optimization at the MRCI, MRCI+Q, CASPT2, CCSD(T), and MP2 levels of theory with triple-ζ (TZ) quality basis sets. This reaction is chosen because it allowed us to directly assess on the electronic structure description avoiding the contribution of intermolecular electrostatic and dispersion interactions. Overall, DFT/MN15/TZ gives accurate geometries, but provides less accurate energetics. This is an indication that the equilibrium region of each stationary geometry (except TS2; see below) is described satisfactorily at DFT/MN15, but the energy differences among the different equilibria are less satisfactory. Thus, we calculated harmonic vibrational frequencies were obtained only at the DFT/MN15/TZ level, which is computationally less demanding. One imaginary frequency was found for every transition state, and only real ones for all intermediates. The normal modes pertaining to the imaginary frequency for these first order transition states validate that TS1 through TS6 connect the intermediates shown in Figure 3.4.

To assess the multi-reference character of the wavefuction for the reaction intermediates and transition states are estimated by the amplitude of the dominent electronic configuration (C_0) and T1 diagonstic at the CCSD level. (for full table, see SI of the article)[139] For almost all cases the ground state is found mostly single-referece with a range of $0.86 < C_0 < 0.99$. The T1 diagnostic ranges from 0.026 to 0.073, and although in some cases is larger than the limit of 0.05 suggested for transition metal compounds in the literature[140] but the CCSD(T) results are consistent with the MRCI and DFT/MN15 ones supports that they are single reference.

The selection of the active space for the CASSCF calcualtions are very challenging because the full valence space is prohibititively large. The CASSCF active orbitals were chosen to include the valence space of iron and the orbitals relative to the bonds cleaved or formed, i.e., the σ and σ* orbitals of the inert C-H bonds were excluded. Special attention was paid to include the same number of active orbitals and electrons at every single step. In all cases we allocated 16 electrons in 13 orbitals. All valence electrons were correlated at the subsequent multi-reference configuration interaction singles and doubles (MRCI) and second order perturbation theory CASPT2 (RS2C approach as implemented in MOLPRO) calculations. Excited state calculations were based on state-average CASSCF (SA-CASSCF) reference wavefunctions. The DFT calculations were done with the Gaussian16[95] suite of codes and all other calculations with MOLPRO2016.[72]

Finally, the energy profiles along the reaction coordinate of each step were constructed at the MRCI+Q/TZ level using the DFT/MN15/TZ geometries of an intrinsic reaction coordinate (IRC) calculation with Gaussian16. The Davidson correction (+Q) was implemented to reduce the size-extensivity error.

3.1.3 Summary of the Results and Discussions

In the section most important findings reported in the following paper[139], provided in Appendix B, are summarized..

Reprinted (adapted) with permission from '**Khan, S. N.**; Miliordos, E., *The Journal of Physical Chemistry A* **2019,** *123*, 5590-5599.' Copyright 2019 American Chemical Society.

Motivated by the work of Najafian and Cundari,[127] we initially constructed the energy landscape for neutral $FeOCH_3$ by means of DFT/B3LYP/TZ. For all species we found that S=3/2 always provides the lowest energy spin state. The energy plot is shown with blue lines in Figure 3.3 We were not able to locate TS2 in this case, but the best structure we obtained is much higher than TS4, which means that the attachment of a second methane molecule to iron is preferred over the oxidation of iron. Additionally, TS5 and TS6 are lower in energy than TS3 leading to unfavorable paths, as described in the previous section. Overall, steps two and three deviate appreciably from the ideal energy diagram of Figure 3.2 We then switched to $FeOCH_3^+$ and the energy diagram of which is closer to that of Figure 3.2.
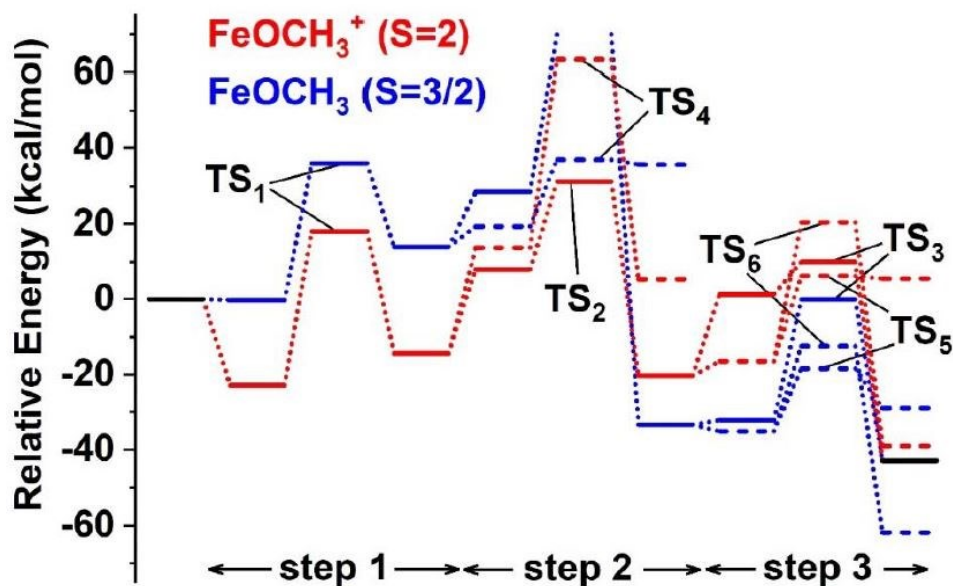
Figure 3.3: DFT/B3LYP energy landscape for the proposed mechanism using neutral (blue lines) or cationic (red lines) iron-methoxide.

Initially, for reaction 1-6, we demonstrate our finding for each of the reactions seperatly and then finally we combine the results to assess the compelete catalytic cycle by constructing the full energy landscape. All intermediate and transition state structures are collected in Figure 3.4
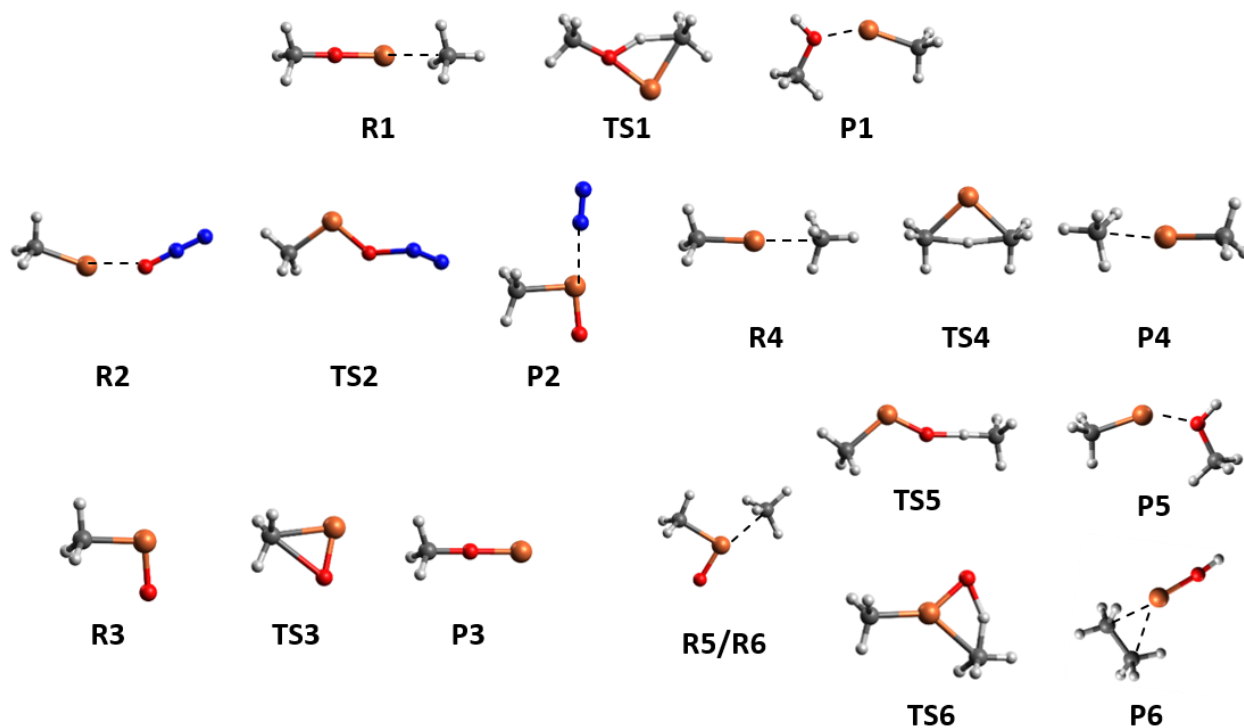
Figure 3.4: DFT/MN15 optimal structures of all intermediates for steps (1)-(6). R, P, and TS correspond to reactants, products, and transition states, respectively.

We first analyze our results on **reaction 3** since we did a more extensive assessment of different electronic structure methodologies in this case. This step involves only one molecule transforming from the metal oxide $OFeCH_3^+$ (R3) to the metal methoxide $FeOCH_3^+$ (P3) via the transition state TS3 (see Figure 3.4). Among the different methodologies the Fe-O and Fe-C bond lengths were found more sensitive to the treatment of electron correlation. Table 3.1.1 lists these bond lengths at MRCI, MRCI+Q, CCSD(T), CASPT2, MP2, DFT/B3LYP, and DFT/MN15. The TZ basis set is used always, but both DZ and TZ basis sets were used for CCSD(T).

Table 3.1: Activation energy (E_{act} in kcal/mol), reaction energy (E_{rxn} in kcal/mol), Fe-O (R_{FeO}) and Fe-C (R_{FeC}) bond lengths (in Å) for the reactants (R3), products (P3), and transition state (TS3) of step (3) with different methodologies.

Quantity	MRCI[a]	MRCI+Q[a]	CCSD(T)[a]	CCSD(T)[b]	CASPT2[a]	MP2[a]	MN15[a]
			OFeCH$_3^+$ (R3)				
R_{FeO}	1.618	1.616	1.608	1.621	1.619	1.518	1.579
R_{FeC}	2.012	1.991	1.967	1.975	1.988	1.944	1.936
			TS3				
R_{FeO}	1.660	1.654	1.642	1.653	1.639	1.534	1.622
R_{FeC}	2.157	2.148	2.091	2.103	2.158	2.078	2.063
E_{act}	8.7	9.5	9.0	8.7	15.8	12.9	5.3
			FeOCH$_3^+$ (P3)				
R_{FeO}	1.707	1.704	1.699	1.706	1.679	1.697	1.685
E_{rxn}	-42.7	-38.0	-46.4	-44.7	-25.7	-64.0	-54.6

[a] Basis set: cc-pVTZ (Fe, C, H), aug-cc-pVTZ (O)

[b] Basis set: cc-pVDZ (Fe, C, H), aug-cc-pVDZ (O)

Moving from MRCI/TZ to MRCI+Q/TZ and to CCSD(T)/TZ, both bonds shorten monotonically. The average decrease is less than 0.01 Å going from MRCI/TZ to MRCI+Q/TZ and ~0.02 Å from MRCI+Q/TZ to CCSD(T)/TZ. Interestingly, CCSD(T)/DZ agrees better with MRCI+Q/TZ with an average difference of 0.01 Å, the latter predicting longer bonds. MP2/TZ shows some large deviations in some cases of ~0.1 Å, but CASPT2/TZ agrees very well (within

~0.01 Å) with both MRCI+Q/TZ and CCSD(T)/TZ. DFT/MN15/TZ showed relatively large average differences from MRCI+Q/TZ and CCSD(T)/TZ of 0.045 and 0.035 Å.

It turns out that these geometrical differences affect minimally (< 1kcal/mol) the energetics. We performed single-point CCSD(T)/TZ calculations employing the optimal geometries of every method. The activation barriers (E_{act}) and reaction energies (E_{rxn}) were found in the range of 8.5 ± 0.5 and -46.6 ± 0.2 kcal/mol, respectively, except for E_{act}(CCSD(T)/TZ// MP2/TZ) which is 5.5 kcal/mol. On the other hand, both E_{act} and E_{rxn} depend strongly on the level that the electron correlation is treated. E_{act} can be as small as 5.3 kcal/mol (MN15/TZ) and as big as 15.8 kcal/mol (CASPT2/TZ). We believe that the value of 9.1 ± 0.4 kcal/mol representing the range for the MRCI/TZ, MRCI+Q/TZ, and CCSD(T)/TZ approaches is more accurate and is in harmony with the CCSD(T)/TZ range when different geometries are employed. The E_{rxn} values cover a larger range from -25.7 kcal/mol (CASPT2/TZ) to -64.0 kcal/mol at MP2/TZ. Again, the 40-45 kcal/mol values of MRCI/TZ, MRCI+Q/TZ, and CCSD(T)/TZ levels should be considered more accurate. To compromise between accuracy and efficiency, we finally decided to obtain MN15/TZ and CCSD(T)/DZ optimized structures and perform single-point CCSD(T)/TZ calculations. This approach gives an E_{rxn} value of -46.4 and -46.8 kcal/mol when the CCSD(T)/DZ and MN15/TZ geometries are used. This practice is followed for the rest reaction steps.

The agreement between multi-reference MRCI/MRCI+Q and single-reference CCSD(T) energetics is better for E_{act}, which relates to R3 and TS3, than E_{rxn}, which relates R3 and P3. Looking at the multi-reference character of the wavefunctions through the T1-diagnostics of R3, TS3, and P3, we see the order P3 (0.038) < TS3 (0.069) < R3 (0.091). Only P3 is below the threshold of 0.05 suggested in the past for reliable CCSD(T) results.[140] Therefore, we get better

agreement for E_{act}, where both related diagnostics are higher than the threshold, than E_{rxn}, where one diagnostic is "normal" and one is almost twice larger than the threshold. This suggest either cancelation of errors, or that the threshold of 0.05 should be revisited. Looking at the coefficient of the larger electronic configuration in the CI vectors, we observe the following order P3 (0.99) > TS3 (0.89) > R3 (0.88), which is in harmony with the T1-diagnostics. The present T1-diagnostics are the largest among all our structures (see Table S1 of the article).[139] Since there is a fair agreement between MRCI/MRCI+Q and CCSD(T) in this case, we believe that our CCSD(T) results are in general quite accurate, and that our conclusions on the catalytic activity will not be affected significantly.

The potential energy profiles (PEPs) along the reaction coordinate for this step are shown in Figure 3.5. The migration of oxygen from iron in-between iron and carbon is described by the OFeC angle. This is around 100° for R3 and almost 0° for P3 (see Figure 3.5). All other parameters are optimized at the MN15/TZ level for every angle, while the C_s symmetry is preserved. Using these geometries, we performed MRCI+Q/TZ calculations for several low-lying electronic states of triplet and quintet spin multiplicity.
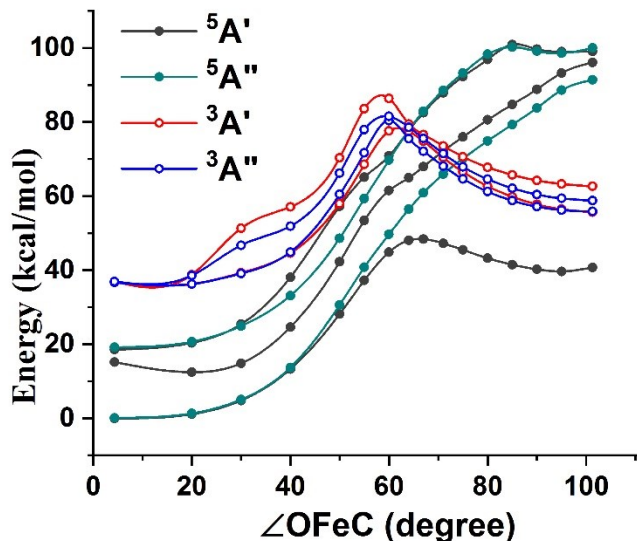
Figure 3.5: MRCI+Q-PEPs as a function of the OFeC angle for reaction (3). All other geometrical parameters are optimized for every angle at the MN15/TZ level of theory for the ground $^5A'$ state.

$FeOCH_3^+$ is pseudo-linear and therefore its $^5A'$ ground state is nearly degenerate with a $^5A''$ state. Recall that iron is best described as $Fe^{2+}(d^6; {}^5D)$. In these two states there are two unpaired electrons to the two $3d_\pi$ orbitals, one electron in a $d_\sigma \sim 3d_z^2$ orbital, and three electrons in the two $3d_\delta$ orbitals (see Figure 3.6). The latter configuration makes the two states distinct but nearly degenerate ($3d_{\delta+}{}^2 3d_{\delta-}{}^1$ and $3d_{\delta+}{}^1 3d_{\delta-}{}^2$) resembling a $^2\Delta$ state. The rest five components of $Fe^{2+}(d^6; {}^5D)$ make the next quintet states around ~20 kcal/mol higher. These split in a pseudo $^2\Pi$ and $^2\Sigma^+$ branches.

At the other side, $OFeCH_3^+$ has a $Fe^{4+}(d^4; {}^5D)$ nature and only one out of these five components dominate. The rest four components are rather unstable sliding readily to the $FeOCH_3^+$ quintets. The reason is that now some d-orbitals participate to the formation of the additional bonds and become unavailable to host "pure-iron" electrons. That's why triplets, where d-electrons pair

63

up are the first excited states below the unstable quintets. The triplets of the two species are both stable and separated by large energy barriers compared to the ground $^5A'$ state (see Figure 3.5).

$3d_\delta$ $3d_\pi$ $3d_\sigma$
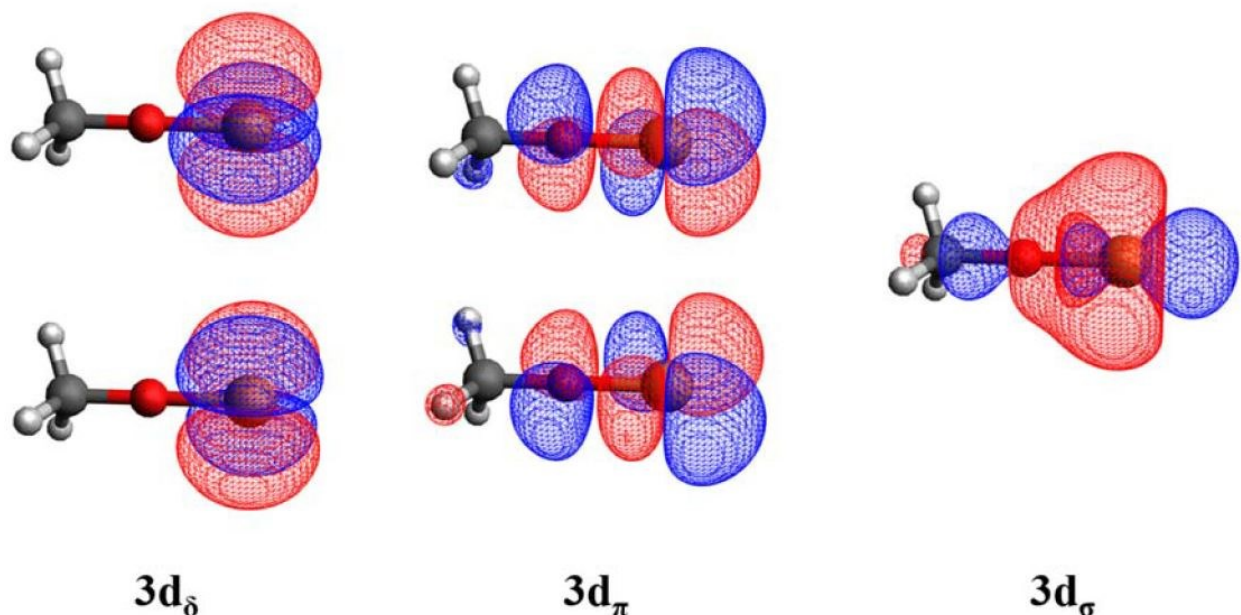
Figure 3.6: Molecular orbital contours for $FeOCH_3^+$ (only the valence electrons of Fe).

Overall, the quintet ground state is well-separated from the excited states and the barrier from the reactants to the thermodynamically more stable products is minimal.

The first step (**reaction 1**) involves the attack of methane to $FeOCH_3^+$ and the release of CH_3OH. The produced form of the catalyst, $FeCH_3^+$, has very similar electronic structure to $FeOCH_3^+$. In both cases iron is in a $Fe^{2+}(d^6; {}^5D)$ state. They are both quasi-linear systems, and the ^5D splits into the five pseudo-$^2\Delta$, $^2\Pi$, and $^2\Sigma^+$ states. The optimal geometries of the reactants (R1), transition state (TS1), and products (P1) are shown in Figure 3.4.

Starting from TS1, we followed the intrinsic reaction coordinate (IRC) along the two directions of the vibrational mode pertaining to the imaginary frequency. The IRC was calculated at the MN15/TZ level of theory, but selected geometries were used to perform MRCI+Q/TZ for the low-lying excited states. Figure 3.7 depicts the PEPs along this IRC for the five components of $Fe^{2+}(d^6; {}^5D)$ plus the first triplet state. The similarity of the electronic structure of the reactants and products is also supported by the persistence of the near degeneracy for the pseudo-${}^2\Delta$ and ${}^2\Pi$ components along the IRC.
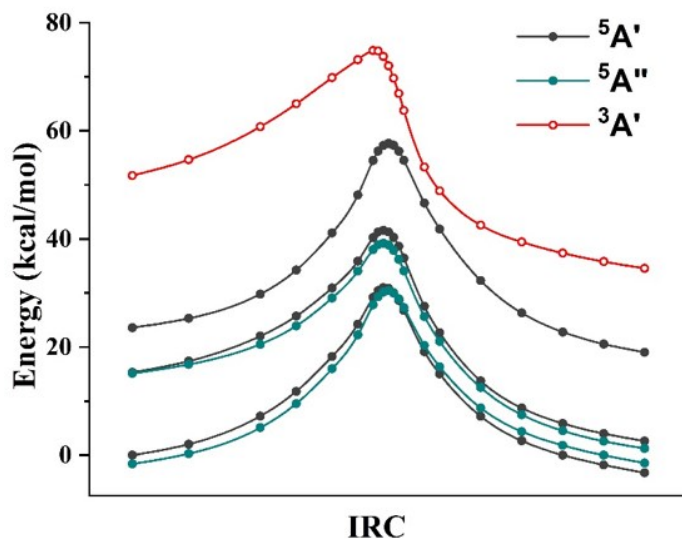
Figure 3.7: MRCI+Q-PEPs for several low-lying electronic states along the reaction coordinate of reaction 1.

Reaction 2 involves the reload of the iron center with oxygen and induces the strongest electronic structure variations. The DFT/MN15 search for TS2 converged readily to that of Figure 3.4. However, locating TS2 with MRCI or CCSD(T) turned out to be very challenging. The

CASSCF electronic wavefunction presented convergence issues, while the optimization algorithm was unable to locate TS2. To identify the cause, we started from the TS2 of DFT/MN15 and scanned over a wide range of the Fe-O and O-N distances. The two-dimensional PEPs are plotted in Figure 3.8. Long Fe-O and short O-N distances correspond to the reactants $CH_3Fe^+ + ON_2$, while short Fe-O and long O-N distances to the products $CH_3FeO^+ + N_2$. The DFT/MN15 distances for TS2 are 1.756 (Fe-O) and 1.631 (N-O) Å
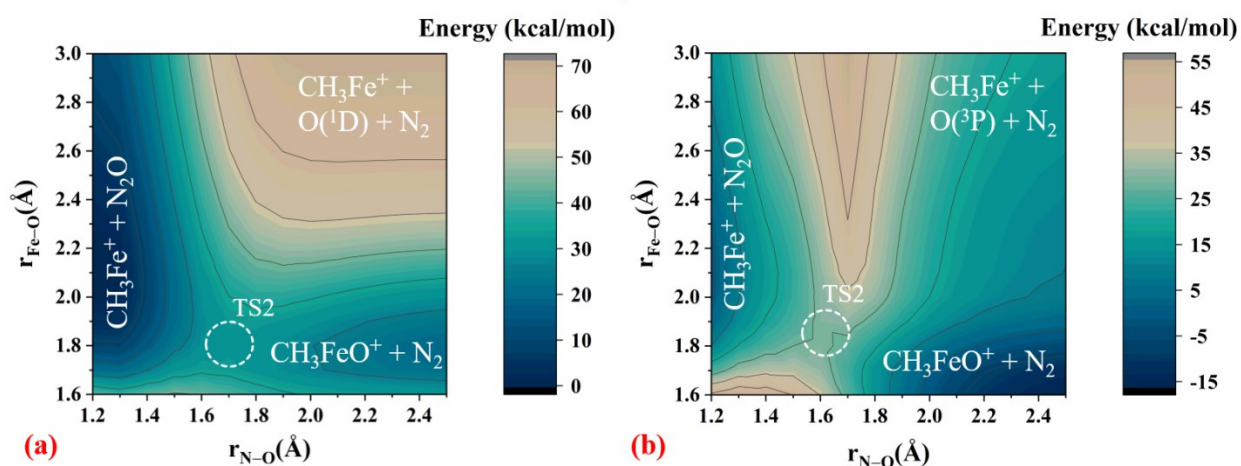
Figure 3.8: Two-dimensional DFT/MN15 (a) and MRCI+Q (b) PEPs for step (2) as a function of the N−O and Fe−O distances. See text for details.

The 2D-PEPs of Figure 3.8 for DFT/MN15/TZ and MRCI/TZ are considerably different. When both distances approach the dissociation limit, DFT/MN15 converges to the CH_3Fe^+ ($^5A'$) + O (~^1D) + N_2 ($^1\Sigma_g^+$) fragments, whereas MRCI goes to the lowest energy fragments CH_3Fe^+ ($^5A'$) + O (^3P) + N_2 ($^1\Sigma_g^+$). Both fragments create quintet spin potential energy surfaces, but the single-reference nature of DFT is unable to capture the shape at the right top corner of the

2D-PEPs (see Figure 3.8). Since the geometry is not optimized at each grid point, the PEPs do not lead to the optimal structures of the reactants or the products.

Recently, we studied the oxidation mechanism of ethene by iodosobenzene (C_6H_5IO), and we found that it is the involvement of $O(^1D)$, which facilitates the transfer of oxygen from iodine to the C-C double bond (making epoxides).[141] Specifically we showed that the closed-shell idosobenzene (C_6H_5I) binds to oxygen via a single dative bond with $O(^1D)$, rather than a double bond with $O(^3P)$, in the following manner $C_6H_5I:\rightarrow O(^1D; 2p_z^0\ 2p_x^2\ 2p_y^2)$. At the transition state, the π-electrons of ethene compete with those of iodine to occupy the $2p_z^0$ orbital, but finally ethene wins since the $2p_x^2$ electrons of $O(^1D)$ attack to its empty π^* orbital making a second bond.

To examine if this is the case here as well, we constructed potential energy curves for several electronic states along two slices of the 2D-PEPs of Figure 3.8. First, we kept fixed the Fe-O distance at 2.8 Å and varied the N-O distance (Figure 3.9), and second, we kept the N-O distance fixed at 2.4 Å and varied the Fe-O distance (Figure 3.10). Figure 3.9 shows clearly that N_2O originates by $O(^1D)$, exactly as iodosobenzene and in harmony with ref. [142], but the spin couplings because of the CH_3Fe^+ presence generate a series of avoided crossings. On the other hand, it is less obvious that CH_3FeO^+ stems diabatically from $O(^1D)$ as well. Initially, the approach of CH_3Fe^+ ($^5A'$) and O (^3P) yields an attractive interaction with a constant slope up to the distance of ~2.1 Å, where the slope changes suddenly leading to the lowest minimum of Figure 3.

10. We believe that this is because of the involvement of O (^1D) depicted with the red dashed line in Figure 3.10. This is also indicated by the DFT/MN15 2D-PEP, where CH_3FeO^+ goes "naturally" to the CH_3Fe^+ + O (~^1D) fragments. Conclusively, we propose a similar mechanism to that observed for the oxidation of ethene: The electron pair (~$3d_\delta^2$) of the in situ $Fe^{2+}(d^6; {}^5D)$ moiety of CH_3Fe^+ is competing with an electron pair of N_2 to occupy the empty 2p-

orbital of O (^{1}D), CH_3Fe^+: $\rightarrow$O$\leftarrow$: N_2. The $3d_\delta$ orbitals are perpendicular to the Fe-CH_3 bond, and that explains also why C, Fe, and O atoms form an almost right angle. The remaining $2p^2$ pairs of oxygen donate only partially electronic density to available iron 3d-orbitals creating the rather ionic Fe-O bond.

Figure 3.9: MRCI+Q-PEPs as a function of the N-O distance for reaction 2. All other parameters are kept fixed at the values of the TS2 structure obtained with MN15, except for the Fe-O distance, which is set equal to 2.8 Å.
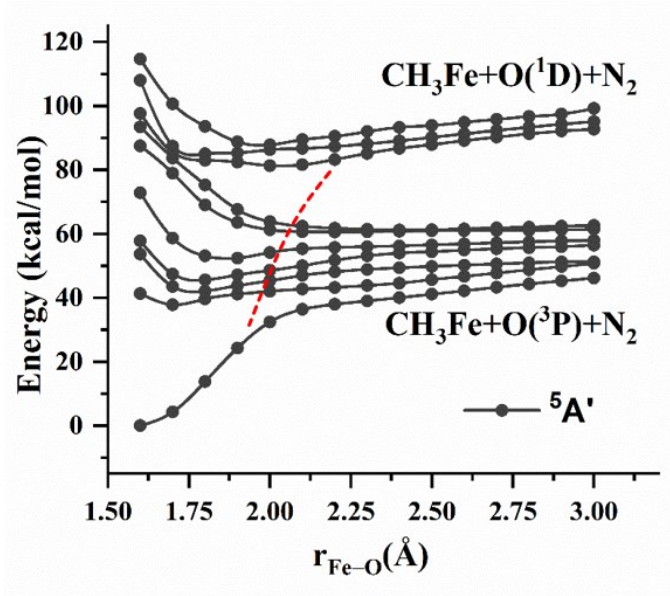
Figure 3.10: MRCI+Q-PEPs as a function of the Fe-O distance for reaction 2. All other parameters are kept fixed at the values of the TS2 structure obtained with MN15, except for the N-O distance, which is set equal to 2.4 Å.

The above analysis suggests that SA-CASSCF calculations are necessary to describe the TS2 region properly. Indeed, we located TS2 after averaging ten states at the CASSCF level but asking only the first MRCI root (DZ basis set is used in this case). Following this method, Fe-O and N-O distances for TS2 are 1.903 and 1.574 Å, respectively, which are longer and shorter than DFT/MN15 by ~0.15 and ~0.05 Å. This discrepancy agrees with the shape of the 2D-PEPs of Figure 3.8. Overall, two reasons caused the convergence issues: 1) the complex shape of the energy landscape and 2) the spin dynamics due to the involvement of many states in the TS region making the CASSCF iterations hard to converge.

To see the effect of the clearly different geometries on the energetics, we performed MRCI(+Q) and CCSD(T) single-point calculations using the MN15/TZ and MRCI/DZ structures. Both state-averaged and state-specific (SS) CASSCF orbitals were probed. The DFT/MN15/TZ activation energy is 39.0 kcal/mol, which is in perfect agreement with SA-CASSCF-MRCI+Q/TZ, SS-CASSCF-MRCI+Q/TZ, and CCSD(T)/TZ values of 40.0, 38.1, and 38.5 kcal/mol when using the DFT/MN15/TZ structure. The corresponding MRCI/TZ values are 47.0 (SA) and 47.6 (SS) kcal/mol. Using the MRCI/DZ geometry, the activation barrier dropped to 34.1, 34.9, and 37.0 kcal/mol at the SA-CASSCF-MRCI+Q/TZ, SS-CASSCF-MRCI+Q/TZ, and CCSD(T)/TZ levels. These values suggest a decrease of ≤ 5 kcal/mol for E_{act}.

Finally, we also investigated the effect of the method on the E_{rxn} using the DFT/MN15/TZ geometries, which should be quite accurate judging by the single-reference character of R2 and P2. The MRCI(+Q) values are -20.0 (-23.6) or (-17.0) -23.1 kcal/mol when a SA-CASSCF or SS-CASSCF is implemented. The Davidson correction brings the SA and SS results closer together.

The CCSD(T)/TZ and MN15/TZ values are -23.1 and -16.7 kcal/mol, respectively. Again, the CCSD(T) energetics agree well with MRCI+Q/TZ, but MN15/TZ predicts smaller exothermicity.

Reaction 4 is competing with reaction 2, since CH_3Fe^+ can in principle react with another C-H bond (CH_4 or CH_3OH) before being oxidized to yield insertion products. However, CH_3Fe^+ seems quite reluctant to coordinate additional units and the addition of CH_4 leads to an exchange of the existing methyl group with the one of the incoming methane, instead of $(CH_3)_2FeH^+$. Figure 3.4 includes the related structures as R4, TS4, and P4=R4. We also made the PEPs along the IRC

for the imaginary frequency of TS4. The inclusion of both quintet and triplet states ensures that the ground state electronic spin remains the same along the IRC (figure 3.11).
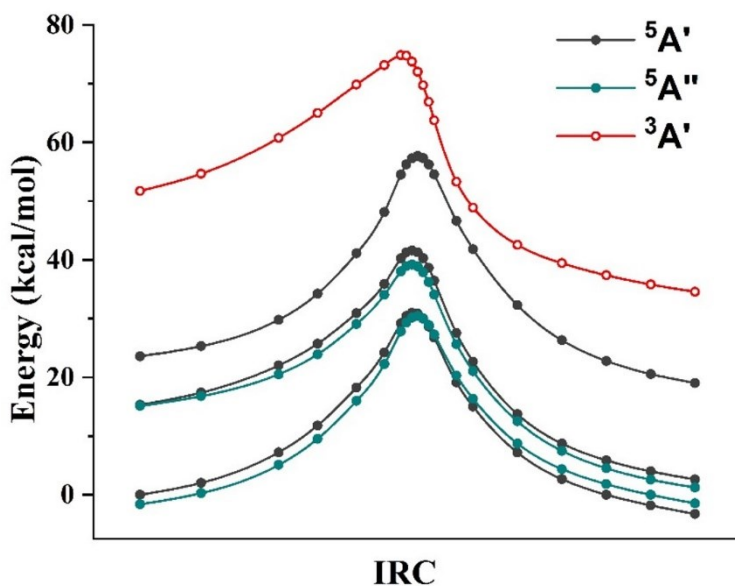
Figure 3.11. MRCI+Q-PEPs for several low-lying electronic states along the reaction coordinate of step (4).

In **reaction 5**, an iron-oxo unit (CH_3FeO^+; $^5A'$) facilitates the conversion of methane to methanol through the radical mechanism described in the introduction. Initially, one H radical is transferred to oxygen making the intermediate I5 = $CH_3FeOH^+ \cdots CH_3$ (dots indicate weak interaction). The CH_3FeOH^+ moiety has a $Fe^{3+}(d^5; {}^6S)$ configuration, which couples with the $^2A_2''$ of CH_3 to give two nearly degenerate $^5A'$ and $^7A'$ states. I5 is a saddle point in the ground state quintet hyper-surface, but it is the global minimum in the septet one. The MRCI+Q PEPs along the IRC is shown in Figure 3.12. I5 finally slides to P5 without a barrier; just a slight bend of the FeOH angle allows CH_3 to rush towards oxygen. The PEPs of the two lowest triplets are above the quintet and cross the septet curve twice. I5 is a local minimum for the lowest triplet $^3A'$ and $^3A''$ states.
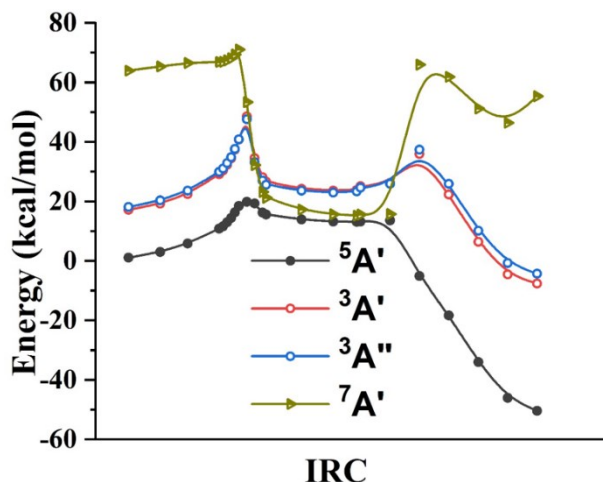
Figure 3.12: MRCI+Q-PEPs for several low-lying electronic states along the reaction coordinate of reaction 5.

Reaction 6 corresponds to the [2+2] insertion of methane to the Fe-O bond. The structures of R6, TS6, and P6 are depicted in Figure 3.4. Observe that the final products are not $(CH_3)_2FeOH^+$, but ethane is released inherently. As in reaction 4, tri-coordinated complexes are not stable. Such a complex would create an in situ $Fe^{4+}(d^4)$ center with a smaller number of "pure" iron orbitals to accommodate four unpaired electrons. Therefore, tri-coordinated complexes are expected to have a ground triplet state with an *in situ* $Fe^{4+}(d^4$; triplet) center. The lowest triplet state $^3P2$ is 3.0 eV higher in energy.[143] Our MN15/TZ calculations confirm that the lowest state of $(CH_3)_2FeOH^+$ is triplet, and lies ~4.5 eV higher than the $FeOH^+(^5A') + C_2H_6$. Instead, the system prefers to eject two ligands and keep the quintet spin multiplicity. The MRCI+Q/TZ PEPs along the IRC path for the lowest quintet and triplet states are given in figure 3.13. It turns out that a triplet state is the lowest one in the TS6 region. Therefore, we obtained the structure of TS6 for the triplet state as well. At the MN15 level the triplet is lower by 9.3 kcal/mol in poor agreement with the MRCI+Q

value of 3.3 kcal/mol. Overall, the system starts as a quintet, changes to a triplet, and then goes back to quintet.
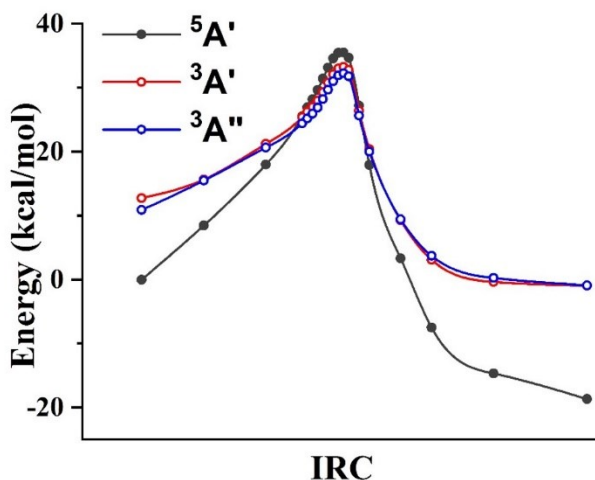
Figure 3.13: MRCI+Q-PEPs for several low-lying electronic states along the reaction coordinate of reaction 6.

Complete catalytic cycle. Figure 3.14 (a) compares the MN15/TZ and CCSD(T)/TZ energy landscapes, and Figure 3.14 (b) includes the zero-point energy (ZPE) and thermally (free energies G) corrected ones. For the latter the CCSD(T) energetics are combined with MN15/TZ ZPE and thermal corrections. In the case of CCSD(T)/TZ the CCSD(T)/DZ geometries are used for all species except for TS2, R5=R6, TS5, TS6, P5, P6, where the MN15/TZ ones are used since we were not able to locate optimal CCSD(T)/DZ structures. Additionally, the TS2 energy in both cases has been reduced by 4.4 kcal/mol to account for the multi-reference character of the system; see the discussion on reaction (2) above. This value is the SA-CASSCF-MRCI+Q/TZ energy difference when the MN15/TZ or the MRCI/DZ optimal geometries are used.
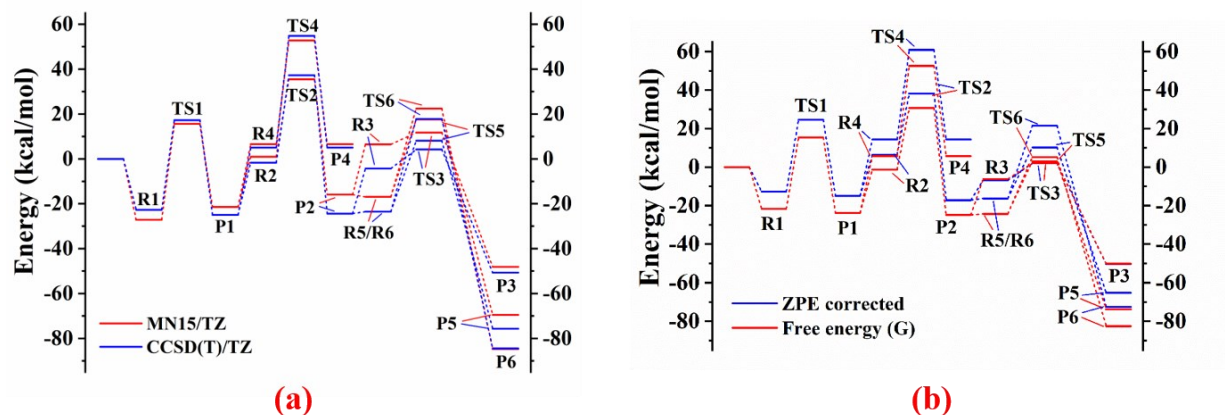
Figure 3.14: (a) Potential energy landscape for the complete MTM conversion catalytic cycle via reactions (1) – (3). The intermediates and transition states of the competing reactions (4) – (6) are also included. (b) ZPE-corrected and free energy landscapes at the CCSD(T)/TZ//MN15/TZ level combined with MN15/TZ ZPE and thermal corrections (298 K and 1 atm).

The MN15/TZ and CCSD(T)/TZ energy diagrams are generally in good agreement, but there are cases with ~10 kcal/mol discrepancies. To investigate if this is due to geometry differences or the different treatment of electron correlation, we constructed the CCSD(T)/TZ energy landscape using the MN15/TZ geometries (Figure 3.15), and we saw that the two plots fall on the top of each other. Therefore, the practice of optimizing the geometries at the low-cost MN15/TZ level and refining the energetics at CCSD(T)/TZ or other high *ab initio* level provides a perfect compromise between accuracy and efficiency.

The construction of an energy landscape at the MRCI, MRCI+Q, CASPT2, or other non-size-extensive method is trickier. Adding the energies of the observer molecules to the intermediates of each step is an erroneous task, and someone must perform calculations where the observer molecules are present in the calculation at long distances (super-molecule approach). This

increases rapidly the number of correlated electrons rendering the calculations extremely demanding. Therefore, although the MRCI(+Q) energetics are very accurate at each step, the exact energy position of the products of one step relative to the reactants of the next requires prohibitive super-molecule calculations. This is an issue not discussed in the literature often.
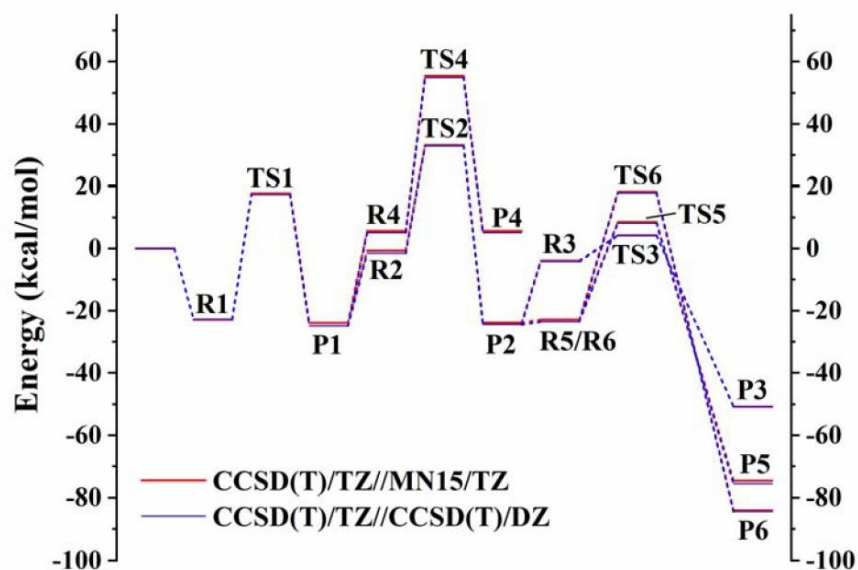
Figure 3.15: Comparison of the CCSD(T)/TZ energy landscapes with CCSD(T)/DZ and MN15/TZ geometries.

Note that the ZPE-corrected energies give always fewer stable intermediates and higher activation barriers than free energies at standard conditions of temperature and pressure (298 K and 1 atm). The ΔG values are analyzed next. Focusing on the chemistry aspect, the first step is exothermic with respect to both the infinitely separated reactants (ISR, zero of the energy scale) and the interacting complex R1 by 24 and 2 kcal/mol, respectively. The energy barrier is less than 20 kcal/mol with respect to ISR. Reaction (2) and (4) compete each other with the oxidation step

providing a lower activation energy. TS2 is the highest energy structure of the cycle lying about 35 kcal/mol higher than ISR.

Finally, the products of reaction (2) can follow three different pathways dictated by TS3, TS5, and TS6. Recall that TS3 leads to the regeneration of the catalyst and the completion of the cycle, which TS5 and TS6 direct to unfavorable paths. Free energies at 298 K locate TS3 only slightly lower than TS5 and TS6, as opposed to the ZPE-corrected values (0 K), which favor clearly TS3. Therefore, lower temperature values will favor reaction (3) over the unwanted reaction (5) and (6). On the other hand, P5 and P6 products are significantly lower than P3, and therefore thermodynamics tend to favor reactions (5) and (6). From a different perspective, reaction (3) is a highly exothermic intra-molecular transformation of the first coordination sphere of the metal. Consequently, it can happen relatively fast before any substrates approach the metal center.

Overall, the investigated cycle shows some promise in developing more efficient MTM catalysts, but certainly needs further optimization. More metals must be considered, while the inclusion of ligands is indispensable to create a "hostile" environment to methanol. Homogeneous catalysis is the suggested route (the next section of this chapter is to this direction), since it offers great flexibility on the catalytic structure and properties.[144]

3.2 Optimization of the Proposed Catalytic Cycle for Methane to Methanol Transformation

In the previous section, we have discussed our results for a complete catalytic cycle for MTM transformation using $FeOCH_3^+$ as a catalyst. And from the energy landscape of the complete cycle, we are convinced that metal methoxide family is very promising as catalyst for MTM transformation. In this section we will present our findings for the optimization of the proposed catalytic cycle. For the optimization, the variable we have used are, formal charge of the metal, effect of ligands and different oxidant. In consistence with the previous section, for this part we have optimized the geometries of all the involved species at MN15/TZ. Harmonic frequency calculations are done to ensure that all the reactants and products are truly minima (all real frequencies), and all the TSs have one imaginary frequency. Starting from the TSs IRC calculations are done to locate the reactants and products. We were not able to perform CCSD(T) or MRCI calculations in this part because of the larger size of the involved species.

The introduction of ligands has dual purposes. First, we want to assess the effect of ligands on the activation barriers of the catalytic cycle. And second, to keep methanol away from the catalytic center to protect it from further oxidation. In the previous section for the bare catalyst (without any ligands), we have used N_2O as an oxidant and the activation barrier of the oxidation step (reaction 2) was 37.0 kcal/mol at CCSD(T)/TZ. That activation barrier of the oxidation step is high considering the feasibility of the catalytic cycle at room temperature. So, in this section we have introduced a more potent oxidant O_3 for the oxidation reaction. Also, in the previous

preliminary assessment (figure 3.3) we found that $FeOCH_3^+$ performed better than $FeOCH_3$. Now, we have employed (+2) charge on the catalytic center to assess its performance. It should be mentioned that the presence of ligands can stabilize the high formal charge on the catalytic center. Also, in this section, we have studied the methanol activation channel and compared the energy landscape with the methane activation channel.

After preliminary calculations of the catalytic cycle, the best combination we have found is for the catalyst $(NH_3)_4FeOCH_3^{2+}$ with an oxidant O_3. In the subsequent sections, we present our findings and compare the energy profile with the previous section. At first, we present the methane activation channel using the catalyst $(NH_3)_4FeOCH_3^{2+}$ and oxidant O_3. Here, the presence of NH_3 ligands is important to stabilize $FeOCH_3^{2+}$ otherwise the species $FeOCH_3^{2+}$ will dissociate into Fe^+ and CH_3O^+. Then we present the methanol activation channel using the same combination of catalyst and oxidant along with a comparison with the methane activation channel.

3.2.1 Methane Activation Channel

We have employed the catalyst $(NH_3)_4FeOCH_3^{2+}$ with an oxidant O_3 for a complete catalytic cycle for methane to methanol transformation. The involved reactions for the catalytic cycle are the following-

Reaction 1: $(NH_3)_4FeOCH_3^{2+} + CH_4 \rightarrow TS1 \rightarrow (NH_3)_4FeCH_3^{2+} + CH_3OH$

Reaction 2: $(NH_3)_4FeCH_3^{2+} + O_3 \rightarrow TS2 \rightarrow (NH_3)_4FeOCH_3^{2+} + O_2$
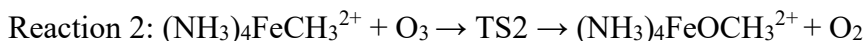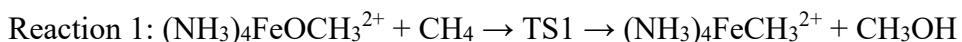
Reaction 1 is the C-H activation reaction of the catalytic cycle where CH_4 attacks the catalytic active site and releases H to produce CH_3OH. This reaction also produces $(NH_3)_4FeCH_3^{2+}$ as a product which goes through an oxidation reaction in the second step (reaction 2) with O_3. Reaction 2 regenerates the catalyst $(NH_3)_4FeOCH_3^{2+}$ along with O_2 as a byproduct. Figure 3.16 depicts the optimized geometries of the involved reactants, TSs, and products.

Figure 3.16: Optimized geometries of the reaction intermediates of the methane activation channel. R1, TS1, P1 and R2, TS2, P2 are the reactant, transition state, and product for reaction 1 and reaction 2 respectively.

Figure 3.17 depicts the energy landscape of the methane activation channel. We have plotted the energy landscape for sextet and quartet spin multiplicity to address any two-state reactivity. For this energy landscape, there are a few very important findings comparable with the energy landscape of figure 3.14 (a). First, for a combination of ligands and (+2) charge on $FeOCH_3$, the species with a terminal Fe-O got destabilized. Because, for the formation of species CH_3FeO^{2+}, in-situ Fe(V) oxidation state is required which is not common. Whereas, to form CH_3OFe^{2+}, Fe(III)

oxidation is needed which is very common. Hence, reaction 3 of the previous section (isomerization) is not present in the case of $(NH_3)_4FeOCH_3^{2+}$ catalyst. Moreover, by using O_3 as an oxidant, the activation barrier of the oxidation step is practically non-existent (< 1 kcal/mol). The catalyst and the reactant of reaction 1 has a sextet ground state but TS1 and the product of reaction 1 (P1) has quartet ground state. So, indeed we see a submerged reaction barrier for reaction 1. Also, the product of reaction 2 is O_2 that has a triplet ground state. Because of the spin coupling with the catalyst (sextet), P2 has an octet ground state.
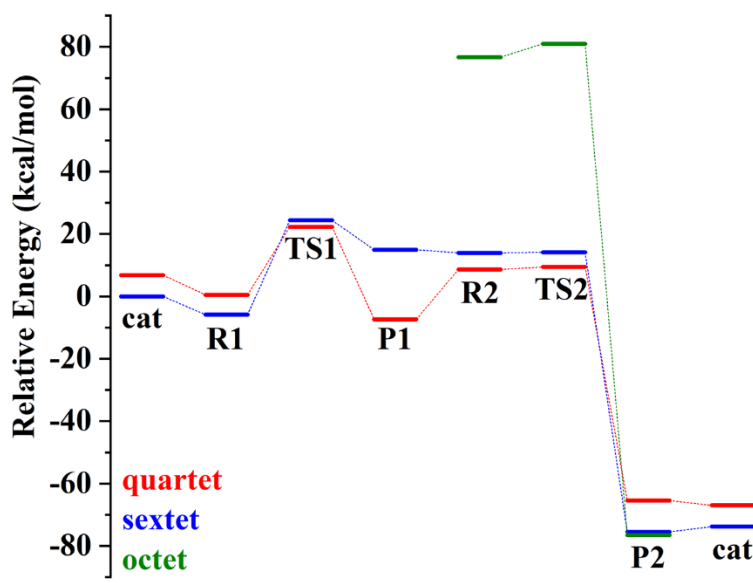
Figure 3.17: Energy landscape for MTM transformation catalytic cycle (methane activation channel only)

3.2.2 Methanol Activation Channel

To address the selectivity issue, we have also studied the methanol activation channel for the same catalytic cycle for MTM transformation. A comparison of the feasibility of methane

activation and methanol activation is made to shed light on the selectivity issue. The methanol

activation channel is comprised of the following reactions-

Reaction 1: $(NH_3)_4FeOCH_3^{2+} + CH_3OH \rightarrow TS1 \rightarrow CH_2OH.... (NH_3)_4Fe^{2+} + CH_3OH$

Reaction 2: $CH_2OH.... (NH_3)_4Fe^{2+} + CH_4 \rightarrow TS2 \rightarrow (NH_3)_4FeCH_3^{2+} + CH_3OH$

Reaction 3: $(NH_3)_4FeCH_3^{2+} + O_3 \rightarrow TS3 \rightarrow (NH_3)_4FeOCH_3^{2+} + O_2$
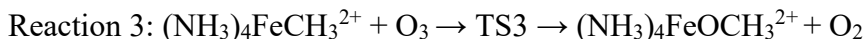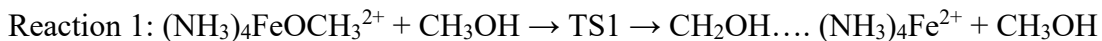
Reaction 1 is the C-H activation reaction of methanol where it forms $CH_2OH.... (NH_3)_4Fe^{2+}$

complex and CH_3OH. The methanol derivative can react with another CH_4 to produce

$(NH_3)_4FeCH_3^{2+}$ complex and CH_3OH in reaction 2. Then the third reaction is the oxidation reaction

with O_3 to regenerate the catalyst. From this catalytic cycle, it is apparent that the methanol

activation channel is regenerating the catalyst and the activation of the C-H bond of methanol

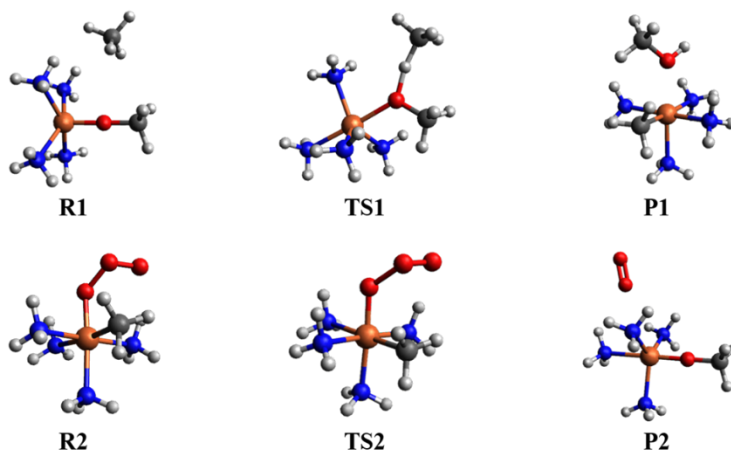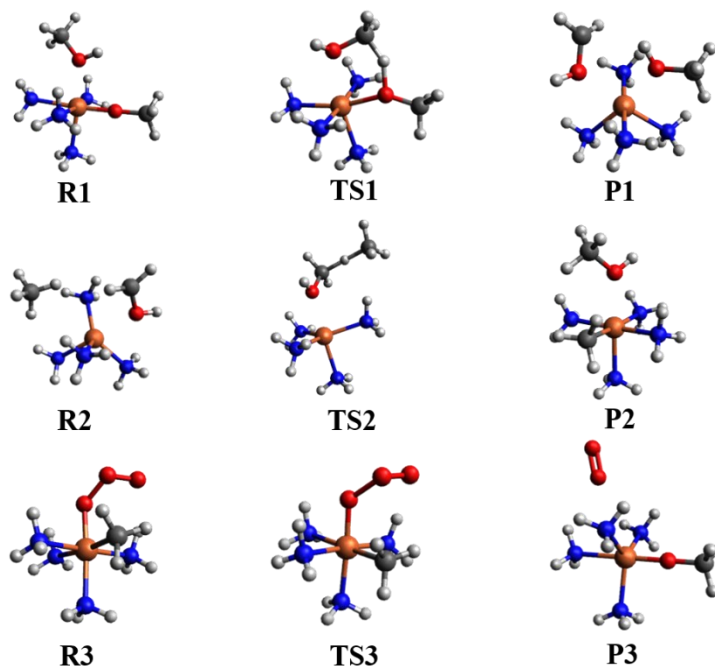**Figure 3.18:** Optimized geometries of the reaction intermediates of the methanol activation

channel. R1, TS1, P1, R2, TS2, P2, R3, TS3, and P3 are the reactant, transition state, and product

for reaction 1, reaction 2, and reaction 3 respectively.

activation is not poisoning the catalyst. Figure 3.18 depicts the optimized structures of the methanol activation channel reaction intermediates. And figure 3.19 is the energy landscape of
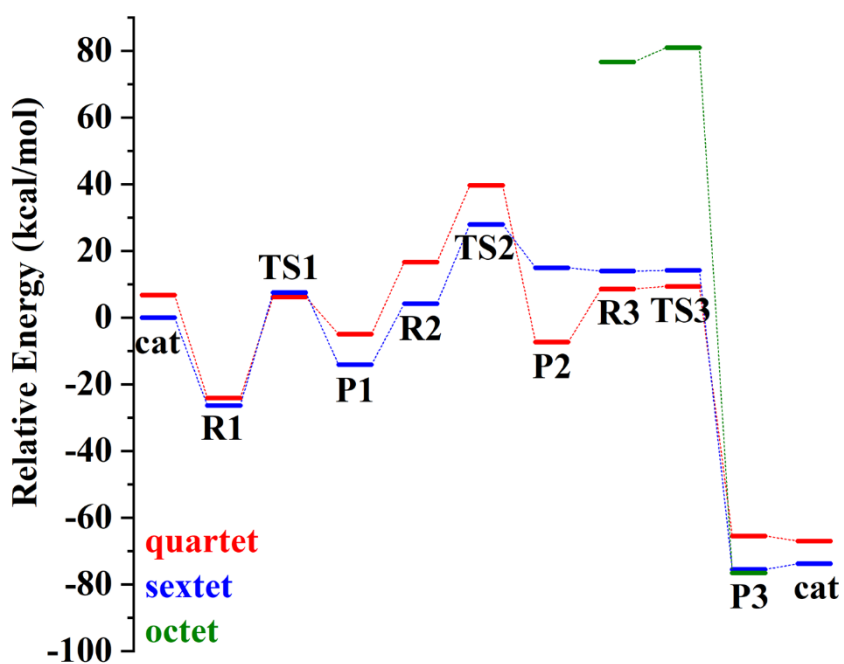
Figure 3.19: Energy landscape for MTM transformation catalytic cycle (methanol activation channel only)

the catalytic cycle. Alike the methane activation channel, this methanol activation channel has also submerged reaction barriers (TS1, TS2). To compare the methane vs methanol activation feasibility, we have charted the activation barriers of all the reactions of these two channels in table 3.2.1.

Table 3.2: Activation barriers (electronic, ZPE corrected, and free energy) for the involved reactions of methane and methanol activation channel in MTM transformation catalytic cycle

Methane Activation Channel

	$\Delta E^{\neq}$ (kcal/mol)	$\Delta E^{\neq}$ (ZPE corrected)(kcal/mol)	$\Delta G^{\neq}$ (kcal/mol)
Reaction 1	28.2	23.5	23.7
Reaction 2	0.7	0.3	0.1

Methanol Activation Channel

	$\Delta E^{\neq}$ (kcal/mol)	$\Delta E^{\neq}$ (ZPE corrected)(kcal/mol)	$\Delta G^{\neq}$ (kcal/mol)
Reaction 1	32.6	28.2	29.6
Reaction 2	23.8	21.3	22.0
Reaction 3	0.7	0.3	0.1

One very important comparison between the methane and methanol activation channel is the activation barriers of the C-H bond activation energy (reaction 1 for both cases). Though the C-H bond of methanol is weaker than the C-H bond of methane, so it is expected that the activation barrier for the C-H activation of methanol should be smaller that methane. But for this catalytic cycle with the catalyst $(NH_3)_4FeOCH_3^{2+}$, the C-H bond activation energy is ~5 kcal/mol larger for methanol than methane. There is a combination of factors responsible for the higher C-H activation barrier of methanol. First, because of the (+2) charge of the catalyst center, the incoming methanol (R1 of figure 3.18 and 3.19) is strongly bound to the catalyst that makes R1 very stable. Whereas, for the C-H activation of methane, methane is only weakly interacting with the catalytic center (R1 of figure 3.16 and 3.17). And second, for the transition state of the C-H bond activation of methanol

(TS1 of 3.2.3 and 3.2.4), O of methanol anchors with the metal due to strong interaction and constraint the optimal bond angle of OHC for the H atom transfer and that causes destabilization of TS1. The combination of these two factors results in a higher activation barrier for the C-H activation of methanol. Also, the C-H activation reaction (reaction 1) of the methanol channel is endothermic. Overall, both the thermodynamic and kinetic factors are not in favor of the first reaction of the methanol channel.

Considering the C-H activation reaction of methanol, reaction 1 produces CH_2OH…. $(NH_3)_4Fe^{2+}$ + CH_3OH. But the product CH_2OH…. $(NH_3)_4Fe^{2+}$ is an isomer of our catalyst $(NH_3)_4FeOCH_3^{2+}$. So, it will be significant if there is any reaction mechanism with which it will be possible to regenerate the catalyst using an isomerization reaction. Indeed, we have located a reaction mechanism for the isomerization of the methanol derivative that eventually regenerate the catalyst. Figure 3.20 depicts the isomers of the catalyst which is the product of reaction 1 of the methanol activation channel. The isomerization reaction –

$$(NH_3)_4Fe^{2+}….CH_2OH \rightarrow TS1 \rightarrow (NH_3)_4FeOCH_3^{2+}$$
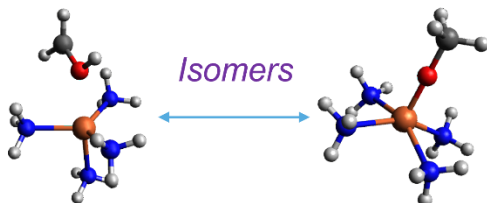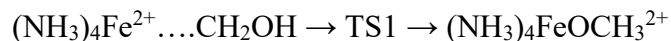
Figure 3.20: Catalyst and its isomer produced in reaction 1 of the methanol activation channel.

In figure 3.21, complete energy landscape of the methanol activation channel is presented with the isomerization step that regenerates the catalyst. The activation barrier for the isomerization step is still large (38 kcal/mol) but can be optimized by different selection of metal and ligands.
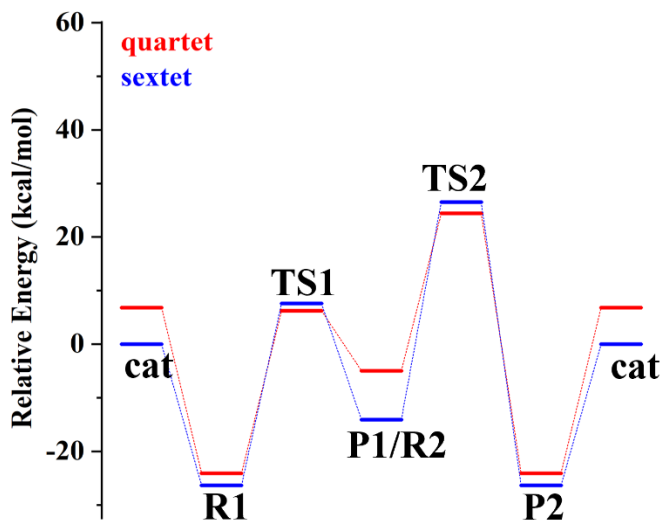
Figure 3.21: Energy landscape for MTM transformation catalytic cycle with isomerization of the methanol derivative.

3.3 Conclusion

The conversion of methane to methanol catalyzed by the $FeOCH_3^+$ transition metal methoxide was investigated by means of high-level electronic structure calculations. The goal of the present work is dual. First, we assessed the computational efficiency of different quantum chemical methodologies, and second, we explored the energy landscape of the studied catalytic cycle.

We found that a combined DFT and *ab-initio* theoretical work provides a low computational cost, relatively fast, and quite accurate investigation. DFT/MN15/TZ and CCSD(T)/DZ optimized structures were used to get CCSD(T)/TZ energetics, while DFT/MN15/TZ frequencies were employed to evaluate ZPE and thermal corrections. MRCI+Q calculations were also invoked to construct PEPs along the reaction coordinate of each step. This work demonstrates that despite the tremendous improvement on the technical part of the existing methodologies, none of them can serve as an accurate standalone method for the study of catalytic systems as small as the present one. An important finding is that the accuracy in geometry plays small role compared to the level of the electron correlation treatment.

The proposed catalytic cycle for MTM transformation using $FeOCH_3^+$ has promising features that can avoid the drawbacks of the commonly used metal oxide catalysts. Though this catalytic cycle can be further optimized which we have done in the second part of the project. For the optimization, first, we have used $FeOCH_3^{2+}$ catalytic center coordinated with four ammonia ligands. A combination of (+2) charge on the active site and the presence of ligand allowed us to directly regenerate the catalyst through oxidation. Hence, we were able to eliminate the

complicated side reactions from the initial catalytic cycle. Then, we have utilized a stronger oxidant O_3 to reduce the activation barrier of the oxidation step. Also, we have constructed the energy landscape for the methanol activation channel and compared it with the methane activation channel to address the selectivity issue. **The methanol channel has a higher activation barrier in the C-H activation step than the methane activation channel, which is unique in the sense that the C-H bond of methanol is weaker than the C-H bond of methane.** Also, the C-H bond activation of methanol is thermodynamically unstable (endothermic). Moreover, the product of the methanol activation is an isomer of the catalyst. And it is possible to regenerate the catalyst following an isomerization reaction. Considering all these factors, we believe that the catalyst $(NH_3)_4FeOCH_3{}^{2+}$ with oxidant O_3 is very promising for MTM transformation where the activation barrier for the C-H bond activation of methane is moderate (28.2 kcal/mol) and the methanol activation is kinetically and thermodynamically unfavorable.

As a future direction, we believe that the complete catalytic cycle is very promising and any future work using different metal-ligand combination for the proposed catalytic cycle is worth trying. This fundamental analysis on the proposed catalytic cycle can be used as a reference point for further detailed investigation for practical application.

Reference

1. S. N. Khan and E. Miliordos, *Physical Chemistry Chemical Physics*, 2017, 19, 18152-18155.
2. B. Wang, Y.-M. Lee, W.-Y. Tcho, S. Tussupbayev, S.-T. Kim, Y. Kim, M. S. Seo, K.-B. Cho, Y. Dede, B. C. Keegan, T. Ogura, S. H. Kim, T. Ohta, M.-H. Baik, K. Ray, J. Shearer and W. Nam, *Nature Communications*, 2017, 8, 14839.
3. K. Qin, C. D. Incarvito, A. L. Rheingold and K. H. Theopold, *Journal of the American Chemical Society*, 2002, 124, 14008-14009.
4. W. Rasheed, A. Draksharapu, S. Banerjee, V. G. Young Jr, R. Fan, Y. Guo, M. Ozerov, J. Nehrkorn, J. Krzystek, J. Telser and L. Que Jr, *Angewandte Chemie International Edition*, 2018, 57, 9387-9391.
5. D. F. Leto, A. A. Massie, D. B. Rice and T. A. Jackson, *Journal of the American Chemical Society*, 2016, 138, 15413-15424.
6. K. H. Bok, M. M. Lee, G. R. You, H. M. Ahn, K. Y. Ryu, S.-J. Kim, Y. Kim and C. Kim, *Chemistry – A European Journal*, 2017, 23, 3117-3125.
7. C. D. Nunes, P. D. Vaz, V. Félix, L. F. Veiros, T. Moniz, M. Rangel, S. Realista, A. C. Mourato and M. J. Calhorda, *Dalton Transactions*, 2015, 44, 5125-5138.
8. H. Kotani, S. Kaida, T. Ishizuka, K. Mieda, M. Sakaguchi, T. Ogura, Y. Shiota, K. Yoshizawa and T. Kojima, *Inorganic Chemistry*, 2018, 57, 13929-13936.
9. H. Kotani, S. Kaida, T. Ishizuka, M. Sakaguchi, T. Ogura, Y. Shiota, K. Yoshizawa and T. Kojima, *Chemical Science*, 2015, 6, 945-955.
10. J. Cho, J. Woo, J. Eun Han, M. Kubo, T. Ogura and W. Nam, *Chemical Science*, 2011, 2, 2057-2062.
11. R. L. Halbach, D. Gygi, E. D. Bloch, B. L. Anderson and D. G. Nocera, *Chemical Science*, 2018, 9, 4524-4528.
12. R. J. Martinie, C. J. Pollock, M. L. Matthews, J. M. Bollinger, C. Krebs and A. Silakov, *Inorganic Chemistry*, 2017, 56, 13382-13389.
13. A. Bodner, P. Jeske, T. Weyhermueller, K. Wieghardt, E. Dubler, H. Schmalle and B. Nuber, *Inorganic Chemistry*, 1992, 31, 3737-3748.
14. B. S. Mandimutsira, B. Ramdhanie, R. C. Todd, H. Wang, A. A. Zareba, R. S. Czernuszewicz and D. P. Goldberg, *Journal of the American Chemical Society*, 2002, 124, 15170-15171.
15. J. M. Stauber and C. C. Cummins, *Inorganic Chemistry*, 2017, 56, 3022-3029.
16. A. M. P. Comba, *Inorg. Chem.*, 1987, 26, 1315–1323.
17. V. C. C. Wang, S. Maji, P. P. Y. Chen, H. K. Lee, S. S. F. Yu and S. I. Chan, *Chemical Reviews*, 2017, 117, 8574-8621.
18. E. Miliordos and A. Mavridis, *The Journal of Physical Chemistry A*, 2007, 111, 1953-1965.
19. E. Miliordos and A. Mavridis, *The Journal of Physical Chemistry A*, 2010, 114, 8536-8572.
20. C. N. Sakellaris and A. Mavridis, *The Journal of Physical Chemistry A*, 2012, 116, 6935-6949.
21. C. N. Sakellaris and A. Mavridis, *The Journal of Chemical Physics*, 2013, 138, 054308.

22.   C. N. Sakellaris, E. Miliordos and A. Mavridis, *The Journal of Chemical Physics*, 2011, 134, 234308.
23.   C. N. Sakellaris, A. Papakondylis and A. Mavridis, *The Journal of Physical Chemistry A*, 2010, 114, 9333-9341.
24.   S. Midda, N. C. Bera, I. Bhattacharyya and A. K. Das, *Journal of Molecular Structure: THEOCHEM*, 2006, 761, 17-20.
25.   M. L. Polak, M. K. Gilles, J. Ho and W. C. Lineberger, *The Journal of Physical Chemistry*, 1991, 95, 3460-3463.
26.   H. Xian, Z. X. Cao, X. Xu, X. Lu and Q. E. Zhang, *Chemical Physics Letters*, 2000, 326, 485-493.
27.   Y. Nakao, K. Hirao and T. Taketsugu, *The Journal of Chemical Physics*, 2001, 114, 7935-7940.
28.   B. A. Jackson and E. Miliordos, *Physical Chemistry Chemical Physics*, 2020, 22, 6606-6618.
29.   I. R. Ariyarathna and E. Miliordos, *Physical Chemistry Chemical Physics*, 2021, 23, 1437-1442.
30.   C. J. Ballhausen and H. B. Gray, *Inorganic Chemistry*, 1962, 1, 111-122.
31.   T. Z. H. Gani and H. J. Kulik, *ACS Catalysis*, 2018, 8, 975-986.
32.   A. Nandy, J. Zhu, J. P. Janet, C. Duan, R. B. Getman and H. J. Kulik, *ACS Catalysis*, 2019, 9, 8243-8255.
33.   J. Fišer, K. Franzreb, J. Lörinčík and P. Williams, *European Journal of Mass Spectrometry*, 2009, 15, 315-324.
34.   D. Schröder, M. Engeser, H. Schwarz and J. N. Harvey, *ChemPhysChem*, 2002, 3, 584-591.
35.   S. Almenia, M. Mogren Al Mogren, D. Ben Abdallah, R. Linguerri and M. Hochlaf, *Chemical Physics Letters*, 2016, 646, 142-147.
36.   L. Gonçalves dos Santos, K. Franzreb and F. R. Ornellas, *Chemical Physics Letters*, 2021, 771, 138525.
37.   Z. Parsons, C. Leavitt, T. Duong, G. S. Groenewold, G. L. Gresham and M. J. Van Stipdonk, *The Journal of Physical Chemistry A*, 2006, 110, 11627-11635.
38.   K. T. H. Johansen, *Chem. Phys. Lett.*, 1985, 116, 155-159.
39.   E. E. Claveau and E. Miliordos, *Physical Chemistry Chemical Physics*, 2021, DOI: 10.1039/D1CP02492B.
40.   Y. Shimoyama and T. Kojima, *Inorganic Chemistry*, 2019, 58, 9517-9542.
41.   W. M. Haynes, *Taylor & Francis*, 2012.
42.   H. Schwarz, *Angewandte Chemie International Edition*, 2011, 50, 10096-10115.
43.   H. Schwarz, P. González-Navarrete, J. Li, M. Schlangen, X. Sun, T. Weiske and S. Zhou, *Organometallics*, 2017, 36, 8-17.
44.   H. Schwarz, S. Shaik and J. Li, *Journal of the American Chemical Society*, 2017, 139, 17201-17212.
45.   F. Roudesly, J. Oble and G. Poli, *Journal of Molecular Catalysis A: Chemical*, 2017, 426, 275-296.
46.   K. Ray, F. F. Pfaff, B. Wang and W. Nam, *Journal of the American Chemical Society*, 2014, 136, 13942-13958.
47.   T. L. Poulos, *Chemical Reviews*, 2014, 114, 3919-3962.

48. S. Sahu and D. P. Goldberg, *Journal of the American Chemical Society*, 2016, 138, 11410-11428.
49. J. C. Price, E. W. Barr, T. E. Glass, C. Krebs and J. M. Bollinger, *Journal of the American Chemical Society*, 2003, 125, 13008-13009.
50. J. M. Elkins, M. J. Ryle, I. J. Clifton, J. C. Dunning Hotopp, J. S. Lloyd, N. I. Burzlaff, J. E. Baldwin, R. P. Hausinger and P. L. Roach, *Biochemistry*, 2002, 41, 5185-5192.
51. S. D. Wong, M. Srnec, M. L. Matthews, L. V. Liu, Y. Kwak, K. Park, C. B. Bell Iii, E. E. Alp, J. Zhao, Y. Yoda, S. Kitao, M. Seto, C. Krebs, J. M. Bollinger and E. I. Solomon, *Nature*, 2013, 499, 320-323.
52. M. L. Matthews, C. M. Krest, E. W. Barr, F. H. Vaillancourt, C. T. Walsh, M. T. Green, C. Krebs and J. M. Bollinger, *Biochemistry*, 2009, 48, 4331-4343.
53. W. Nam, *Accounts of Chemical Research*, 2007, 40, 522-531.
54. W. Nam, *Accounts of Chemical Research*, 2015, 48, 2415-2423.
55. W. N. Oloo and L. Que, *Accounts of Chemical Research*, 2015, 48, 2612-2621.
56. M. Puri and L. Que, *Accounts of Chemical Research*, 2015, 48, 2443-2452.
57. L. Que, *Accounts of Chemical Research*, 2007, 40, 493-500.
58. V. I. Sobolev, K. A. Dubkov, O. V. Panna and G. I. Panov, *Catalysis Today*, 1995, 24, 251-252.
59. K. A. Dubkov, V. I. Sobolev, E. P. Talsi, M. A. Rodkin, N. H. Watkins, A. A. Shteinman and G. I. Panov, *Journal of Molecular Catalysis A: Chemical*, 1997, 123, 155-161.
60. B. E. R. Snyder, P. Vanelderen, M. L. Bols, S. D. Hallaert, L. H. Böttger, L. Ungur, K. Pierloot, R. A. Schoonheydt, B. F. Sels and E. I. Solomon, *Nature*, 2016, 536, 317-321.
61. P. Liao, R. B. Getman and R. Q. Snurr, *ACS Applied Materials & Interfaces*, 2017, 9, 33484-33492.
62. D. J. Xiao, E. D. Bloch, J. A. Mason, W. L. Queen, M. R. Hudson, N. Planas, J. Borycz, A. L. Dzubak, P. Verma, K. Lee, F. Bonino, V. Crocellà, J. Yano, S. Bordiga, D. G. Truhlar, L. Gagliardi, C. M. Brown and J. R. Long, *Nature Chemistry*, 2014, 6, 590-595.
63. H. Hirao, W. K. H. Ng, A. M. P. Moeljadi and S. Bureekaew, *ACS Catalysis*, 2015, 5, 3287-3291.
64. P. Verma, K. D. Vogiatzis, N. Planas, J. Borycz, D. J. Xiao, J. R. Long, L. Gagliardi and D. G. Truhlar, *Journal of the American Chemical Society*, 2015, 137, 5770-5781.
65. X. Engelmann, I. Monte-Pérez and K. Ray, *Angewandte Chemie International Edition*, 2016, 55, 7632-7649.
66. J. Olsen, B. O. Roos, P. Jo/rgensen and H. J. r. A. Jensen, *The Journal of Chemical Physics*, 1988, 89, 2185-2192.
67. B. O. Roos, P. R. Taylor and P. E. M. Sigbahn, *Chemical Physics*, 1980, 48, 157-173.
68. P. J. Knowles and H.-J. Werner, *Chemical Physics Letters*, 1988, 145, 514-522.
69. H. J. Werner and P. J. Knowles, *The Journal of Chemical Physics*, 1988, 89, 5803-5814.
70. T. H. Dunning, *The Journal of Chemical Physics*, 1989, 90, 1007-1023.
71. R. A. Kendall, T. H. Dunning and R. J. Harrison, *The Journal of Chemical Physics*, 1992, 96, 6796-6806.
72. P. J. K. H.-J. Werner, G. Knizia, F. R. Manby, M. Schütz, P. Celani, T. Korona, R. Lindh, A. Mitrushenkov, G. Rauhut, K. R. Shamasundar, T. B. Adler, R. D. Amos, A. Bernhardsson, A. Berning, D. L. Cooper, M. J. O. Deegan, A. J. Dobbyn, F. Eckert, E. Goll, C. Hampel, A. Hesselmann, G. Hetzer, T. Hrenar, G. Jansen, C. Köppl, Y. Liu, A. W. Lloyd, R. A. Mata, A. J. May, S. J. McNicholas, W. Meyer, M. E. Mura, A. Nicklass,

D. P. O'Neill, P. Palmieri, D. Peng, K. Pflüger, R. Pitzer, M. Reiher, T. Shiozaki, H. Stoll, A. J. Stone, R. Tarroni, T. Thorsteinsson and M. Wang, 2012.

73. J. K. Kirkland, S. N. Khan, B. Casale, E. Miliordos and K. D. Vogiatzis, *Physical Chemistry Chemical Physics*, 2018, 20, 28786-28795.

74. W. M. Haynes, ed., *CRC Handbook of Chemistry and Physics*, Taylor and Francis, Boca Raton, FL, 2012.

75. A. Kramida, Y. Ralchenko and J. Reader, NIST Atomic Spectra Database (ver. 5.5.6), http://physics.nist.gov/asd).

76. E. Broclawik, R. Yamauchi, A. Endou, M. Kubo and A. Miyamoto, *Int. J. Quantum Chem.*, 1997, 61, 673-682.

77. G. Fu, X. Xu, X. Lu and H. Wan, *J. Am. Chem. Soc.*, 2005, 127, 3989-3996.

78. C. Gao, H.-Q. Yang, J. Xu, S. Qin and C.-W. Hu, *J. Comput. Chem.*, 2010, 31, 938-953.

79. X. Xu, F. Faglioni and W. A. Goddard, *J. Phys. Chem. A*, 2002, 106, 7171-7176.

80. A. Citra and L. Andrews, *J. Phys. Chem. A*, 1999, 103, 4845-4854.

81. J. Gengler, T. Ma, A. G. Adam and T. C. Steimle, *J. Chem. Phys.*, 2007, 126, 134304.

82. R. F. Heuff, W. J. Balfour and A. G. Adam, *J. Mol. Spectrosc.*, 2002, 216, 136-150.

83. R. H. Jensen, S. G. Fougère and W. J. Balfour, *Chem. Phys. Lett.*, 2003, 370, 106-111.

84. X. Li and L.-S. Wang, *J. Chem. Phys.*, 1998, 109, 5264-5268.

85. M. R. Beltrán, F. Buendía Zamudio, V. Chauhan, P. Sen, H. Wang, Y. J. Ko and K. Bowen, *Eur. Phys. J. D*, 2013, 67, 63.

86. G. J. Mains and J. M. White, *J. Phys. Chem.* , 1991, 95, 112-118.

87. P. E. M. Siegbahn, *Chem. Phys. Lett.*, 1993, 201, 15-23.

88. P. Song, W. Guan, C. Yao, Z. M. Su, Z. J. Wu, J. D. Feng and L. K. Yan, *Theor. Chem. Acc.*, 2007, 117, 407-415.

89. F. Stevens, V. Van Speybroeck, I. Carmichael, F. Callens and M. Waroquier, *Chem. Phys. Lett.*, 2006, 421, 281-286.

90. B. Suo, H. Han, Y. Lei, G. Zhai, Y. Wang and Z. Wen, *J. Chem. Phys.*, 2009, 130, 094304.

91. H. B. Gray and J. R. Winkler, *Accounts of Chemical Research*, 2018, 51, 1850-1857.

92. N. M. S. Almeida, I. R. Ariyarathna and E. Miliordos, *The Journal of Physical Chemistry A*, 2019, 123, 9336-9344.

93. K. A. Peterson, D. Figgen, M. Dolg and H. Stoll, *J. Chem. Phys.*, 2007, 126, 124101.

94. H. S. Yu, X. He, S. L. Li and D. G. Truhlar, *Chem. Sci.*, 2016, 7, 5032-5051.

95. G. W. T. M. J. Frisch, H. B. Schlegel, G. E. Scuseria, M. A. Robb, J. R. Cheeseman, G. Scalmani, V. Barone, G. A. Petersson, H. Nakatsuji, X. Li, M. Caricato, A. V. Marenich, J. Bloino, B. G. Janesko, R. Gomperts, B. Mennucci, H. P. Hratchian, J. V. Ortiz, A. F. Izmaylov, J. L. Sonnenberg, D. Williams-Young, F. Ding, F. Lipparini, F. Egidi, J. Goings, B. Peng, A. Petrone, T. Henderson, D. Ranasinghe, V. G. Zakrzewski, J. Gao, N. Rega, G. Zheng, W. Liang, M. Hada, M. Ehara, K. Toyota, R. Fukuda, J. Hasegawa, M. Ishida, T. Nakajima, Y. Honda, O. Kitao, H. Nakai, T. Vreven, K. Throssell, J. A. Montgomery, Jr., J. E. Peralta, F. Ogliaro, M. J. Bearpark, J. J. Heyd, E. N. Brothers, K. N. Kudin, V. N. Staroverov, T. A. Keith, R. Kobayashi, J. Normand, K. Raghavachari, A. P. Rendell, J. C. Burant, S. S. Iyengar, J. Tomasi, M. Cossi, J. M. Millam, M. Klene, C. Adamo, R. Cammi, J. W. Ochterski, R. L. Martin, K. Morokuma, O. Farkas, J. B. Foresman, and D. J. Fox, *Journal*, 2016, Revision A.03.

96. S. N. Khan and E. Miliordos, *Inorganic Chemistry*, 2021, 60, 16111-16119.

97.	A. R. Kulkarni, Z.-J. Zhao, S. Siahrostami, J. K. Nørskov and F. Studt, *Catalysis Science & Technology*, 2018, 8, 114-123.
98.	M. Ravi, M. Ranocchiari and J. A. van Bokhoven, *Angewandte Chemie International Edition*, 2017, 56, 16464-16483.
99.	P. Schwach, X. Pan and X. Bao, *Chemical Reviews*, 2017, 117, 8497-8520.
100.	Z. Zakaria and S. K. Kamarudin, *Renewable and Sustainable Energy Reviews*, 2016, 65, 250-261.
101.	P. V. L. Reddy, K.-H. Kim and H. Song, *Renewable and Sustainable Energy Reviews*, 2013, 24, 578-585.
102.	J. Yin, S. Su, X. X. Yu and Y. Weng, *Applied Energy*, 2010, 87, 2102-2108.
103.	H. D. Gesser, N. R. Hunter and C. B. Prakash, *Chemical Reviews*, 1985, 85, 235-244.
104.	M. D. Khokhar, R. S. Shukla and R. V. Jasra, *Journal of Molecular Catalysis A: Chemical*, 2009, 299, 108-116.
105.	M. J. da Silva, *Fuel Processing Technology*, 2016, 145, 42-61.
106.	L. Soussan, N. Pen, M.-P. Belleville, J. S. Marcano and D. Paolucci-Jeanjean, *Journal of Biotechnology*, 2016, 222, 117-142.
107.	G. Ménard, J. A. Hatnean, H. J. Cowley, A. J. Lough, J. M. Rawson and D. W. Stephan, *Journal of the American Chemical Society*, 2013, 135, 6446-6449.
108.	G. Ménard and D. W. Stephan, *Angewandte Chemie International Edition*, 2012, 51, 4409-4412.
109.	T. Ikuno, J. Zheng, A. Vjunov, M. Sanchez-Sanchez, M. A. Ortuño, D. R. Pahls, J. L. Fulton, D. M. Camaioni, Z. Li, D. Ray, B. L. Mehdi, N. D. Browning, O. K. Farha, J. T. Hupp, C. J. Cramer, L. Gagliardi and J. A. Lercher, *Journal of the American Chemical Society*, 2017, 139, 10294-10301.
110.	Á. Szécsényi, G. Li, J. Gascon and E. A. Pidko, *Chemical Science*, 2018, 9, 6765-6773.
111.	J. G. Vitillo, A. Bhan, C. J. Cramer, C. C. Lu and L. Gagliardi, *ACS Catalysis*, 2019, 9, 2870-2879.
112.	J. Shan, M. Li, L. F. Allard, S. Lee and M. Flytzani-Stephanopoulos, *Nature*, 2017, 551, 605-608.
113.	L. Sushkevich Vitaly, D. Palagin, M. Ranocchiari and A. van Bokhoven Jeroen, *Science*, 2017, 356, 523-527.
114.	A. A. Latimer, A. Kakekhani, A. R. Kulkarni and J. K. Nørskov, *ACS Catalysis*, 2018, 8, 6894-6907.
115.	R. Palkovits, M. Antonietti, P. Kuhn, A. Thomas and F. Schüth, *Angewandte Chemie International Edition*, 2009, 48, 6909-6912.
116.	M. Muehlhofer, T. Strassner and W. A. Herrmann, *Angewandte Chemie International Edition*, 2002, 41, 1745-1747.
117.	B. L. Conley, W. J. Tenn, K. J. H. Young, S. K. Ganesh, S. K. Meier, V. R. Ziatdinov, O. Mironov, J. Oxgaard, J. Gonzales, W. A. Goddard and R. A. Periana, *Journal of Molecular Catalysis A: Chemical*, 2006, 251, 8-23.
118.	R. H. Crabtree, *Chemical Reviews*, 1995, 95, 987-1007.
119.	J. F. Hartwig, *Journal of the American Chemical Society*, 2016, 138, 2-24.
120.	B. G. Hashiguchi, S. M. Bischof, M. M. Konnick and R. A. Periana, *Accounts of Chemical Research*, 2012, 45, 885-898.
121.	A. Holmen, *Catalysis Today*, 2009, 142, 2-8.

122. R. A. Periana, G. Bhalla, W. J. Tenn, K. J. H. Young, X. Y. Liu, O. Mironov, C. J. Jones and V. R. Ziatdinov, *Journal of Molecular Catalysis A: Chemical*, 2004, 220, 7-25.
123. J. A. Labinger and J. E. Bercaw, *Nature*, 2002, 417, 507-514.
124. P. Chawdhury, K. V. S. S. Bhargavi and C. Subrahmanyam, *Sustainable Energy & Fuels*, 2021, 5, 3351-3362.
125. W. A. Donald, C. J. McKenzie and R. A. J. O'Hair, *Angewandte Chemie International Edition*, 2011, 50, 8379-8383.
126. K. M. Carsch and T. R. Cundari, *Computational and Theoretical Chemistry*, 2012, 980, 133-137.
127. A. Najafian and T. R. Cundari, *Inorganic Chemistry*, 2017, 56, 12282-12290.
128. A. Marzouk, M. E. Alikhani, B. Madebène, B. Tremblay and J.-P. Perchard, *The Journal of Physical Chemistry A*, 2013, 117, 1697-1705.
129. E. M. Cunningham, A. S. Gentleman, P. W. Beardsmore and S. R. Mackenzie, *Molecular Physics*, 2019, 117, 2990-3000.
130. D. Trogolo, J. S. Arey and P. R. Tentscher, *The Journal of Physical Chemistry A*, 2019, 123, 517-536.
131. J. Campos, J. López-Serrano, R. Peloso and E. Carmona, *Chemistry – A European Journal*, 2016, 22, 6432-6457.
132. N. Nakatani and M. Hada, *Journal of Computational Chemistry*, 2019, 40, 414-420.
133. A. Fiedler, D. Schroeder, S. Shaik and H. Schwarz, *Journal of the American Chemical Society*, 1994, 116, 10734-10741.
134. K. D. Vogiatzis, M. V. Polynski, J. K. Kirkland, J. Townsend, A. Hashemi, C. Liu and E. A. Pidko, *Chemical Reviews*, 2019, 119, 2453-2523.
135. S. M. Tekarli, M. L. Drummond, T. G. Williams, T. R. Cundari and A. K. Wilson, *The Journal of Physical Chemistry A*, 2009, 113, 8607-8614.
136. N. B. Balabanov and K. A. Peterson, *The Journal of Chemical Physics*, 2005, 123, 064107.
137. E. Miliordos, J. F. Harrison and K. L. C. Hunt, *The Journal of Chemical Physics*, 2011, 135, 144111.
138. E. Miliordos, J. F. Harrison and K. L. C. Hunt, *The Journal of Chemical Physics*, 2013, 138, 114305.
139. S. N. Khan and E. Miliordos, *The Journal of Physical Chemistry A*, 2019, 123, 5590-5599.
140. W. Jiang, N. J. DeYonker and A. K. Wilson, *Journal of Chemical Theory and Computation*, 2012, 8, 460-468.
141. S. N. Khan and E. Miliordos, *Phys. Chem. Chem. Phys.*, 2017, 19, 18152-18155.
142. A. Kalemos, I. R. Ariyaranthna, S. N. Khan, E. Miliordos and A. Mavridis, *Comput. Theor. Chem.*, 2019, DOI: https://doi.org/10.1016/j.comptc.2019.02.014.
143. N. Forsberg and P.-Å. Malmqvist, *Chemical Physics Letters*, 1997, 274, 196-204.
144. B. Cornils and W. A. Herrmann, *J. Catal.*, 2003, 216, 23-31.

Appendix A

Supporting Materials for Chapter 2

- J. K. Kirkland, **S. N. Khan**, B. Casale, E. Miliordos and K. D. Vogiatzis, *Phys. Chem. Chem. Phys.*, 2018, **20**, 28786

- **S. N. Khan**, and E. Miliordos, *Inorg, Chem.* 2021, *60*, 16111-16119.

PAPER

Check for updates

Ligand field effects on the ground and excited states of reactive FeO^{2+} species†

Justin K. Kirkland,[a] Shahriar N. Khan,[b] Bryan Casale,[a] Evangelos Miliordos [ID] *[b] and Konstantinos D. Vogiatzis [ID] *[a]

High-valent Fe(IV)-oxo species have been found to be key oxidizing intermediates in the mechanisms of mononuclear iron heme and non-heme enzymes that can functionalize strong C–H bonds. Biomimetic Fe(IV)-oxo molecular complexes have been successfully synthesized and characterized, but their catalytic reactivity is typically lower than that of the enzymatic analogues. The C–H activation step proceeds through two competitive mechanisms, named σ- and π-channels. We have performed high-level wave function theory calculations on bare FeO^{2+} and a series of non-heme Fe(IV)-oxo model complexes in order to elucidate the electronic properties and the ligand field effects on those channels. Our results suggest that a coordination environment formed by a weak field gives access to both competitive channels, yielding more reactive Fe(IV)-oxo sites. In contrast, a strong ligand environment stabilizes only the σ-channel. Our concluding remarks will aid the derivation of new structure–reactivity descriptors that can contribute to the development of the next generation of functional catalysts.

I. Introduction

The selective functionalization of the C–H bond has been regarded as a problem of major interest for energy and industrial applications.[1–4] This process is present in many biological processes and is promoted by enzymes that contain metal-oxo active sites. Nature has developed a large variety of heme and non-heme enzymes for the controlled oxidation of organic substrates.[5,6] Enzymes containing mononuclear and dinuclear iron sites activate dioxygen and form intermediate metal-oxo species, which promote the functionalization of strong C–H bonds.[6,7] For example, the non-heme enzymes α-ketoglutarate dependent taurine dioxygenase (TauD)[8,9] and syringomycin halogenase (SyrB2)[10,11] form high-valent Fe(IV)-oxo intermediates which can abstract a H-atom from an inert C–H bond as strong as 106 kcal mol^{-1} to initiate hydroxylation or halogenation.[12–15]

In an attempt to mimic nature and obtain new insights into the reactivity of the Fe(IV)-oxo unit, many non-heme Fe(IV)-oxo model complexes have been synthesized and characterized.[16–20] Alternatively, zeolites and metal–organic frameworks (MOFs) provide coordination environments suitable for the stabilization of highly reactive intermediates. Cationic Fe complexes stabilized in zeolite or MOF micropores have been shown to be efficient catalysts for the selective oxyfunctionalization of methane and ethane.[21–25] For these cases, a Fe(IV)-oxo intermediate has been suggested as the reactive intermediate.[23,24]

From an electronic structure standpoint, nature shows preference to a coordination environment for Fe(IV)-oxo which promotes the highly reactive high-spin quintet state ($S = 2$). Porous materials produce a weak ligand field on the deposited iron cations which stabilizes the high-spin intermediate as verified by magnetic circular dichroism (MCD) spectroscopy[23] and computational studies.[24,26,27] On the other hand, synthetic non-heme model complexes tend to prefer an intermediate spin state (triplet state; $S = 1$).[16,17,28] Several attempts have been made to synthesize stable high-spin models,[29–35] such as the tridentate TMG$_3$tren (TMG$_3$tren = 1,1,1-tris[2-[N2-(1,1,3,3-tetramethylguanidino)]ethyl]amine) Fe(IV)-oxo complex.[29]

Triplet spin complexes typically follow a two-state reactivity (TSR) scheme switching from triplet to quintet along the hydrogen abstraction step which lowers the activation barrier.[36] This spin–flip has been argued to have an energy penalty that lowers the reactivity of $S = 1$ complexes.[37] Alternatively, Meyer and co-workers applied a strong ligand field using a tetracarbene ligand maximizing the triplet–quintet gap.[38–41] This complex was found to be more reactive than other synthetic $S = 1$ non-heme model complexes and was attributed to the avoidance of the TSR scheme.

Aside from the spin issue, low catalytic reactivity of most of the model complexes is attributed to two other key reasons: the steric hindrance of the active sites and the self-oxidation

[a] *Department of Chemistry, University of Tennessee, Knoxville, Tennessee 37996, USA. E-mail: kvogiatz@utk.edu*

[b] *Department of Chemistry and Biochemistry, Auburn University, Auburn, Alabama 36849, USA. E-mail: emiliord@auburn.edu*

pathways that they undergo. MCD spectroscopy and multi-configurational wave function theory calculations have revealed two different reaction channels for the $[Fe^{IV}(O)(TMG_3tren)]^{2+}$ complex.[42] The first one activates a C–H bond of the substrate, and leads to the formation of the desired product, whereas the second one self-oxidizes the ligand and is responsible for the self-decay of the catalyst.

In total, four possible reaction channels are considered depending on the spin state of the Fe(IV)-oxo and the molecular orbital (MO) that overlaps with the activated C–H bond, which consequently leads to the abstraction of the hydrogen atom. Previous studies have described the electronic structure of ground and excited states of several Fe(IV)-oxo species.[39,40,42–46] These electronic states can be further related to different C–H activation mechanisms, and involve the evolution of Fe(IV)–O^{2-} (oxo) to Fe(III)–$O^{\bullet-}$ (oxyl), which occur upon elongation of the Fe–O bond.[47] The valence molecular orbitals (σ, π, δ, $\pi^\star$ and $\sigma^\star$) of the Fe–O unit are shown in Fig. 1 denoted by σ, π, $\delta(d_{x^2-y^2}/d_{xy})$, $\pi^\star$, and $\sigma^\star$. The first reaction channel involves the excitation of an electron from the σ bonding orbital (polarized towards oxygen) to the $\sigma^\star$ antibonding orbital (polarized towards iron). Therefore, upon the $\sigma \rightarrow \sigma^\star$ excitation, the $2p_z$ orbital of the oxygen atom becomes singly occupied, and O^{2-} evolves the radical $O^{\bullet-}$ (oxyl) character. The hydrogen atom abstraction via the $2p_z(\sigma)$ orbital is termed σ-mechanism and it is accessed from the ground state of the Fe(IV)-oxo intermediate. The first, doubly degenerate excited state introduces a competitive mechanism where one of the degenerate $2p_{x/y}$ orbitals of the oxygen atom (polarized π orbital) becomes singly occupied and the oxo atom evolves a radical $O^{\bullet-}$ character. Since the $2p_{x/y}$ orbitals are involved in the $\pi/\pi^\star$ molecular orbitals, this C–H activation channel is termed π-mechanism. The σ- and π-channels can further be divided to triplet $^3\sigma$ and $^3\pi$ and quintet $^5\sigma$ and $^5\pi$, depending on the spin state of the Fe(VI)–oxo unit. Fig. 2 presents all four mechanisms with MO diagrams, which suggest that the $^5\sigma/^5\pi$ mechanisms should be favored under a near-trigonal pyramidal field, whereas $^3\sigma/^3\pi$ mechanisms are more likely for near-octahedral structures.

Overall the followed mechanism is determined by the combination of specific electronic and stereochemical conditions. For example, the $S = 1$ species undergoing a TSR mechanism prefer the $^5\sigma$ channel,[48] while the high reactivity of the $S = 1$ tetracarbene complex is because of the accessibility to both

$^3\sigma$ and $^3\pi$ channels (about 4 kcal mol^{-1} difference).[40] The high-spin ($S = 2$) trigonal bipyramidal $[Fe^{IV}(O)(TMG_3tren)]^{2+}$ complex also has multiple available channels ($^5\sigma$, $^5\pi$ and $^3\pi$) but shows reactivity comparable to $S = 1$ complexes undergoing a TSR mechanism.[29] The reason is that unlike $^5\sigma$, the $^5\pi$ and $^3\pi$ channels cause the self-oxidation of the complex due to preferential overlap of the $2p_{x/y}$ orbitals of oxygen with the methyl groups of the ligands.[42,49] It is noteworthy that the non-heme enzyme SyrB2 modulates its reactivity by different channels; hydroxylation proceeds via $^5\sigma$, while halogenation via $^5\pi$.[11,43] Finally, the stereochemistry of the active site and the reactants promotes both $^5\pi$ and $^5\sigma$ mechanisms for the C–H activation of 4-hydroxymandelate synthase (HmaS) and (4-hydroxyphenyl)-pyruvate dioxygenase (HPPD), and AlkB enzymes.[50,51]

Presently, we aim to systematically analyze the electronic factors favoring the different reaction channels facilitated by the Fe(IV)-oxo sites. Our target is to elucidate at the electronic structure level how the ligand field increases or decreases the accessibility of each reactive channel. To this end, we performed multiconfigurational quantum chemical calculations for the ground and low-lying electronic states of model $[FeO]^{2+}$ systems. We started by constructing potential energy profiles for bare $[FeO]^{2+}$ followed by the singly coordinated $[(H_3N)FeO]^{2+}$ and $[(H_2O)FeO]^{2+}$ species before the study of the larger penta- and hexa-coordinated complexes composed of ammonia and water ligands in different ratios. We found that strong field ligands enable only the $^5\sigma$ mechanism, while weak ligands expedite additional channels.

The computational methodology followed in this study is described in Section II. In Section III, the low-lying energy states of bare and mono-coordinated $[FeO]^{2+}$ are discussed in detail. Section IV focuses on the ligand field effects on the reactive lowest lying electronic states. The electronic structure of each state is analyzed and correlated to the different reaction channels. Finally, in Section V, we summarize our findings and make suggestions for designing new ligands that can increase the accessibility of specific reaction channels or for descriptors.

II. Computational methodology

To ensure the accurate description of the $S = 1$ and $S = 2$ radical nature, we employed various multiconfigurational wave function approaches. The complete active space self-consistent field (CASSCF)[52,53] method was used to obtain the reference wave function. The notation CAS(n,m) stands for n electrons allocated in m active orbitals. Dynamical correlation was added by means of internally contracted multireference configuration interaction (MRCI)[54,55] or second-order perturbation theory (CASPT2).[56]

For diatomic $[FeO]^{2+}$, all possible single and double excitations of all valence electrons to the virtual space were variationally coupled through the internally contracted MRCI scheme implemented in MOLPRO.[57] The reference CASSCF wave function was built by allocating the 4s3d/Fe 2p/O electrons in 14 orbitals which at infinite Fe–O separation correspond to the 4s3d/Fe 2p/O orbitals plus an additional series of five d-orbitals on iron (CAS(10,14)).
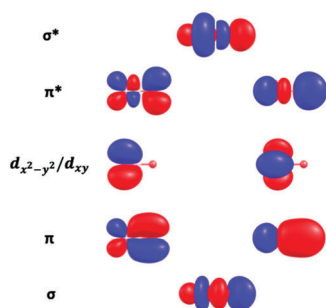

Fig. 1 Valence molecular orbitals of bare FeO^{2+} (R_{Fe-O} = 1.64 Å).
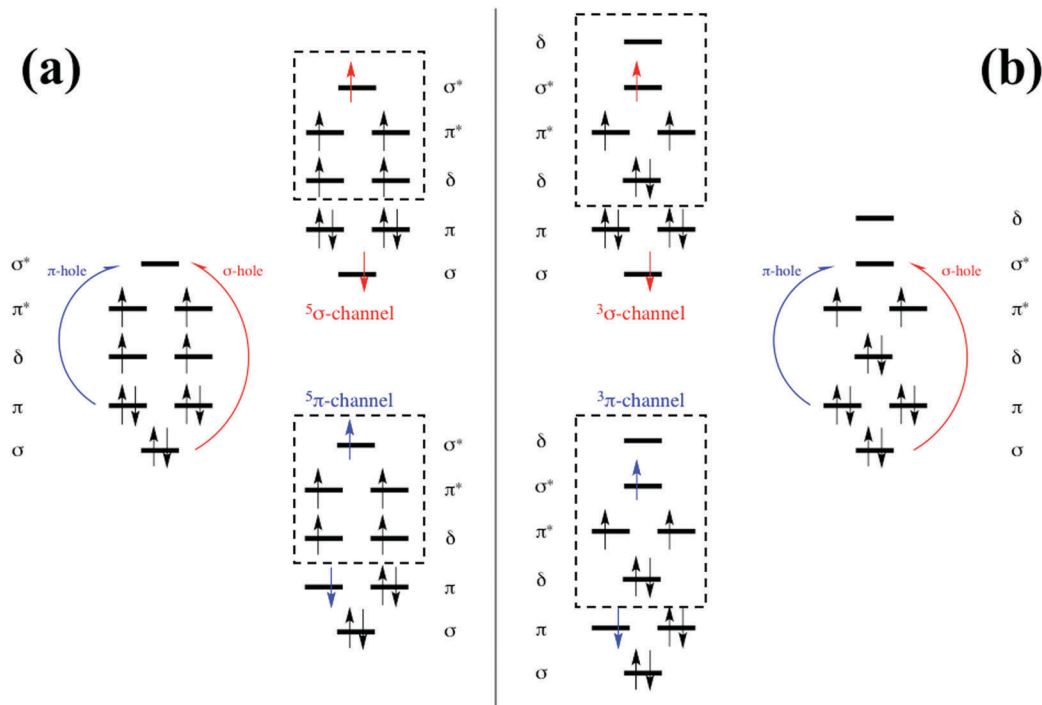
Fig. 2 Molecular orbital diagrams for (a) high-spin $S = 2$ Fe(IV)-oxo species in a near-trigonal pyramidal field and (b) intermediate-spin $S = 1$ Fe(IV)-oxo species in a near-tetragonal pyramidal field. Curved arrows show the electron transferred upon Fe−O bond elongation for the formation of the Fe(III)-oxyl species that promote the hydrogen atom abstraction via (a) the $^5\sigma$ and $^5\pi$ channels and (b) the $^3\sigma$ and $^3\pi$ channels. Orbitals inside the dashed-line boxes have predominant iron character.

The latter orbitals were deemed technically necessary for the correct dissociation of the potential energy curves (PECs). The cc-pVQZ/Fe aug-cc-pVQZ/O basis sets were used to construct the CASSCF orbitals. State-averaged calculations were performed with all states having equal weights.

The calculations for the singly coordinated $[(H_3N)FeO]^{2+}$ and $[(H_2O)FeO]^{2+}$ complexes were done in the equilibrium region using only the 4s3d/Fe 2p/O orbitals in the reference CASSCF wave function (CAS(10,9)), but still allowing excitations from all valence orbitals at MRCI.

Larger active spaces have to be considered for the larger complexes. For the near-C_{4v} hexa-coordinated and near-C_{3v} penta-coordinated iron complexes, one and two bonding ligand-Fe($3d_{x^2−y^2}$) and ligand-Fe($3d_{xy}/3d_{x^2−y^2}$) MOs were added, respectively (the term near is used since consideration of hydrogen atoms of the ligands lowers the symmetry of the tetragonal pyramidal and trigonal pyramidal, respectively). In the latter case, the displacement of 2s of oxygen by a ligand orbital was observed at specific Fe–O bond distances. This orbital rotation did not affect the quintet states, but introduced inconsistencies for triplets. The second d-shell of Fe was found to affect the relative energy differences by less than 0.1 eV (see the ESI,† Section S1) and it was excluded. The total size of the active space is CAS(20,13) and CAS(18,12) for penta- and hexacoordinated Fe complexes, respectively. State-averaged restricted active space SCF (SA-RASSCF)[52,58] calculations were performed for the examination of larger active spaces that included the 3s of Fe, the 2s of O, and lone pair of NH_3, as is discussed in the ESI,†

Sections S1 and S2. For quantitative results, the multi-state extension of CASSCF and RASSCF that include dynamic correlation from second-order perturbation theory (CASPT2[56] and RASPT2,[59] respectively) was used.

All SA-RASSCF/MS-RASPT2 calculations were performed with the MOLCAS 8.2 program package.[60] Scalar relativistic effects were included using the all-electron triple-zeta quality atomic natural orbital relativistic basis sets (ANO-RCC-VTZP)[61,62] and a second-order Douglas–Kroll–Hess Hamiltonian.[63,64] A shifted zeroth-order Hamiltonian[65] (IPEA shift) with the default value of 0.25 a.u. and an imaginary shift[66] of 0.2 a.u. were applied to all MS-RASPT2 calculations. The two-electron integral evaluation was simplified by using the Cholesky decomposition.[67]

III. Bare and mono-coordinated $[FeO]^{2+}$

We start our discussion with the bare and mono-coordinated $[FeO]^{2+}$ species since they provide valuable insights which aid the investigation of the larger systems. It should be mentioned that the electronic structures of the bare FeO and $[FeO]^+$ have been examined previously in great detail,[68,69] but to the best of our knowledge, bare $[FeO]^{2+}$ has not been studied before.

The first two ionization energies of iron are 7.90 eV [Fe(^{5}D) → Fe$^+$(^{6}D)] and 16.19 eV [Fe$^+$(^{6}D) → Fe^{2+}(^{5}D)],[70] while for oxygen they are 13.62 eV [O(^{3}P) → O$^+$(^{4}S)] and 35.12 eV [O$^+$(^{4}S) → O^{2+}(^{3}P)].[70] These values set the lowest dissociation

channel as $Fe^+(^6D) + O^+(^4S)$ followed by $Fe^{2+}(^5D;d^6) + O(^3P)$ at 2.57 eV. This energy range fits eight excited electronic states of Fe^+,[71] but none for O^+. All $Fe^+ + O^+(^4S;2s^22p^3)$ asymptotes generate dissociative PECs, and considering a $1/R(Fe–O)$ repulsion, the $Fe^+ + O^+$ energies increase by as much as 1.44 eV at 10 Å. At the same distance, the $Fe^{2+} + O$ fragments interact only weakly. Thus, the $Fe^+(^6D) + O^+(^4S)$ and $Fe^{2+}(^5D;d^6) + O(^3P)$ asymptotes approach to $2.57 - 1.44 = 1.13$ eV, which means that only three $Fe^+ + O^+$ channels are lower than $Fe^{2+} + O$ at 10 Å. All states (32 triplets, quintets, and septets) of these four channels are included in our PECs of Fig. 3–5, which cover Fe–O distances shorter than 8 Å. Further implying this simple model, the $Fe^+(^6D) + O^+(^4S)$ and $Fe^{2+}(^5D;d^6) + O(^3P)$ asymptotes are expected to cross at $1/R(Fe–O) = 2.57$ eV which yields $R(Fe–O) = 5.6$ Å. Indeed our PECs present an avoided crossing region at 5.5–6 Å. Setting the zero of the energy scale equal to that of $Fe^{2+}(^5D) + O(^3P)$, the lowest energy fragments $Fe^+(^6D) + O^+(^4S)$ are at -2.57 eV $= -59.3$ kcal mol^{-1}. In the same scale, the equilibrium energy of the ground $^3\Delta$ state is -42 kcal mol^{-1} (see Fig. 3) and -10 kcal mol^{-1} for our highest state ($^3\Pi$). Therefore, all equilibrium energies are lower than the $Fe^{2+} + O$ fragments but higher than the $Fe^+ + O^+$ ones, which means that bare FeO^{2+} is thermodynamically unstable, but kinetically stable because of the large dissociation barriers.

The first three dissociation paths associate with the $^6D(4s^13d^6)$, $^4F(3d^7)$, and $^4D(4s^13d^6)$ states of Fe^+ which combined with $O^+(^4S)$ create a series of singlets, triplets, quintets, and septets with Σ^+, Σ^-, Π, Δ, and Φ symmetries. The $Fe^{2+}(^5D) + O(^3P)$ channel generates (Wigner–Witmer rules) the $^{3,5,7}[\Sigma^+, \Sigma^-(2), \Pi(3), \Delta(2), \Phi]$ states. The states of the same spin and space symmetry from the different channels run into each other producing the avoided crossings of Fig. 3–5.

All minima at Fe–O distances of 2–2.5 Å come smoothly from $Fe^{2+}(^5D) + O(^3P)$ and their equilibrium electronic structure is closer to the Fe(III)-oxyl picture. For example, $^5\Delta$ at its equilibrium bond length of 2.15 Å is (see the ESI†) $|^5\Delta\rangle \approx 0.72|\sigma^2\pi^2\pi\star^2\delta^3\sigma^1\rangle$. However, there are PECs which exhibit additional features. Specifically, the $^5\Sigma^+$ state of Fig. 4 follows its sister states for

Fig. 4 Potential energy curves of the quintet electronic states of FeO^{2+}.
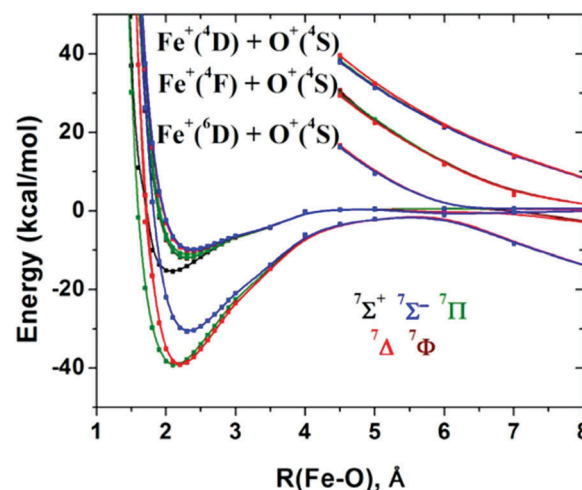
Fig. 5 Potential energy curves of the septet electronic states of FeO^{2+}.

Fig. 3 Potential energy curves of the triplet electronic states of FeO^{2+}.

distances longer than 2.5 Å tending to form a minimum at 2.2 Å. It deviates though creating a minimum at 1.64 Å. Similar minima are found for $^3\Phi$ and $^3\Sigma^+$ which undergo an avoided crossing right at the region of their 1.6 Å minima with PEC of lower states (see the encircled region of Fig. 3). Finally, $^5\Pi$ reveals a shoulder at the same distance (see Fig. 4), which turns out to create gradually a clear minimum in the presence of ligands (see below). The electronic configurations and spectroscopic constants for all of the bound states are given in the ESI,† Section S3.

To locate the origin of these additional features, we focused on the CI vectors at 1.6 Å of the relative states. The dominant electronic configurations of $^5\Sigma^+$ (equilibrium) and $^5\Pi$ (shoulder), are (see Fig. 1 for orbital notation):

$$|^5\Sigma^+\rangle \approx 0.74|\sigma^2\pi^4\pi\star^2\delta^2\rangle$$

$$|^5\Pi\rangle \approx 0.78|\sigma^2\pi^4\pi\star^1\delta^2\sigma\star^1\rangle$$

These are the only quintets with $\sigma^2\pi^4$, and as discussed in the introduction, the polarization of σ and π towards oxygen signals

an *in situ* Fe(IV)-oxo picture. All quintets with equilibrium bond lengths of about 2–2.5 Å are of $\sigma^1\pi^4$ or $\sigma^2\pi^3$ character matching better to a radical terminal oxygen, Fe(III)-oxyl. The same configurations prevail for $^5\Sigma^+$ and $^5\Pi$ for R(Fe–O) > 2.0 Å. Specifically, their configurations at 2.7 Å ($^5\Sigma^+$) and 2.14 Å ($^5\Pi$) are:

$$|^5\Sigma^+\rangle \approx 0.80|\sigma^1\pi^4\pi^{\star2}\delta^2\sigma^{\star1}\rangle$$

$$|^5\Pi\rangle \approx 0.72|\sigma^2\pi^3\pi^{\star2}\delta^2\sigma^{\star1}\rangle$$

Because of their larger iron formal charge, the approach of a ligand is expected to stabilize the equilibrium of $^5\Sigma^+$ and the shoulder of $^5\Pi$ over the rest quintets.

To corroborate these observations, we added an ammonia or water ligand to the $[FeO]^{2+}$ diatomic and constructed the PECs in the Fe–O equilibrium region for the lowest quintet states ($^5\Sigma^+$, $^5\Pi$ and $^5\Delta$). The $[FeO(H_2O)]^{2+}$ and $[FeO(H_3N)]^{2+}$ structures were fully optimized at the MRCI level for the $^5\Sigma^+$ and then scanned over the Fe–O distance by keeping all other geometrical parameters fixed. The potential energy curves are shown in Fig. 6.

In comparison to bare $[FeO]^{2+}$, the $^5\Sigma^+$ minimum (black line) is stabilized with the addition of a water molecule (weak ligand field), and even more so with an ammonia molecule (strong ligand field). The same is true for the shoulder of $^5\Pi$ which splits into two components due to symmetry lowering. In the case of ammonia, one of the $^5\Pi$ components becomes a very shallow local minimum. It is these minima that stabilize further upon the addition of more ligands generating the ^5A and ^5E states (see Section IV). Overall, the $^5\Sigma^+$ and $^5\Pi$ states have a Fe(IV)-oxo character at R(Fe–O) ∼ 1.6 Å which switches to Fe(III)-oxyl at R(Fe–O) ∼ 2.25 Å. This transition occurs at about 1.8 Å (energy barrier of the two rightmost plots of Fig. 6). Additionally, the Fe(IV)-oxo region is stabilized over the Fe(III)-oxyl region when adding a ligand, and this stabilization is larger for ammonia than water.

These observations generally apply to the corresponding ^5A and ^5E states of the fully coordinated systems examined in Section IV, where more accurate and quantitative results are reported. To assure that CASPT2, which was used for the larger complexes, and MRCI are equivalent, we repeated the above analysis for the diatomic $[FeO]^{2+}$ species at the SA(3)-CASSCF/MS(3)-CASPT2 level; MRCI and CASPT2 are in agreement with each other.

IV. Ligand field effects

The effect of different ligand fields on the stability of the larger fully-coordinated Fe(IV)-oxo species and its evolution to the reactive Fe(III)-oxyl are discussed in this section. The six different model complexes used in this study are the $[Fe(O)(H_2O)_4]^{2+}$, $[Fe(O)(H_2O)_5]^{2+}$, $[Fe(O)(H_2O)_{ax}(NH_3)_3]^{2+}$, $[Fe(O)(H_2O)_{ax}(NH_3)_4]^{2+}$, $[Fe(O)(NH_3)_4]^{2+}$, and $[Fe(O)(NH_3)_5]^{2+}$ (Fig. 7). The H_2O ligands are considered representative of a weak ligand field, while the NH_3 ligands representative of a strong ligand field. Two out of these six models ($[Fe(O)(H_2O)_5]^{2+}$ and $[Fe(O)(H_2O)_{ax}(NH_3)_4]^{2+}$) have been employed by Kazaryan and Baerends,[72] who examined using density functional theory (DFT) the ligand field effects on the spin state and the C–H activation promoted by the Fe(IV)-oxo moiety. The Fe atom in the $[Fe(O)(H_2O)_5]^{2+}$ model experiences a weak field and has a $S = 2$ ground spin state. In contrast, the $[Fe(O)(H_2O)_{ax}(NH_3)_4]^{2+}$ model has a $S = 1$ ground state, since the NH_3 ligands form a stronger field. The $[Fe(O)(H_2O)_{ax}(NH_3)_4]^{2+}$ model is also representative of the two-state reactivity scheme for the C–H activation mechanism, since a spin-transition occurs at the corresponding transition state.[36] However, CASPT2 calculations on the DFT optimized geometries predicted for both systems a high-spin $S = 2$ ground spin state. For obtaining optimized geometries with the correct ground state for all six model complexes, we have performed symmetric Fe–L scans (L = equatorial H_2O or NH_3). For the models with strong ligand fields, the addition of the lone pair of NH_3 and the 3s3p of Fe was mandatory.[73,74] The MS-RASPT2 calculations provided the correct global ground spin state ($S = 1$) for the pseudo-C_{4v} species ($[Fe(O)(H_2O)_{ax}(NH_3)_4]^{2+}$), as expected, with a Fe–L distance of 2.000 Å. Similarly, the expected high-spin ($S = 2$) was obtained for the remaining pseudo-C_{3v} models ($[Fe(O)(H_2O)_{ax}(NH_3)_3]^{2+}$ and $[Fe(O)(NH_3)_4]^{2+}$), as is explained in the introduction. Figures with the six potential energy scans along the Fe–L distances are given in the ESI,† Section S1.
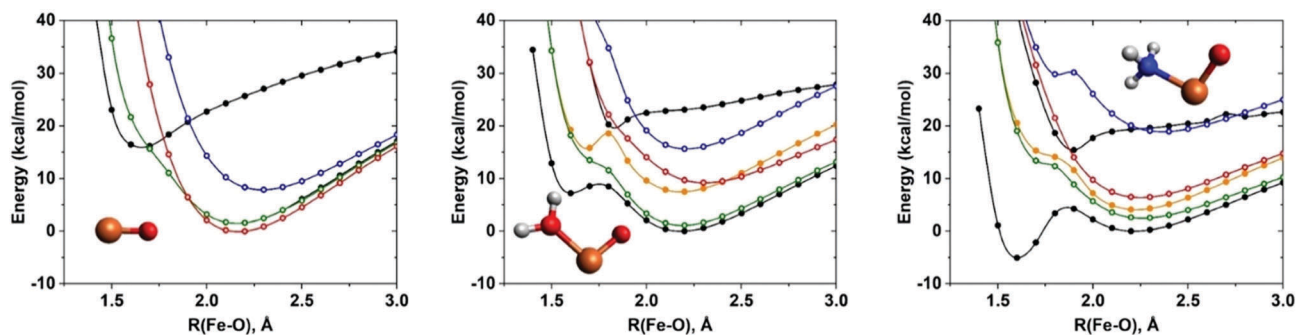
Fig. 6 CASSCF(12,9)/MRCI PECs for $[FeO]^{2+}$, $[(H_2O)FeO]^{2+}$, and $[(H_3N)FeO]^{2+}$ using the cc-pVTZ (Fe,NH$_3$,H$_2$O) aug-cc-pVQZ (terminal O) basis set. The color coding for bare FeO^{2+} is the same as in Fig. 4. For the mono-coordinated complexes, solid circles correspond to $^5A''$ and open circles to $^5A'$ states.
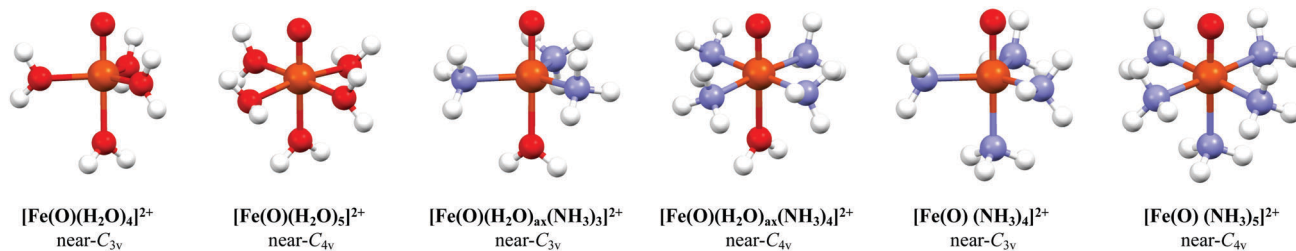
Fig. 7 The six model complexes used in this work, their chemical formulae and their pseudo-symmetry point groups. The Fe-equatorial ligand distances have been optimized with symmetric scans at the CASSCF/RASSCF level. (Fe: light brown, O: red, N: blue and H: white).

Once the equatorial Fe–L distances were calibrated for the six models, potential energy curves along the Fe–O bond distance were calculated. A detailed analysis of one representative species ($[Fe(O)(H_2O)_5]^{2+}$) is given, but similar considerations hold for the remaining five models (ESI,† Section S4). The left plot of Fig. 8 shows the potential energy curves for the ground (^5A, orange) and the doubly degenerate first excited states (^5E, black) calculated at the MS-RASPT2(24,15) level of theory. A detailed analysis of the CI coefficients obtained from the multiconfigurational zeroth-order SA-CASSCF(18,12) wave function reveals the character of the two electronic states. As is explained in Section I and shown in Fig. 2, the non-reactive Fe(IV)-oxo configuration involves a $3d^4$ Fe atom and a closed-shell $2p^6$ O atom. By adding the weights (i.e. the square of the CI coefficients) of each configuration that corresponds to such electronic configurations, we can calculate the Fe(IV)-oxo character of each state. Similarly, the reactive Fe(III)-oxyl character can be calculated as the sum of all configurations that involve the transfer of an electron from O to Fe.

This electron transfer reduces Fe(IV) to Fe(III) and creates a hole in the electronic configuration of the O atom, which results in the radical character of the oxyl species. At the equilibrium bond distance (around 1.58 Å), both states have a non-reactive character, with a 0.73/0.14 ratio between Fe(IV)-oxo/Fe(III)-oxyl for the ground state ^5A and a 0.54/0.30 ratio for the first excited state ^5E, as is shown in the right plot of Fig. 8. The character of the two states changes upon Fe–O bond elongation. It is evident from the same plot of Fig. 8 that at

1.67 Å, the reactive Fe(III)-oxyl becomes the dominant character of the first excited state. This means that the π-channel becomes accessible at bond distances of 1.67 Å or higher. However, the excited state is still less stable than the ^5A state by about 1 eV (Fig. 8 left). The ^5A ground state obtains a radical character at about 1.84 Å, and the σ-channel becomes accessible. The intercrossing of the two states occurs at about 1.86 Å and thus, both reactive channels are accessible for C–H abstraction. The Fe–O bond distance at the transition state of the C–H activation is expected to fall between 1.67 Å and 1.86 Å. Indeed, previous mechanistic DFT studies for a fully hydrated FeO^{2+} species predicted a Fe–O distance at a transition state of 1.728 Å[72], while for the fully oxygen coordination sphere of a Fe-containing MOF-74 catalyst, a value of 1.75 Å was calculated.[26]

The triplet states for the $[Fe(O)(H_2O)_5]^{2+}$ model complex were calculated at the same level of theory (MS-CASPT2(18,12), see the ESI,† Section S4). The relative energy of the six lowest states from the ^5A ground state is more than 1.73 eV at the equilibrium geometry, where they exhibit a shallow minimum in their potential energy curves. Similarly to the quintet counterparts, they have a non-reactive Fe(IV)-oxo character that evolves into radical Fe(III)-oxyl at longer Fe–O bond distances. Their energies at the $R_{Fe–O} = 1.7–1.9$ Å range are between 1.0 and 1.3 eV, comparable to the quintet states (Fig. 8, left). This leads to the conclusion that the triplet channels are also accessible for C–H activation, in addition to the quintet σ- and π-channels. We were not able to distinguish between the ^{3}σ- and ^{3}π-channels since
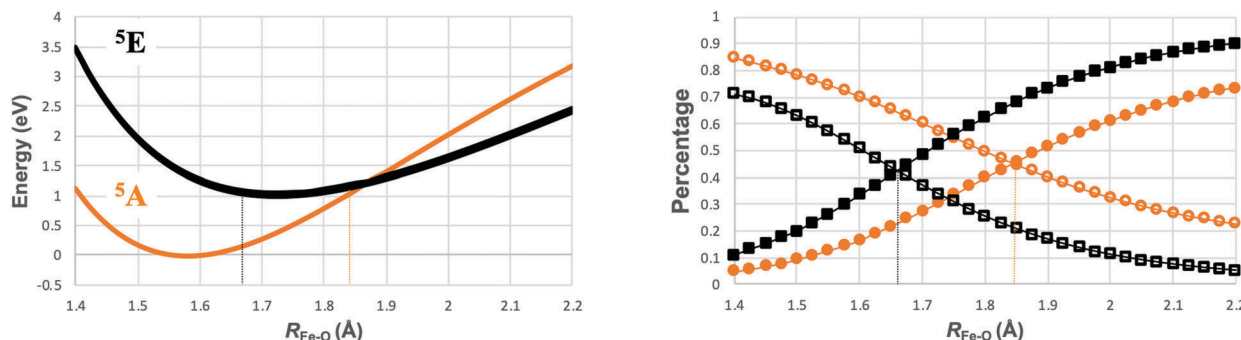
Fig. 8 Left: Potential energy curves of $[Fe(O)(H_2O)_5]^{2+}$ at the MS-CASPT2(18,12) level for the ground (^5A, orange) and first excited states (^5E, black) along the Fe−O bond distance. Right: The percentage of the wave function for the ground (^5A, orange) and first excited states (^5E, black) along the Fe−O bond distance which corresponds to the non-reactive Fe(IV)-oxo electronic configuration (open circles and squares, respectively) and to the radical Fe(III)-oxyl configuration (closed circles and squares, respectively). The vertical orange and black dotted lines on both figures indicate the Fe−O distance where the character of the electronic states changes from the non-reactive Fe(IV)-oxo to the radical Fe(III)-oxyl.

Table 1 Energy difference ΔE (eV) of the ^{5}E and lowest triplet states (^{3}A/^{3}E) with respect to the most stable quintet state (^{5}A) at R_{Fe-O} = 1.60 Å, Fe–O distance R_C (Å) where ^{5}A and ^{5}E states cross, and $R_{C,Q/T}$ (Å) where quintet and triplet states cross

Model complex	$\Delta E(^5E)$	$\Delta E(^3A/^3E)$	R_C	$R_{C,Q/T}$
$[Fe(O)(H_2O)_4]^{2+}$	1.31	1.73	1.91	1.92
$[Fe(O)(H_2O)_5]^{2+}$	1.24	1.42	1.86	1.97
$[Fe(O)(H_2O)_{ax}(NH_3)_3]^{2+}$	1.56	1.69	1.97	1.92
$[Fe(O)(H_2O)_{ax}(NH_3)_4]^{2+}$	1.65	−0.46	1.98	2.10
$[Fe(O)(NH_3)_4]^{2+}$	1.79	2.26	2.03	1.94
$[Fe(O)(NH_3)_5]^{2+}$	1.92	−0.47	2.03	2.10

electronic configurations corresponding to these channels were present in all low-lying triplet states. Exception was the $[Fe(O)(H_2O)_{ax}(NH_3)_4]^{2+}$ species, as is discussed in the next paragraphs.

The results from all six model complexes are summarized in Table 1. The first observation is related to the relative energy differences of the quintet ground and excited states (also shown in Fig. 9). For the two hydrated models (four and five water molecules in the coordination sphere of Fe), the relative energy differences of the two states at 1.60 Å are 1.31 and 1.24 eV, respectively. The same energy difference increases once the equatorial water molecules are substituted by stronger ligands (NH$_3$), while for the all-ammonia complex ($[Fe(O)(NH_3)_4]^{2+}$), the $\Delta E(^5A-^5E)$ at 1.60 Å is 1.79 eV. Similarly, the intercrossing of the two quintet states occurs at longer Fe–O bond distances once the strength of the ligand field increases (from 1.86 to 2.03 Å). Therefore, we conclude that the increase of the ligand field strength destabilizes the π-channel (Fig. 9) and makes it less accessible for C–H activation. This conclusion is in agreement with the observation made by Kupper et al.[40] on the reactivity of the $[Fe(O)(TMC)(MeCN)]^{2+}$ biomimetic model complex that shares the same coordination environment with the $[Fe(O)(H_2O)_{ax}(NH_3)_4]^{2+}$ complex from our study. In the previous study, a combination of DFT with multiconfigurational calculations revealed that the specific non-heme model complex has only one accessible reaction mechanism ($^5σ$).

From the six model complexes discussed, the $[Fe(O)(H_2O)_{ax}(NH_3)_4]^{2+}$ and $[Fe(O)(NH_3)_5]^{2+}$ have a triplet ground state (Table 1).
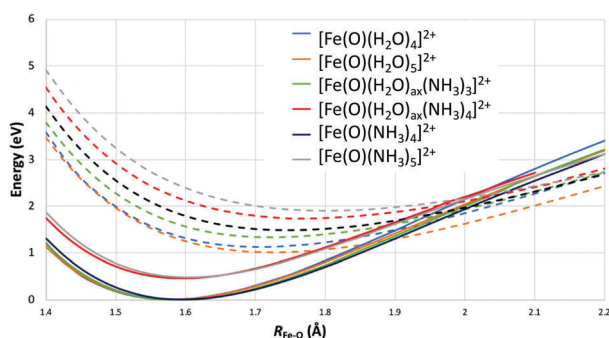
Fig. 9 Superimposed potential energy curves of the six Fe-oxo models considered in this study. Solid lines correspond to the ground quintet state (^{5}A) that evolves to the $^5σ$ channel, dashed lines to the first excited state (^{5}E) that evolves to the $^5π$ channel.

However, the specific complex follows a two-state reactivity mechanism,[72] so the quintet states are mostly relevant to C–H activation. For examining the accessibility of the $^3σ$ and $^3π$ channels, we have analyzed the character of the triplet states and how those evolve to Fe(III)-oxyl with hole on the σ and π bonding orbitals, respectively. For all species, six low-lying triplet states were found, which are within less than 1.0 eV for the Fe–O bond range of 1.6–1.9 Å. The only exceptions are $[Fe(O)(H_2O)_{ax}(NH_3)_4]^{2+}$ and $[Fe(O)(NH_3)_5]^{2+}$, which due to the Jahn–Teller effect (Fig. 2(b)), have a non-degenerate triplet ground state, with the next three triplet states being more than 1.39 eV less stable (at 1.60 Å).

Finally, for all the models considered in this study, the ground state (quintet) crosses the triplet states at bond distances that all channels are accessible (1.92–1.97 Å, Table 1). Exceptions are the two species with inverted spin state order (intercrossing at 2.10 Å), but since they follow the two-state reactivity scheme, the quintet states are more relevant for comparison.

V. Conclusions and outlook

In this work, we have performed an in-depth study on the electronic structure of the low-lying states of a bare $[FeO]^{2+}$ species and a series of six Fe(IV)-oxo model complexes, by applying multiconfigurational wave function theory. Our calculations revealed the electronic effects of the strength of the ligand field on the most stable quintet and triplet states, and were correlated to the reaction channels of the evolving Fe(III)-oxyl radical species for C–H activation. The results presented here suggest that engineering of the primary coordination sphere can tune the accessibility of the different C–H reaction channels of the Fe(IV)-oxo biomimetic sites and affect their reactivity.

The electronic structure of the bare iron oxide dication was elucidated via the construction of full PECs and the analysis of the equilibrium configurations at highly correlated multi-reference techniques (CASSCF and MRCI). We found potential energy minima in two different Fe–O regions. At longer distances (2–2.5 Å) an iron-oxyl (radical oxygen terminal) character prevails while at shorter distances the iron–oxo (closed-shell oxygen terminal) character emerges. It is the $^5Σ^+$ and $^5Π$ states which evolve to ^{5}A and ^{5}E species upon coordination, which exhibit an Fe(III)–O$^{•-}$ and Fe(IV)–O^{2-} identity at longer and shorter Fe–O distances, respectively. For all states we report accurate energetics and spectroscopic parameters. Despite its metastable nature, bare $[FeO]^{2+}$ is separated from the Fe$^+$ + O$^+$ fragments by large activation barriers enabling its experimental observation.

Once the electronic structure of the bare FeO^{2+} was elucidated, we examined the ligand field effects on the low-lying states. At the equilibrium geometry, the $[FeOL_n]^{2+}$ species (L = H$_2$O and/or NH$_3$, n = 4 or 5) have a non-reactive Fe(IV)-oxo character that evolves into a Fe(III)-oxyl radical once at larger Fe–O bond distances. The radical character is a consequence of an electron promotion from the bonding σ or π orbitals to the antibonding ones. Since the bonding orbitals are polarized towards the

28792 | Phys. Chem. Chem. Phys., 2018, **20**, 28786–28795

This journal is © the Owner Societies 2018

oxygen atom, the electron transfer is responsible for the formation of a hole on the 2p atomic orbitals of the oxygen, which evolves the radical character. This electron hole on oxygen can be found either on the σ- or π-type orbital, which are responsible for different C–H abstraction mechanisms, known as σ- and π-mechanisms, respectively. In this work, we quantified the accessibility of those reaction channels by considering different ligand field environments. We have considered the relative energy difference of the two states responsible for these two reaction channels, and the Fe–O bond distance that they intercross.

The Fe(ιν)-oxo sites that have multiple accessible reaction channels are considered more catalytically active than those that have only one channel for C–H activation. We showed that a weaker ligand environment lowers the energy difference between the reactive states of the Fe(ιν)-oxo species at the equilibrium geometry, which will evolve into Fe(ιιι)-oxyl with a strong radical character, and eventually increases their reactivity. Conclusions from the multiconfigurational calculations presented in this work are in agreement with recent literature and support the known structure–function relation between the ligand field strength and catalytic performance for C–H activation.[16,75] For example, Mukherjee et al. have reported a 10^4-fold increase of oxidation reaction rates when weaker ligands are introduced in the equatorial position in a Fe(ιν)-oxo complex.[76] Another example is the recent experimental work of Rasheed et al., who observed increased reactivity at weaker ligand fields by increasing the equilibrium metal–ligand distance (using bulkier ligands).[77] We believe that in the future, the relative energies of the ground (σ-mechanism) and first excited states (π-mechanism) can be used as a descriptor of catalytic activity of the Fe(ιν)-oxo species.

Conflicts of interest

There are no conflicts to declare.

Acknowledgements

References

1 H. Schwarz, Angew. Chem., Int. Ed., 2011, **50**, 10096.

2 F. Roudesly, J. Oble and G. Poli, J. Mol. Catal. A: Chem., 2017, **426**, 275.

3 H. Schwarz, S. Shaik and J. Li, J. Am. Chem. Soc., 2017, **139**, 17201.

4 H. Schwarz, P. González-Navarrete, J. Li, M. Schlangen, X. Sun, T. Weiske and S. Zhou, Organometallics, 2016, **36**, 8.

5 T. L. Poulos, Chem. Rev., 2014, **114**, 3919.

6 K. Ray, F. F. Pfaff, B. Wang and W. Nam, J. Am. Chem. Soc., 2014, **136**, 13942.

7 S. Sahu and D. P. Goldberg, J. Am. Chem. Soc., 2016, **138**, 11410.

8 J. M. Elkins, M. J. Ryle, L. J. Clifton, J. C. D. Hotopp, J. S. Lloyd, N. I. Burzlaff, J. E. Baldwin, R. P. Hausinger and P. L. Roach, Biochemistry, 2002, **41**, 5185.

9 J. C. Price, E. W. Barr, T. E. Glass, C. Krebs and J. M. Bollinger Jr., J. Am. Chem. Soc., 2003, **125**, 13008.

10 M. L. Matthews, C. S. Neumann, L. A. Miles, T. L. Grove, S. J. Booker, C. Krebs, C. T. Walsh and J. M. Bollinger Jr, Proc. Natl. Acad. Sci. U. S. A., 2009, **106**, 17723.

11 S. D. Wong, M. Srnec, M. L. Matthews, L. V. Liu, Y. Kwak, K. Park, C. B. Bell III, E. E. Alp, J. Zhao, Y. Yoda, S. Kitao, M. Seto, C. Krebs, J. M. Bollinger and E. I. Solomon, Nature, 2013, **499**, 320.

12 C. Krebs, D. G. Fujimori, C. T. Walsh and J. M. Bollinger Jr., Acc. Chem. Res., 2007, **40**, 484.

13 B. E. Eser, E. W. Barr, P. A. Frantom, L. Saleh, J. M. Bollinger Jr., C. Krebs and P. F. Fitzpatrick, J. Am. Chem. Soc., 2007, **129**, 11334.

14 D. G. Fujimori, E. W. Barr, M. L. Matthews, G. M. Koch, J. R. Yonce, C. T. Walsh, J. M. Bollinger Jr., C. Krebs and P. J. Riggs-Gelasco, J. Am. Chem. Soc., 2007, **129**, 13408.

15 M. L. Matthews, C. M. Krest, E. W. Barr, F. H. Vaillancourt, C. T. Walsh, M. T. Green, C. Krebs and J. M. Bollinger Jr., Biochemistry, 2009, **48**, 4331.

16 W. Nam, Acc. Chem. Res., 2007, **40**, 522.

17 L. Que Jr., Acc. Chem. Res., 2007, **40**, 493.

18 W. N. Oloo and L. Que, Acc. Chem. Res., 2015, **48**, 2612.

19 M. Puri and L. Que, Acc. Chem. Res., 2015, **48**, 2443.

20 W. Nam, Acc. Chem. Res., 2015, **48**, 2415.

21 V. I. Sobolev, K. A. Dubkov, O. V. Panna and G. I. Panov, Catal. Today, 1995, **24**, 251.

22 K. A. Dubkov, V. I. Sobolev, E. P. Talsi, M. A. Rodkin, N. H. Watkins, A. A. Shteinman and G. I. Panov, J. Mol. Catal. A: Chem., 1997, **123**, 155.

23 B. E. R. Snyder, P. Vanelderen, M. L. Bols, S. D. Hallaert, L. H. Böttger, L. Ungur, K. Pierloot, R. A. Schoonheydt, B. F. Sels and E. I. Solomon, Nature, 2016, **536**, 317.

24 D. J. Xiao, E. D. Bloch, J. A. Mason, W. L. Queen, M. R. Hudson, N. Planas, J. Borycz, A. L. Dzubak, P. Verma, K. Lee, F. Bonino, V. Crocellà, J. Yano, S. Bordiga, D. G. Truhlar, L. Gagliardi, C. M. Brown and J. R. Long, Nat. Chem., 2014, **6**, 590.

25 P. Liao, R. B. Getman and R. Q. Snurr, ACS Appl. Mater. Interfaces, 2017, **9**, 33484.

26 P. Verma, K. D. Vogiatzis, N. Planas, J. Borycz, D. J. Xiao, J. R. Long, L. Gagliardi and D. G. Truhlar, J. Am. Chem. Soc., 2015, **137**, 5770.

27 H. Hirao, W. K. H. Ng, A. M. P. Moeljadi and S. Bureekaew, ACS Catal., 2015, **5**, 3287.

28 X. Engelmann, I. Monte-Pérez and K. Ray, *Angew. Chem., Int. Ed.*, 2016, **55**, 7632.

29 J. England, M. Martinho, E. R. Farquhar, J. R. Frisch, E. L. Bominaar, E. Münck and L. Que, *Angew. Chem., Int. Ed.*, 2009, **48**, 3622.

30 D. C. Lacy, R. Gupta, K. L. Stone, J. Greaves, J. W. Ziller, M. P. Hendrich and A. S. Borovik, *J. Am. Chem. Soc.*, 2010, **132**, 12188.

31 J. P. Bigi, W. H. Harman, B. Lassalle-Kaiser, D. M. Robles, T. A. Stich, J. Yano, R. D. Britt and C. J. Chang, *J. Am. Chem. Soc.*, 2012, **134**, 1536.

32 J. England, Y. Guo, K. M. V. Heuvelen, M. A. Cranswick, G. T. Rohde, E. L. Bominaar, E. Münck and L. Que, *J. Am. Chem. Soc.*, 2011, **133**, 11880.

33 A. N. Biswas, M. Puri, K. K. Meier, W. N. Oloo, G. T. Rohde, E. L. Bominaar, E. Münck and L. Que Jr., *J. Am. Chem. Soc.*, 2015, **137**, 2428.

34 O. Pestovsky, S. Stoian, E. L. Bominaar, X. Shan, E. Münck, L. Que Jr. and A. Bakac, *Angew. Chem., Int. Ed.*, 2005, **44**, 6871.

35 M. B. Chambers, S. Groysman, D. Villagrán and D. G. Nocera, *Inorg. Chem.*, 2013, **52**, 3159.

36 D. Schröder, S. Shaik and H. Schwarz, *Acc. Chem. Res.*, 2000, **33**, 139.

37 S. Shaik, H. Chen and D. Janardanan, *Nat. Chem.*, 2011, **3**, 19.

38 S. Meyer, I. Klawitter, S. Demeshko, E. Bill and F. Meyer, *Angew. Chem., Int. Ed.*, 2013, **52**, 901.

39 S. Ye, C. Kupper, S. Meyer, E. Andris, R. Navrátil, O. Krahe, B. Mondal, M. Atanasov, E. Bill, J. Roithová, F. Meyer and F. Neese, *J. Am. Chem. Soc.*, 2016, **138**, 14312.

40 C. Kupper, B. Mondal, J. Serrano-Plana, I. Klawitter, F. Neese, M. Costas, S. Ye and F. Meyer, *J. Am. Chem. Soc.*, 2017, **139**, 8939.

41 R. Kumar, A. Ansari and G. Rajaraman, *Chem. – Eur. J.*, 2018, **24**, 6818.

42 M. Srnec, S. D. Wong, J. England, J. Lawrence Que and E. I. Solomon, *Proc. Natl. Acad. Sci. U. S. A.*, 2012, **109**, 14326.

43 M. Srnec, S. D. Wong, M. L. Matthews, C. Krebs, J. M. Bollinger Jr. and E. I. Solomon, *J. Am. Chem. Soc.*, 2016, **138**, 5110.

44 A. Decker, J.-U. Rohde, E. J. Klinker, S. D. Wong, J. Que Lawrence and E. I. Solomon, *J. Am. Chem. Soc.*, 2007, **129**, 15983.

45 M. Srnec, S. D. Wong and E. I. Solomon, *Dalton Trans.*, 2014, **43**, 17567.

46 S. Ye and F. Neese, *Proc. Natl. Acad. Sci. U. S. A.*, 2011, **108**, 1228.

47 B. K. Mai and Y. Kim, *Inorg. Chem.*, 2016, **55**, 3844.

48 D. Usharani, D. Janardanan, C. Li and S. Shaik, *Acc. Chem. Res.*, 2013, **46**, 471.

49 J. England, Y. Guo, E. R. Farquhar, V. G. Young Jr., E. Münck and L. Que Jr., *J. Am. Chem. Soc.*, 2010, **132**, 8635.

50 M. L. Neidig, A. Decker, O. W. Choroba, F. Huang, M. Kavana, G. R. Moran, J. B. Spencer and E. I. Solomon, *Proc. Natl. Acad. Sci. U. S. A.*, 2006, **103**, 12966.

51 D. Fang, R. L. Lord and G. A. Cisneros, *J. Phys. Chem. B*, 2013, **117**, 6410.

52 J. Olsen, B. O. Roos, P. Jørgensen and H. J. A. Jensen, *J. Chem. Phys.*, 1988, **89**, 2185.

53 B. O. Roos, P. R. Taylor and P. E. M. Siegbahn, *Chem. Phys.*, 1980, **48**, 157.

54 P. J. Knowles and H.-J. Werner, *Chem. Phys. Lett.*, 1988, **145**, 514.

55 H. J. Werner and P. J. Knowles, *J. Chem. Phys.*, 1988, **89**, 5803.

56 K. Andersson, P. Å. Malmqvist and B. O. Roos, *J. Chem. Phys.*, 1992, **96**, 1218.

57 H.-J. Werner, P. J. Knowles, G. Knizia, F. R. Manby, M. Schütz, P. Celani, T. Korona, R. Lindh, A. Mitrushenkov, G. Rauhut, K. R. Shamasundar, T. B. Adler, R. D. Amos, A. Bernhardsson, A. Berning, D. L. Cooper, M. J. O. Deegan, A. J. Dobbyn, F. Eckert, E. Goll, C. Hampel, A. Hesselmann, G. Hetzer, T. Hrenar, G. Jansen, C. Köppl, Y. Liu, A. W. Lloyd, R. A. Mata, A. J. May, S. J. McNicholas, W. Meyer, M. E. Mura, A. Nicklass, D. P. O'Neill, P. Palmieri, D. Peng, K. Pflüger, R. Pitzer, M. Reiher, T. Shiozaki, H. Stoll, A. J. Stone, R. Tarroni, T. Thorsteinsson and M. Wang, *MOLPRO, version 2012.1, a package of ab initio programs*, University College Cardiff Consultants, Ltd., Cardiff, UK, 2012.

58 P. Å. Malmqvist, A. Rendell and B. O. Roos, *J. Phys. Chem.*, 1990, **94**, 5477.

59 P. Å. Malmqvist, K. Pierloot, A. R. M. Shahi, C. J. Cramer and L. Gagliardi, *J. Phys. Chem.*, 2008, **128**, 204109.

60 F. Aquilante, J. Autschbach, R. K. Carlson, L. F. Chibotaru, M. G. Delcey, L. D. Vico, I. F. Galván, N. Ferré, L. M. Frutos, L. Gagliardi, M. Garavelli, A. Giussani, C. E. Hoyer, G. L. Manni, H. Lischka, D. Ma, P. Å. Malmqvist, T. Müller, A. Nenov, M. Olivucci, T. B. Pedersen, D. Peng, F. Plasser, B. Pritchard, M. Reiher, I. Rivalta, I. Schapiro, J. Segarra-Martí, M. Stenrup, D. G. Truhlar, L. Ungur, A. Valentini, S. Vancoillie, V. Veryazov, V. P. Vysotskiy, O. Weingart, F. Zapata and R. Lindh, *J. Comput. Chem.*, 2016, **37**, 506.

61 B. O. Roos, R. Lindh, P.-Å. Malmqvist, V. Veryazov and P.-O. Widmark, *J. Phys. Chem. A*, 2004, **108**, 2851.

62 B. O. Roos, R. Lindh, P.-Å. Malmqvist, V. Veryazov and P.-O. Widmark, *J. Phys. Chem. A*, 2005, **109**, 6575.

63 M. Douglas and N. M. Kroll, *Ann. Phys.*, 1974, **82**, 89.

64 B. A. Hess, *Phys. Rev. A: At., Mol., Opt. Phys.*, 1986, **33**, 3742.

65 G. Ghigo, B. O. Roos and P.-Å. Malmqvist, *Chem. Phys. Lett.*, 2004, **396**, 142.

66 N. Forsberg and P. Å. Malmqvist, *Chem. Phys. Lett.*, 1997, **274**, 196.

67 F. Aquilante, R. Lindh and T. B. Pedersen, *J. Chem. Phys.*, 2007, **127**, 114107.

68 S. Vancoillie, H. Zhao, V. T. Tran, M. F. A. Hendrickx and K. Pierloot, *J. Chem. Theory Comput.*, 2011, **7**, 3961.

69 C. N. Sakellaris, E. Miliordos and A. Mavridis, *J. Chem. Phys.*, 2011, **134**, 234308.

70 *CRC Handbook of Chemistry and Physics*, ed. W. M. Haynes, Taylor and Francis, Boca Raton, FL, 93th edn, 2012.

71 A. Kramida, Y. Ralchenko and J. Reader, *NIST Atomic Spectra Database (ver. 5.5.6)*, 2018, National Institute of Standards and Technology, Gaithersburg, MD. http://physics.nist.gov/asd.

72 A. Kazaryan and E. J. Baerends, *ACS Catal.*, 2015, **5**, 1475.

73 K. Pierloot, Q. M. Phung and A. Domingo, *J. Chem. Theory Comput.*, 2017, **13**, 537.

74 M. Radoń and K. Pierloot, *J. Phys. Chem. A*, 2008, **112**, 11824.

75 J. England, G. J. Britovsek, N. Rabadia and A. J. White, *Inorg. Chem.*, 2007, **46**, 3752.

76 G. Mukherjee, C. W. Z. Lee, S. S. Nag, A. Alili, F. G. Cantu Reinhard, D. Kumar, C. V. Sastri and S. P. de Visser, *Dalton Trans.*, 2018, **47**, 14945–14957.

77 W. Rasheed, A. Draksharapu, S. Banerjee, V. G. Young, Jr., R. Fan, Y. Guo, M. Ozerov, J. Nehrkorn, J. Krzystek, J. Tesler and L. Que, Jr., *Angew. Chem., Int. Ed.*, 2018, **57**, 9387.

Electronic Structure of RhO^{2+}, Its Ammoniated Complexes (NH$_3$)$_{1-5}$RhO^{2+}, and Mechanistic Exploration of CH$_4$ Activation by Them

Shahriar N. Khan and Evangelos Miliordos*

Read Online

ACCESS | Metrics & More | Article Recommendations | Supporting Information

ABSTRACT: High-level electronic structure calculations are initially performed to investigate the electronic structure of RhO^{2+}. The construction of potential energy curves for the ground and low-lying excited states allowed the calculation of spectroscopic constants, including harmonic and anharmonic vibrational frequencies, bond lengths, spin−orbit constants, and excitation energies. The equilibrium electronic configurations were used for the interpretation of the chemical bonding. We further monitored how the Rh−O bonding scheme changes with the gradual addition of ammonia ligands. The nature of this bond remains unaffected up to four ammonia ligands but adopts a different electronic configuration in the pseudo-octahedral geometry of (NH$_3$)$_5$RhO^{2+}. This has consequences in the activation mechanism of the C−H bond of methane by these complexes, especially (NH$_3$)$_4$RhO^{2+}. We show that the [2 + 2] mechanism in the (NH$_3$)$_4$RhO^{2+} case has a very low energy barrier comparable to that of a radical mechanism. We also demonstrate that methane can coordinate to the metal in a similar fashion to ammonia and that knowledge of the electronic structure of the pure ammonia complexes provides qualitative insights into the optimal reaction mechanism.
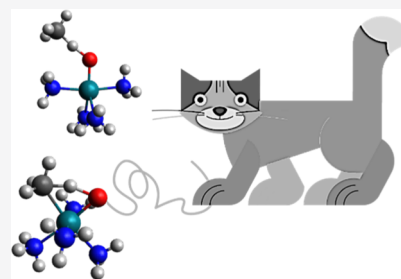
1. INTRODUCTION

Earth-abundant small molecules, such as methane, offer huge potential to satiate our ever-increasing energy demand. Considering the scientific explorations of the last few decades, activation of small molecules has revealed profound complexities. For the activation of C−H bonds, transition metals and their oxides have been treated as a "panacea," and a plethora of research outcomes has been documented in the literature.[1−4]

Because of the presence of low-lying excited states, transition metal (TM) oxides are instrumental in activating chemical bonds. For C−H activation, first-row TM oxides have been widely employed. Theoretical studies on the reaction of CH$_4$ with ScO$^+$,[5] TiO$^+$,[5] VO$^+$,[5] CrO$^+$,[5,6] MnO$^+$,[5,7] FeO$^+$,[5,7−10] CoO$^+$,[5,11] NiO$^+$,[5] CuO$^+$,[5] and ZnO[12] have provided fundamental insights into their efficiency to activate methane. On the contrary, the study on the second-row TM oxides for methane activation is sporadic. For example, molybdenum,[6,13] rhodium,[14] and palladium[15] oxides have been suggested theoretically as prospective options. This also indicates the increasing difficulty to work with a second-row transition metal incorporating many electron correlation energy and relativistic effects.

To investigate the mechanism of C−H bond activation with TM oxides and the role of the excited electronic channels, it is imperative to understand the electronic structure of the involved molecules.[16,17] Prior to this work, we have investigated the electronic structures of FeO^{2+},[18] ZrO,[19] NbO,[20] MoO^{2+},[21] RuO$^{+/2+}$,[22,23] and FeOCH$_3$$^{+}$[24] and their

role in methane activation. Generally, metal oxides can exhibit two different electronic structures, namely, -oxo and -oxyl. In the -oxo species, the metal (M) oxide has a predominant M^{2+}O^{2-} electronic configuration, whereas in the -oxyl species, there is one less electron near the oxygen terminal and the metal oxide has a predominant M^{+}O$^{\bullet-}$ radical character. Typically, the -oxyl moiety has a longer bond length than the -oxo moiety because of the weaker metal−oxygen binding. From our FeO^{2+} study, the ground state $^3\Delta$ is of -oxyl character. However, higher-energy -oxo structures ($^5\Sigma^+$ and $^5\Pi$) can be stabilized by using proper ligands.[18] Although useful insights can be obtained by the study of naked metal oxides and their reaction with CH$_4$, practical applications require the knowledge of the role of the ligands and the co-operativity of the metal and ligand "personality". Our goal here is to see the co-operation of ligands and metals for a second-row TM oxide and specifically RhO^{2+}.

Our interest in RhO^{2+} started from a different viewpoint as well. The oxo wall is a rather well-established notion for transition metal oxides and is usually placed between iron and

cobalt.[25−27] The meaning is that metal oxide complexes based on a metal heavier than iron do not adopt an oxo ground state in an octahedral geometry. This is not true for a tetrahedral structure; see, for example, the CoO^{2+} complex synthesized four years ago.[28] In addition, our work on FeO^{2+} and RuO^{2+} indicates that the second-row transition metal oxides favor an oxo electronic structure and poses questions about the applicability of the oxo wall in second-row transition metal complexes.[18,23] Ruthenium-oxo complexes have been synthesized,[29] but Rh-terminal oxygen complexes are rare in the literature.[30] Presently, we explore RhO^{2+} as the second-row analogue of CoO^{2+} to investigate its electronic structure and determine on which side of the oxo wall it is.

Many studies have been carried out on neutral RhO on both the theoretical[31−36] and experimental[37−41] fronts. The ground state of RhO has been assigned as $^4\Sigma^-$, but to our best knowledge, there is limited information on the electronic structures of charged RhO. In this project, we have studied the ground and excited states of RhO^{2+} using multi-reference techniques. Considering different spin multiplicities, we have tabulated the energy order of the electronic states along with their spectroscopic constants. Also, we have considered the effect of spin−orbit coupling to assign spin−orbit states of RhO^{2+}.

For methane activation with RhO^{2+}, we have considered three spin multiplicities of RhO^{2+} and included up to five ammonia ligands in the system to study the activation barrier with respect to the coordination number. The ionization energy of RhO^+ is ∼18 eV, which is higher than the ionization energy of CH_4 ∼12 eV. This causes an additional issue in the calculations, which tend to ionize methane and reduce the metal oxide dication. The molecular system requires at least four ammonia ligands to stabilize RhO^{2+} (or better $(NH_3)_4RhO^{2+}$) over CH_4^+. Generally, in presence of metal oxides, the C−H bond activation occurs through two possible mechanisms: by the formation of radical intermediates or the [2 + 2] addition mechanism.[42] Herein, we report the activation barrier of the C−H bond and compare the energy diagrams for both radical and [2 + 2] addition mechanisms.

Computational details are presented in Section 2. A comprehensive discussion of our findings is documented in the following sections. Section 3.1 deals with the electronic structure of RhO^{2+} in ground and excited states of the titled species, considering different spin multiplicities, their spectroscopic constants, and spin−orbit coupling. Section 3.2 is the demonstration of the CH_4 activation mechanism with ammonia-ligated RhO^{2+}. Finally, Section 4 contains our concluding remarks.

2. COMPUTATIONAL DETAILS

To construct the potential energy curves (PECs) of RhO^{2+}, we have considered the C_{2v} point group symmetry (largest Abelian subgroup of the full $C_{\infty v}$ point group of the molecule) in our calculation. PECs are constructed with the multi-reference configuration interaction (MRCI) starting from a complete active space self-consistent field (CASSCF) reference wavefunction. The selected active space consists of 11 electrons in 9 orbitals, namely, 5s and 4d orbitals of Rh and 2p orbitals of O at long interatomic distances. For all low-lying states, preliminary state-average CASSCF calculations showed that the 2s of oxygen is doubly occupied in all configurations. To reduce the computational cost, these 2s electrons are not

included in the active space, but they are correlated at the MRCI level.

To incorporate dynamic electron correlation, all single and double excitations from the valence (including 2s of oxygen) to the virtual orbitals are allowed at MRCI. In addition, to reduce the size-extensivity error, the Davidson correction has been considered, and the PECs reported herein are of MRCI + Q method.

Rhodium, being a second-row transition metal, demands the consideration of relativistic effects. Stuttgart relativistic pseudopotential (accounting for 28 inner electrons) combined with the quintuple-ζ quality basis set (cc-pV5Z-PP)[43−45] is invoked for Rh, whereas a diffuse basis set (aug-cc-pV5Z) is used for O, owing to its higher electron affinity and polarity of the metal−oxygen bond. Two sets of PECs were constructed. The quintuple-ζ (5z) basis set was used for the construction of PECs around equilibrium (1.2−3.5 Å) and extraction of our numerical results. However, we reduced the basis set to the triple-ζ (tz) quality for the construction of full PECs. At the asymptotic dissociation limit, the computations are extremely challenging and forced us to use a smaller basis set.

To chart the spectroscopic constants, along with MRCI and MRCI + Q, we have also employed core MRCI (C-MRCI) calculations, where we have included dynamic electron correlation from the 4s and 4p electrons of Rh. For this purpose, a weighted-core basis (cc-pwCV5Z-PP) is employed for Rh. We have also performed CCSD(T) and C-CCSD(T) calculations for low-lying states, which are single reference. The first five vibrational levels were used to obtain harmonic frequencies and anharmonicities. In all cases, none of these levels is energetically close to avoided crossings and they are not perturbed by them.

To account for the spin−orbit coupling, PECs of the spin−orbit states are reported in the Supporting Information (Figure S4 and Table S3). These calculations are performed by diagonalizing the Breit−Pauli Hamiltonian. The MRCI wavefunctions with the quintuple-ζ basis set are used as basis to construct the Breit−Pauli Hamiltonian. Finally, the spectroscopic constants for all the states reported, herein, are calculated by solving the rovibrational Schrödinger equation numerically. All multi-reference calculations are performed by using the MOLPRO 2015 electronic structure package.[46]

For the methane activation part, calculations are performed with density functional theory (DFT, unrestricted Kohn−Sham formulation) using the MN15 functional.[47] MN15 is suggested in the literature for its accuracy with transition metals and non-covalent interactions.[47] We have studied the reaction of $(NH_3)_{1−5}RhO^{2+}$ with CH_4, considering three spin multiplicities (doublet, quartet, and sextet) and optimized every reactant, product, and transition state (TS) with triple-ζ basis sets. As in naked RhO^{2+}, Stuttgart relativistic pseudopotential and a diffuse basis set is used for Rh and O, respectively. The calculations for the TSs are accompanied by harmonic frequency calculations, which corroborated the TS structures to be first-order saddle points (one imaginary frequency). Then, the intrinsic reaction coordinates calculation is invoked to locate the reactants and products. Finally, the geometry optimization of the reactants and products is supported by harmonic frequency calculations, which produced only real frequencies. We have used Gaussian 16 electronic structure codes for the DFT calculations.[48]
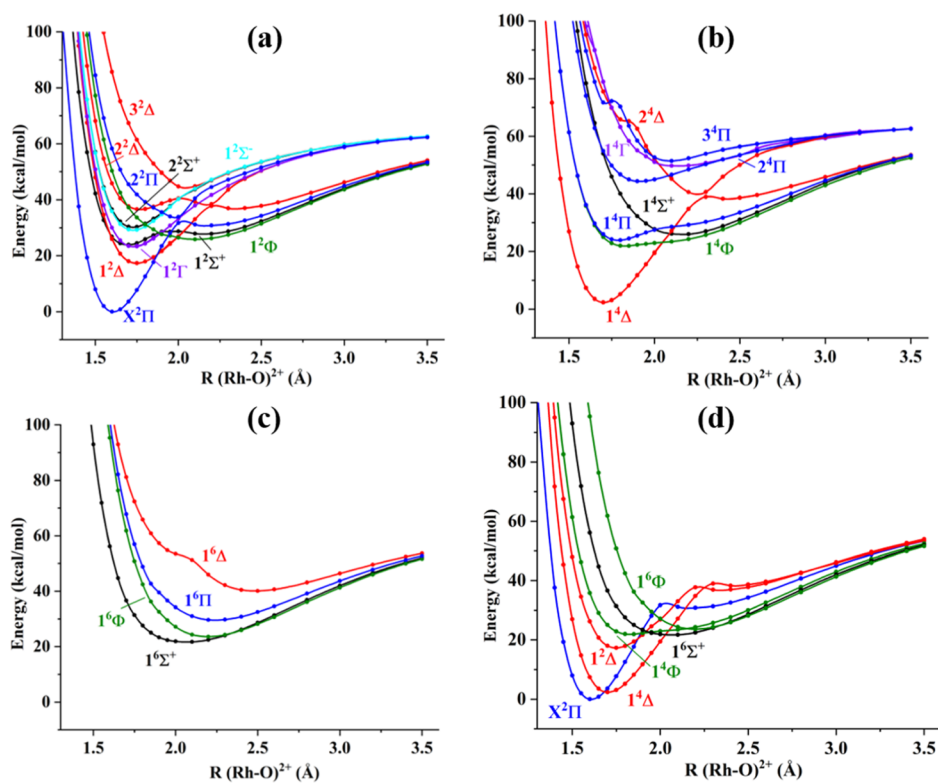
Figure 1. PECs of RhO^{2+} with respect to Rh−O distance for different spin multiplicities: (a) doublet, (b) quartet, and (c) sextet at the MRCI + Q/5z level. The lower-right graph (d) is the PECs of a few low-lying states of RhO^{2+}, considering all the spins together.

3. RESULTS AND DISCUSSION

A comprehensive presentation of the ground and excited states of RhO^{2+} is imperative to understand the involved reaction mechanism with methane. In section 3.1, we start our discussion with the electronic structure of RhO^{2+}. In section 3.2, we present the C−H bond activation.

3.1. Electronic Structure of RhO^{2+}. Figure 1 presents the PECs of the equilibrium region for doublet 1(a), quartet 1(b), sextet 1(c), and all the spin multiplicities combined 1(d). The same PECs for a larger distance range are shown in the Supporting Information (Figures S1−S3). There are two different potential energy wells; the steeper wells with minima at 1.6−1.8 Å and the shallower ones with minima beyond 2.0 Å. The ground state undergoes an avoided crossing at about 2.0 Å, and the first two excited states $1^{2,4}\Delta$ cross at 2.2−2.3 Å with higher energy curves of the same spin and spatial symmetry. Doublet and quartet states form generally stronger and shorter bonds as opposed to sextets. To get a better understanding of the morphology of the PECs, we next take a more detailed look on the bonding features of the low-lying electronic states.

Figure 2 depicts the valence molecular orbital contours of RhO^{2+} at equilibrium. The molecular orbitals 2σ, 3σ, 1π, and 2π have significant contribution from both the metal and the oxygen atom, whereas 1δ and 4σ orbitals are mostly localized on the metal. The $2\sigma/3\sigma$ and $1\pi/2\pi$ orbitals represent the σ- and π-bonding/antibonding Rh−O orbitals ($3\sigma \approx \sigma_{RhO}^*$ and $2\pi \approx \pi_{RhO}^*$). The dominant electronic configurations are listed in Table 1, and spectroscopic constants for the low-lying electronic states are tabulated in Table 2. Complete lists for all states studied are provided in the Supporting Information (Tables S1 and S2).
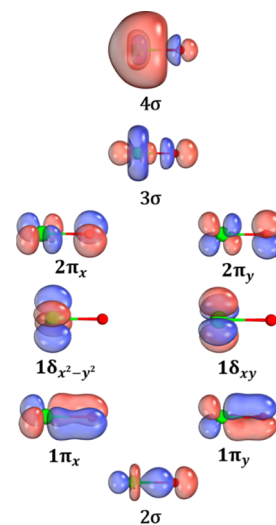
Figure 2. Selected valence molecular orbital contours of RhO^{2+} at equilibrium. The green sphere is Rh and the red one is oxygen. Only valence orbitals are numbered; 1σ (not shown here) corresponds to the 2s of oxygen.

The ground state $^2\Pi$ of RhO^{2+} has the shortest bond length of 1.608 Å (see Table 2, MRCI + Q) and is only 0.1 eV lower in energy than the first excited state $^4\Delta$. For the ground state, the C-MRCI + Q values closely follow the MRCI + Q values, which indicates the minimal effect of the core electron correlation. The same small effect holds true for the +Q correction. Specifically, going from MRCI to C-MRCI + Q, the bond length r_e changes only by 0.002 Å (0.1%), the harmonic vibrational frequency ω_e changes by 2.4 cm^{-1} (0.3%), and the anharmonicity $\omega_e x_e$ changes by 0.4 cm^{-1} (5%). The dominant

Table 1. Dominant Electronic configuration for the Lowest Electronic States of RhO^{2+} [a]

state	coef.	2σ	3σ	4σ	$1\pi_x$	$2\pi_x$	$1\pi_y$	$2\pi_y$	$1\delta x^2-y^2$	$1\delta_{xy}$
X$^2\Pi$	0.88	2	0	0	2	α	2	0	2	2
1$^4\Delta$	0.92	2	0	0	2	α	2	α	2	A
1$^2\Delta$	0.71	2	0	0	2	α	2	α	2	B
	−0.35	2	0	0	2	α	2	β	2	A
	−0.35	2	0	0	2	β	2	α	2	A
1$^6\Sigma^+$	0.83	2	α	0	2	α	2	α	α	A
	−0.39	2	α	0	α	α	α	α	2	2
1$^4\Phi$	−0.62	2	α	0	2	0	2	α	2	A
	0.62	2	α	0	2	α	2	0	α	2
1$^2\Gamma$	0.44	2	0	0	2	0	2	2	2	A
	−0.44	2	0	0	2	2	2	0	2	A
	−0.44	2	0	0	2	α	2	β	α	2
	0.44	2	0	0	2	β	2	α	α	2
1$^6\Phi$	0.67	2	α	0	α	α	2	α	2	A
	−0.67	2	α	0	2	α	α	α	α	2
1$^4\Pi$	0.63	2	α	0	2	0	2	α	2	A
	0.63	2	α	0	2	α	2	0	α	2
1$^2\Sigma^+$	0.77	2	α	0	2	0	2	0	2	2

[a] The A$_1$ and B$_1$ irreducible representation of the C_{2v} subgroup components for Δ and Γ (Π and Φ), respectively, are only given.

Table 2. Equilibrium Energy E_e (a.u.), Bond Length r_e (Å), Harmonic Vibrational Frequencies ω_e (cm^{-1}), Anharmonicity $\omega_e x_e$ (cm^{-1}), $\Delta G_{1/2}$ (cm^{-1}) Value, and Excitation Energy T_e (eV) for the Lowest Electronic States of RhO^{2+} [a]

state	method	r_e	ω_e	$\omega_e x_e$	$\Delta G1/2$	T_e
X$^2\Pi$	MRCI	1.610	951.4	7.8	935.9	0.000
	MRCI + Q	1.608	955.9	7.8	940.3	0.000
	C-MRCI	1.613	945.5	7.7	930.3	0.000
	C-MRCI + Q	1.612	953.8	7.4	939.1	0.000
	CCSD(T)	1.595	966.4	−4.6	975.9	0.000
	C-CCSD(T)	1.598	956.5	−7.1	969.7	0.000
1$^4\Delta$	MRCI	1.705	795.6	6.8	781.6	0.106
	MRCI + Q	1.703	798.9	6.8	785.0	0.102
	C-MRCI	1.708	787.1	7.0	772.1	0.153
	C-MRCI + Q	1.705	796.8	6.6	782.9	0.172
	CCSD(T)	1.687	878.5	7.2	863.1	0.147
	C-CCSD(T)	1.683	904.3	8.4	885.9	0.201
1$^2\Delta$	MRCI	1.754	666.7	6.6	653.7	0.751
	MRCI + Q	1.749	694.0	7.9	665.3	0.752
	C-MRCI	1.755	669.8	6.4	657.4	0.751
	C-MRCI + Q	1.745	711.6	7.7	686.0	0.767
1$^6\Sigma^+$	MRCI	2.122	304.1	0.5	306.0	0.828
	MRCI + Q	2.073	293.3	−1.7	291.8	0.942
1$^4\Phi$	MRCI	1.896	136.5	−12.5	140.3	0.892
	MRCI + Q	1.825	262.3	1.3	297.7	0.951
1$^2\Gamma$	MRCI	1.737	681.5	11.9	656.9	0.989
	MRCI + Q	1.722	697.8	11.7	681.2	1.010
1$^6\Phi$	MRCI	2.219	350.2	2.4	345.0	0.866
	MRCI + Q	2.196	349.4	2.3	344.7	1.026
1$^4\Pi$	MRCI	1.796	434.3	29.6	455.9	0.998
	MRCI + Q	1.789	614.2	40.7	534.3	1.037
1$^2\Sigma^+$	MRCI	1.698	316.4	18.7	393.8	0.994
	MRCI + Q	1.695	675.5	62.9	612.6	1.038

[a] The energy order of the states is based on the MRCI + Q values.

CI coefficient and the electronic configuration of this state are 0.88 $|2\sigma^2 1\pi_x^2\ 2\pi_x^1 1\pi_y^2 1\delta_{x^2-y^2}^2\ 1\delta_{xy}^2\rangle$, suggesting a single reference character and enabling the use of CCSD(T). At both CCSD(T) and C-CCSD(T), the equilibrium bond distance is found to be shorter than that by the corresponding MRCI + Q and C-MRCI + Q methods by 0.013 and 0.014 Å. Similar differences were found for RuO^{2+}.[23] CCSD(T) PECs are steeper, resulting in an increase in the harmonic frequency by ~10 cm^{-1}. We believe that CCSD(T) bond lengths are more accurate (larger electron correlation) but MRCI frequencies are more trustable because MRCI includes more configurations in the region longer than r$_e$ in order to adjust to the avoided crossing at 2.0 Å. Compared to RuO^{2+}, the additional electron populates the 2π antibonding orbital, disrupting the "triple" bond of RuO^{2+23} and increasing the metal oxygen bond length by 0.06 Å at MRCI + Q. In addition, the 2π orbital gives some O$^\bullet$ radical character to the system (see Figure 2).

The first excited state 1$^4\Delta$ has an equilibrium bond distance of 1.703 Å at the MRCI + Q level, almost 0.1 Å longer than the ground state, and it decreased to 1.687 Å at the CCSD(T) level. Alike the ground state, the first excited state is also single reference with a CI coefficient of 0.92, and one 1δ (nonbonding) electron moved to the 2π (anti-bonding) orbital (see Table 1), which explains the elongation of the bond. The excitation energy of this state is 0.106 eV at MRCI and increases to 0.172 and 0.201 eV for C-MRCI + Q and C-CCSD(T), respectively. The reduction in the bond order decreases the harmonic vibrational frequency as well considerably by more than 150 cm^{-1} (see Table 2).

The second excited state is 1$^2\Delta$, which lies 0.75−0.77 eV (depending on the method) higher than the ground state. It can be produced from its sister quartet state (1$^4\Delta$) by spin-flip of one of the three unpaired electrons ($2\pi^2 1\delta^1$); see Table 2. Interestingly, the equilibrium bond distance increases by ~0.05 Å due to the spin change, and the vibrational frequency drops by at least 80 cm^{-1} (C-MRCI + Q) or 120 cm^{-1} at MRCI and C-MRCI.

Within an energy range of 0.94−1.0 eV, there are six excited states of different spin multiplicities in the following order: 1$^6\Sigma^+$, 1$^4\Phi$, 1$^2\Gamma$, 1$^6\Phi$, 1$^4\Pi$, and 1$^2\Sigma^+$. Except for 1$^2\Sigma^+$, the rest five states have high multireference character, involving reallocation of 1π (π_{Rh-O}) and $1\delta_{(Rh)}$ electrons to 2π (π^*_{Rh-O}) and/or 3σ (σ^*_{Rh-O}). In terms of equilibrium bond length, 1$^6\Sigma^+$, 1$^4\Phi$, 1$^6\Phi$, and 1$^4\Pi$ have the bond distances of 2.073, 1.825, 2.196, and 1.789 Å, respectively. The longer bond length (relatively) of these states is the result of the population of the 3σ (anti-bonding) orbital. 1$^6\Sigma^+$ and 1$^4\Phi$ have negative anharmonicity values, which suggests unusual morphology of their PECs. Indeed, 1$^6\Sigma^+$ and 1$^4\Phi$ have a flat region near the equilibrium, and 1$^4\Phi$ tends to form a second minimum at ~2.25 Å; see Figure 1c,b. The doublet states can be generated by moving the 2π electron of the ground state to the 3σ orbital (1$^2\Sigma^+$) or moving one 1δ electron and coupling it with the 2π electron of the ground state (1$^2\Gamma$). In the first case, the electron migrates from a π^* to a σ^* orbital, and thus, the bond length elongates by 0.08−0.09 Å but less than that in the second case (0.12−0.13 Å), where we have a δ (non-bonding) $\rightarrow \pi^*$ transition.

3.2. H$_3$C−H Bond Activation Using (NH$_3$)$_{1-5}$RhO^{2+}. In this section, we investigate the reaction of methane with a RhO^{2+} unit coordinated with ammonia ligands. We obtained the optimal structure of the reactants, TSs, and products for all

titled complexes in their lowest doublet, quartet, and sextet spin states (see Supporting Information). Ammonia represents commonly used larger ligands coordinating to the metal with the lone pair of the nitrogen atom.[49] The number of ammonia ligands is varied from one to five to monitor the effect of the ligands on the electronic structure of the RhO^{2+} unit, as we move from the naked to an octahedral $(NH_3)_5RhO^{2+}$ unit, and how this affects the C−H bond activation mechanism. Methane is selected for three reasons: (1) it represents saturated hydrocarbons with the strongest C−H bond, (2) its conversion to methanol is a topic of high interest in the literature,[50−53] and (3) its small size serves perfectly our computational needs/goal.

First, we examine the geometric electronic structure of $(NH_3)_{1-5}RhO^{2+}$ coordination complexes. The first ammonia ligand binds with a N−Rh−O angle 128°, and the second one binds similarly making an ammonia−ammonia−oxygen triangle, and the geometries of the rest ones are shown in Figure 3. $(NH_3)_5RhO^{2+}$ is octahedral, $(NH_3)_4RhO^{2+}$ is trigonal

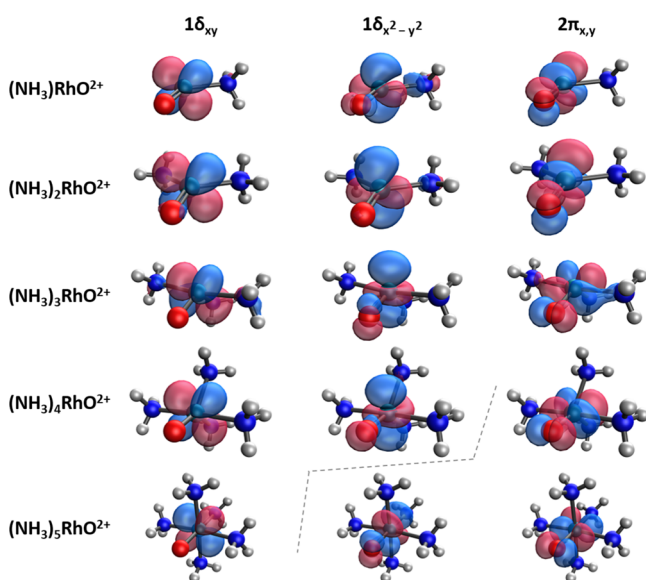**Figure 3.** Electronic structure determining molecular orbitals (MN15/tz) of $(NH_3)_{1-5}RhO^{2+}$. The notation follows that of plain RhO^{2+} for simplicity. The first two orbitals are doubly occupied, and the last one is singly occupied. Notice that ammonia ligands coordinate in specific orientations to minimize overlap with the occupied orbitals and that $1\delta_{x^2-y^2}$ is replaced with a 2π orbital in the case of $(NH_3)_5RhO^{2+}$.

bipyramidal, and $(NH_3)_3RhO^{2+}$ is trigonal bipyramidal with one equatorial ammonia missing. Figure 3 depicts also selected occupied Rh−O molecular orbitals. Recall that the ground doublet state of RhO^{2+} has a $2\sigma(=\sigma_{RhO})^2 \ 1\pi(=\pi_{RhO})^4 \ 1\delta^4 \ 2\pi(=\pi_{Rh}O^*)^1$ configuration (see Figure 2 for molecular orbital contours). The ground state remains a doublet (see below and Supporting Information) with practically the same electronic configuration $(\sigma_{RhO}^2\pi_{RhO}^4 1\delta^4 \pi_{RhO}^{*1})$ for all complexes up to four ammonia ligands. The ligands are placed in a way that the nitrogen lone pairs do not overlap with $1\delta_{xy}$ or $2\pi_{x,y}$ and have minimal overlap with $1\delta_{x^2-y^2}$. In the case of octahedral $(NH_3)_5RhO^{2+}$, the $1\delta_{x^2-y^2}$ orbital, which has strong Rh−N antibonding character (e_g), is replaced with a 2π non-bonding (t_{2g}) orbital. Therefore, only the t_{2g} orbitals (t_{2g}^5) are occupied in $(NH_3)_5RhO^{2+}$. As shown below, this "mutation" plays an

important role in the C−H activation process. Another effect of this "mutation" is that the RhO bond length increases considerably because of the 1δ (non-bonding) → 2π (π_{RhO}^*, antibonding) electron promotion. The bond elongates by ~0.05 Å going from $n = 2$ to 3 (1.59−1.64 Å) and from 3 to 4 (1.64−1.70 Å) but by 0.17 Å going from 4 to 5.

The approach of a methane molecule to any of the $(NH_3)_{1-5}RhO^{2+}$ compounds results in two kinds of interactions. In the first kind, a hydrogen atom of methane forms a weak electrostatic interaction with the oxygen terminus, and this will finally lead to the production of a methyl radical (radical C−H activation mechanism). In the second kind, methane coordinates to the metal in a similar fashion to ammonia. For example, the $(CH_4)(NH_3)RhO^{2+}$ complex resembles $(NH_3)_2RhO^{2+}$. The attachment of methane to the Rh^{4+} center happens between the electron pair of one C−H bond and rhodium and resembles that between the electron pair of ammonia and rhodium. Figure 4 shows clearly
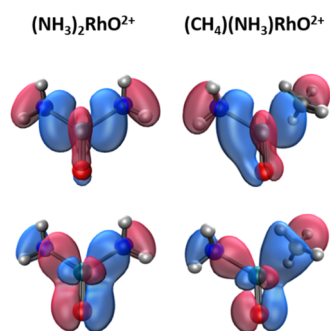

Figure 4. Molecular orbitals of the Rh−N bonds of $(NH_3)_2RhO^{2+}$ compared to those of the Rh−N and "Rh−C" bonds of $(CH_4)(NH_3)RhO^{2+}$.

this correspondence for $(NH_3)_2RhO^{2+}$ and $(CH_4)(NH_3)RhO^{2+}$. This second type of interaction leads to the oxidative addition of methane to RhO^{2+} ([2 + 2] mechanism) forming $(NH_3)CH_3RhOH^{2+}$. The binding energy of ammonia to Rh(IV) is between 53.3 $[(NH_3)_5RhO^{2+}]$ and 99.8 $[(NH_3)_2RhO^{2+}]$ kcal/mol, while that of methane is smaller ranging from 10.6 $[(CH_4)(NH_3)_4RhO^{2+}]$ to 48.6 $[(CH_4)(NH_3)RhO^{2+}]$ kcal/mol.

The radical and [2 + 2] mechanisms correspond to the homolytic and heterolytic dissociation of the H_3C−H bond. In the radical mechanism, a proton is transferred from methane to oxygen with a simultaneous transfer of an electron to the metal center (proton-coupled electron transfer = PCET).[54] For the ground doublet state and all complexes, the resulting product is a closed shell $(NH_3)_{2-5}RhOH^{2+}$ and a doublet $CH_3^{\bullet}$ radical, which suggests that the migrating electron couples to the existing πRhO^* (or 2π) electron. The proton transfer is facilitated by the $1\pi^2$ electrons and the electron transfer is mediated by the 2π orbital.[54] The [2 + 2] mechanism proceeds with the transfer of the proton to oxygen but now the remaining CH_3^- moiety binds to Rh^{4+}, making $(NH_3)_{1-4}CH_3RhOH^{2+}$. Figure 5 helps to compare the TSs for the two mechanisms of the $CH_4 + (NH_3)_4RhO^{2+}$ reaction.

The activation energy barriers $\Delta E^{\ddagger}$ for the two mechanisms in the lowest doublet, quartet, and sextet states are listed in Table 3. Focusing on the ground doublet state, $\Delta E^{\ddagger}$ of the radical mechanism is 12.8−15.3 kcal/mol for $3 \leq n \leq 5$ and practically non-existent for $n = 2$. For $n = 1$, we were not able
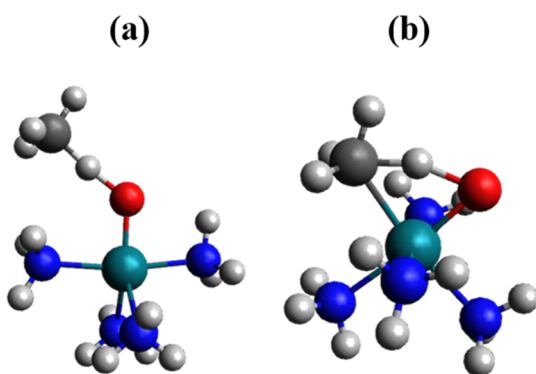
Figure 5. TS for the C−H bond activation of methane with RhO^{2+}(NH$_3$)$_4$ ($S = 1/2$): (a) radical mechanism and (b) [2 + 2] addition mechanism.

Table 3. MN15 C−H Bond Activation Energy Barriers $\Delta E^{\ddagger}$ (kcal/mol) of the Radical and [2 + 2] Addition Mechanisms for the CH$_4$ + (NH$_3$)$_n$RhO^{2+} Reaction with Different Spin (S) Multiplicities

	$S = 1/2$		$S = 3/2$		$S = 5/2$
n	radical	[2 + 2]	radical	[2 + 2]	radical
1		27.7		27.0	
2	0.4	22.9		27.8	24.9
3	15.3	30.9	17.7	27.5	10.5
4	14.8	13.6	16.7	40.8^a	14.3
5	12.8		20.0		16.7

^{a}Single-point energy calculation using the $S = 1/2$ optimized structure.

to locate a TS. The [2 + 2] values are between 22.9 and 30.9 kcal/mol for $1 \leq n \leq 3$, but surprisingly, $\Delta E^{\ddagger}$ drops to 13.6 kcal/mol, entering the radical $\Delta E^{\ddagger}$ range for $n = 4$. Steric effects prevent the coordination of CH$_4$ to Rh for $n = 5$, and thus, no [2 + 2] TS is possible. Zero-point energy-corrected barriers and free energy barriers are listed in Table S10 of the Supporting Information. The absolute values have decreased (as expected) by not more than 5 kcal/mol, but the relative barriers (radical vs [2 + 2]) remain the same within 2 kcal/mol. To benchmark the accuracy of MN15, we employed higher-level electronic structure methods to calculate the unexpectedly small C−H activation barrier of the CH$_4$ + (NH$_3$)$_4$RhO^{2+} reaction ([2 + 2] mechanism). Second-order Møller Plesset perturbation theory (MP2), coupled-cluster singles doubles (CCSD), and perturbative triples [CCSD(T)] gave 13.1, 16.6, and 13.7 kcal/mol values. The MP2 and CCSD(T) values are in excellent agreement with MN15 (13.6 kcal/mol). Finally, to gauge the solvent effects on the same activation barrier, we employed the polarizable continuum model combined with a polar (water) and a non-polar (toluene) solvent. The values changed to 15.6 and 14.2 kcal/mol, respectively. The small change is attributed to the fact that solvent effects affect the energy of reactants, products, TSs nearly the same.

To understand the low activation barrier for the [2 + 2] route of CH$_4$ + (NH$_3$)$_4$RhO^{2+}, we resorted to Figure 3. The initially formed (CH$_4$)(NH$_3$)$_4$RhO^{2+} complex resembles (NH$_3$)$_5$RhO^{2+} with one ammonia being replaced with methane (see discussion above and Figure 4). Unlike the smaller (CH$_4$)(NH$_3$)$_{1-3}$RhO^{2+} complexes, the "absence" of $1\delta_{x^2-y^2}$ (e$_g$), which screens the nuclear charge more efficiently, seems to facilitate the binding of CH$_3^-$ to Rh(IV); see Figure

5. An additional factor is the small interaction/stabilization energy of CH$_4$···(NH$_3$)$_4$RhO^{2+} (10.6 kcal/mol; see above), probably due to steric effects, which prevents "trapping" (over-stabilization) of methane in the first coordination sphere of the metal. To support this hypothesis, we studied the reaction of (NH$_3$)$_4$NiO^{2+} + CH$_4$. In this case, (NH$_3$)$_5$NiO^{2+} has a t$_{2g}^5$e$_g^1$ ($S = 1$) ground-state configuration and the activation barrier of the [2 + 2] mechanism increases to 29.6 kcal/mol at the MN15/cc-pVTZ level of theory (see Supporting Information).

In the past, we have seen for ZrO and NbO that the [2 + 2] mechanism is less favorable not only for the generally high activation barrier of the C−H bond activation but also for the high activation barrier of the CH$_3$ and OH recombination step to make methanol.[19,20] To see if the activation barrier of the latter step is high for (NH$_3$)$_4$RhO^{2+} + CH$_4$, we calculated the complete energy landscape toward (NH$_3$)$_4$Rh^{2+} + CH$_3$OH. Figure 6 shows both the electronic and free energy (25 °C and
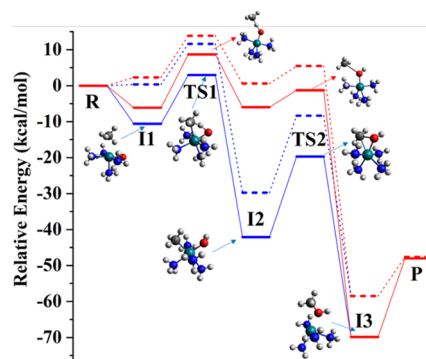
Figure 6. Energy landscape ($S = 1/2$) for the CH$_4$ + (NH$_3$)$_4$RhO^{2+} → CH$_3$OH + (NH$_3$)$_4$Rh^{2+} reaction, following [2 + 2] addition mechanism (blue lines) and radical mechanism (red lines) where R = reactants (CH$_4$ + (NH$_3$)$_4$RhO^{2+}), I = reaction intermediates, TS = transition states, and P = products (CH$_3$OH + (NH$_3$)$_4$Rh^{2+}). Solid lines correspond to electronic energy and dashed lines correspond to free energy (25 °C and 1 atm).

1 atm) diagrams. The zero of the energy scale is set to the initial reactants (NH$_3$)$_4$RhO^{2+} + CH$_4$, I1 is their interacting complex, TS1 is the TS of the C−H bond activation, I2 is the product of the [2 + 2] process (NH$_3$)$_4$(CH$_3$)RhOH^{2+} or of the radical process (NH$_3$)$_4$RhOH^{2+}···CH$_3$, TS2 is the TS of the CH$_3$−OH recombination step, and I3 is the interacting complex of the products (NH$_3$)$_4$Rh^{2+} + CH$_3$OH. The structures of these species are given in the Supporting Information. In agreement with our past findings, the activation barrier of the [2 + 2] recombination step is higher than that of the radical path (4.7 vs 22.4 kcal/mol), but five times smaller than that observed for ZrO and NbO.[19,20] In addition, the first step of the [2 + 2] mechanism is more exothermic than that of the radical path, placing TS2 of [2 + 2] lower in energy than the radical TS2. Therefore, the interplay of these factors (activation barriers and exothermicity) make the two mechanisms highly competitive.

We were able to locate TS1 (C−H bond activation step) for the two mechanisms in the quartet potential energy surface as well. For CH$_4$ + (NH$_3$)$_4$RhO^{2+}, we were not able to locate a [2 + 2] TS, but we performed a single point energy calculation using doublet-spin TS geometry. The energy of reactants, TSs, and products of the quartet state are always higher than that of the doublet, and thus, there is no evidence for two-state

reactivity. The $\Delta E^{\ddagger}$ values are quite consistent with those of the doublet ground state: the radical mechanism has activation barriers between 16.7 and 20.0 kcal/mol, and the [2 + 2] barriers are 27−28 kcal/mol (see Table 3) for $1 \leq n \leq 3$. The estimated $\Delta E^{\ddagger}$ value for $n = 4$ is actually larger (40.8 kcal/mol), in complete contrast to the doublet $\Delta E^{\ddagger}$ value of 13.6 kcal/mol. This fact can be attributed to the $t_{2g}^4 e_g^1$ configuration of the quartet, which does have an electron in the non-innocent $1\delta_{x^2-y^2}^2$ $(=e_g)$ orbital, supporting further our explanation for the low activation barrier of the doublet state.

Finally, we examined the sextet state, which was found higher than both quartet and doublet for all structures. The sextet state has an unpaired electron in the bonding π_{RhO} orbital, and the formation of a $(NH_3)_{1-5}CH_3RhOH^{2+}$ complex with multiple metal−ligand bonds (including Rh−OH and Rh−CH$_3$) and five unpaired metallic electrons was not possible. Therefore, the radical mechanism prevails and proceeds with a different electronic structure path: One $\sigma(H_3C-H)$ electron couples to the π_{RhO} unpaired electron as happens for early transition metal oxides (hydrogen atom transfer or HAT).[19,20,55] The $\Delta E^{\ddagger}$ values are in the same range as the previous values for the radical mechanism of doublet and quartet (10.5−24.9 kcal/mol).

4. SUMMARY AND CONCLUSIONS

In the present work, we explored the electronic structure of the rhodium oxide dication in its ground and several excited electronic states. We constructed PECs, and we demonstrated (see Supporting Information) the difficulties to describe the region around 4 Å, where multiple avoided crossings occur between ground and excited states of the homolytic and heterolytic dissociation asymptotes. We calculated the spectroscopic data (equilibrium bond lengths, vibrational frequencies, and excitation energies), and we noticed the minor effect of the core-valence electron correlation. Spin−orbit effects were also considered for the lowest lying states.

Wavefunction information is provided for all of the examined states. The ground state has a rich ionic $Rh^{4+}O^{2-}$ character with five metallic electrons occupying the two d_δ and one 2π $(\sim\pi RhO^*)$ orbitals. The latter electron gives partial $O^{\bullet-}$ character, which facilitates the observed PCET mechanism. This is preserved upon addition of up to four ammonia ligands. The addition of a fifth ammonia completes the first coordination sphere and stabilizes the second 2π orbital over one of the d_δ $(\sim d_{x^2-y^2})$ orbitals. The two 2π and the other d_δ $(\sim d_{xy})$ constitute the t_{2g} orbitals, leading to a t_{2g}^5 ground state. The singly occupied 2π orbital maintains the partial $O^{\bullet-}$ character of the complex.

The reaction of methane with these complexes was studied by means of DFT. The optimized structures of the reactants, TSs, and products are provided for the lowest doublet, quartet, and sextet states. We show that methane coordinates to Rh in a similar fashion to ammonia, but the role of the lone pair of ammonia is undertaken by one of the C−H bond pairs. We identified three types of C−H activation mechanisms: the "pure" radical mechanism (HAT) of the oxyl character of the sextet state, the PCET-type radical mechanism of the oxo character of the ground doublet state, and the [2 + 2] mechanism of the oxo ground state. The two types of radical mechanisms bear similar activation energies, which are generally twice smaller than the [2 + 2] ones, except for the $(NH_3)_4RhO^{2+}$ doublet case. The small activation barrier of the latter case falls close to that of the radical processes and was

explained by the electronic structure of the (CH_4)-$(NH_3)_4RhO^{2+}$ complex. For this system, the recombination step of CH$_3$ and OH for the production of methanol has also small activation barriers for both mechanisms, and especially, the [2 + 2] barrier is five times smaller than literature values. Future work will expand on more dicationic metal oxides and explore the factors that favor the three types of C−H activation mechanisms.

■ ASSOCIATED CONTENT

Ⓢ Supporting Information

The Supporting Information is available free of charge at https://pubs.acs.org/doi/10.1021/acs.inorgchem.1c01447.

> Spectroscopic and wavefunction information; composition of the spin−orbit states; optimal geometries for all the reaction intermediates and TSs; harmonic vibrational frequencies (cm^{-1}); optimal geometries and harmonic vibrational frequencies (cm^{-1}) for the reactant, TS, and product for $(NH_3)_4NiO^{2+}$ + CH$_4$ (spin multiplicity = 3); ZPE-corrected and free energy barriers corresponding to the values of Table S3; and geometries and energetics of the CH$_3$−OH recombination step for both [2 + 2] and radical mechanisms (PDF)

■ AUTHOR INFORMATION

Corresponding Author

Evangelos Miliordos − *Department of Chemistry and Biochemistry, Auburn University, Auburn, Alabama 36849-5312, United States;* ⓞ orcid.org/0000-0003-3471-7133; Email: emiliord@auburn.edu

Author

Shahriar N. Khan − *Department of Chemistry and Biochemistry, Auburn University, Auburn, Alabama 36849-5312, United States;* ⓞ orcid.org/0000-0002-8913-8430

Complete contact information is available at:
https://pubs.acs.org/10.1021/acs.inorgchem.1c01447

Notes

The authors declare no competing financial interest.

■ REFERENCES

(1) Schröder, D.; Schwarz, H. C-H and C-C Bond Activation by Bare Transition-Metal Oxide Cations in the Gas Phase. *Angew. Chem., Int. Ed.* **1995**, *34*, 1973−1995.

(2) Yoshizawa, K. Theoretical study on kinetic isotope effects in the C−H bond activation of alkanes by iron-oxo complexes. *Coord. Chem. Rev.* **2002**, *226*, 251−259.

(3) Gunay, A.; Theopold, K. H. C−H Bond Activations by Metal Oxo Compounds. *Chem. Rev.* **2010**, *110*, 1060−1081.

(4) Schwarz, H. Chemistry with Methane: Concepts Rather than Recipes. *Angew. Chem., Int. Ed.* **2011**, *50*, 10096−10115.

(5) Shiota, Y.; Yoshizawa, K. Methane-to-Methanol Conversion by First-Row Transition-Metal Oxide Ions: ScO$^+$, TiO$^+$, VO$^+$, CrO$^+$,

MnO⁺, FeO⁺, CoO⁺, NiO⁺, and CuO⁺. *J. Am. Chem. Soc.* **2000**, *122*, 12317−12326.

(6) Xu, X.; Faglioni, F.; Goddard, W. A. Methane Activation by Transition-Metal Oxides, MO_x (M = Cr, Mo, W; x = 1, 2, 3). *J. Phys. Chem. A* **2002**, *106*, 7171−7176.

(7) Yoshizawa, K.; Shiota, Y.; Yamabe, T. Methane−Methanol Conversion by MnO⁺, FeO⁺, and CoO⁺: A Theoretical Study of Catalytic Selectivity. *J. Am. Chem. Soc.* **1998**, *120*, 564−572.

(8) Schroeder, D.; Fiedler, A.; Hrusak, J.; Schwarz, H. Experimental and theoretical studies toward a characterization of conceivable intermediates involved in the gas-phase oxidation of methane by bare FeO⁺. Generation of four distinguishable [Fe,C,H₄,O]⁺ isomers. *J. Am. Chem. Soc.* **1992**, *114*, 1215−1222.

(9) Yoshizawa, K.; Shiota, Y.; Yamabe, T. Abstraction of the Hydrogen Atom of Methane by Iron−Oxo Species: The Concerted Reaction Path Is Energetically More Favorable. *Organometallics* **1998**, *17*, 2825−2831.

(10) Wang, Y.; Sun, X.; Zhang, J.; Li, J. A Theoretical Study on Methane C−H Bond Activation by Bare [FeO]⁺/⁰/⁻. *J. Phys. Chem. A* **2017**, *121*, 3501−3514.

(11) Chen, Y.-M.; Clemmer, D. E.; Armentrout, P. B. Conversion of CH₄ to CH₃OH: Reactions of CoO⁺ with CH₄ and D₂, Co⁺ with CH₃OD and D₂O, and Co⁺(CH₃OD) with Xe. *J. Am. Chem. Soc.* **1994**, *116*, 7815−7826.

(12) Su, Z.; Qin, S.; Tang, D.; Yang, H.; Hu, C. Theoretical study on the reaction of methane and zinc oxide in gas phase. *J. Mol. Struct.* **2006**, *778*, 41−48.

(13) Fu, G.; Xu, X.; Lu, X.; Wan, H. Mechanisms of Methane Activation and Transformation on Molybdenum Oxide Based Catalysts. *J. Am. Chem. Soc.* **2005**, *127*, 3989−3996.

(14) Gao, C.; Yang, H.-Q.; Xu, J.; Qin, S.; Hu, C. W. Theoretical study on the gas-phase reaction mechanism between rhodium monoxide and methane for methanol production. *J. Comput. Chem.* **2010**, *31*, 938−53.

(15) Broclawik, E.; Yamauchi, R.; Endou, A.; Kubo, M.; Miyamoto, A. Density functional study on the activation of methane over Pd₂, PdO, and Pd₂O clusters. *Int. J. Quantum Chem.* **1997**, *61*, 673−682.

(16) Gani, T. Z. H.; Kulik, H. J. Understanding and Breaking Scaling Relations in Single-Site Catalysis: Methane to Methanol Conversion by Fe^{IV}=O. *ACS Catal.* **2018**, *8*, 975−986.

(17) Nandy, A.; Zhu, J.; Janet, J. P.; Duan, C.; Getman, R. B.; Kulik, H. J. Machine Learning Accelerates the Discovery of Design Rules and Exceptions in Stable Metal-Oxo Intermediate Formation. *ACS Catal.* **2019**, *9*, 8243−8255.

(18) Kirkland, J. K.; Khan, S. N.; Casale, B.; Miliordos, E.; Vogiatzis, K. D. Ligand field effects on the ground and excited states of reactive FeO^{2+} species. *Phys. Chem. Chem. Phys.* **2018**, *20*, 28786−28795.

(19) Jackson, B. A.; Miliordos, E. Weak-field ligands enable inert early transition metal oxides to convert methane to methanol: the case of ZrO. *Phys. Chem. Chem. Phys.* **2020**, *22*, 6606−6618.

(20) Claveau, E. E.; Miliordos, E. Quantum chemical calculations on NbO and its reaction with methane: ground and excited electronic states. *Phys. Chem. Chem. Phys.* **2019**, *21*, 26324−26332.

(21) Ariyarathna, I. R.; Miliordos, E. Ab initio investigation of the ground and excited states of $MoO^{+,2+,-}$ and their catalytic strength on water activation. *Phys. Chem. Chem. Phys.* **2018**, *20*, 12278−12287.

(22) Ariyarathna, I. R.; Almeida, N. M. S.; Miliordos, E. Ab initio investigation of the ground and excited states of $RuO^{+,0,-}$ and their reaction with water. *Phys. Chem. Chem. Phys.* **2020**, *22*, 16072−16079.

(23) Almeida, N. M. S.; Ariyarathna, I. R.; Miliordos, E. O−H and C−H Bond Activations of Water and Methane by RuO^{2+} and $(NH_3)RuO^{2+}$: Ground and Excited States. *J. Phys. Chem. A* **2019**, *123*, 9336−9344.

(24) Khan, S. N.; Miliordos, E. Methane to Methanol Conversion Facilitated by Transition-Metal Methyl and Methoxy Units: The Cases of FeCH₃⁺ and FeOCH₃⁺. *J. Phys. Chem. A* **2019**, *123*, 5590−5599.

(25) Shimoyama, Y.; Kojima, T. Metal-Oxyl Species and Their Possible Roles in Chemical Oxidations. *Inorg. Chem.* **2019**, *58*, 9517−9542.

(26) Claveau, E.; Miliordos, E. Electronic Structure of the dicationic first row transition metal oxides. *Phys. Chem. Chem. Phys.* **2021**, *23*, 21172.

(27) Gray, H. B.; Winkler, J. R. Living with Oxygen. *Acc. Chem. Res.* **2018**, *51*, 1850−1857.

(28) Wang, B.; Lee, Y.-M.; Tcho, W.-Y.; Tussupbayev, S.; Kim, S.-T.; Kim, Y.; Seo, M. S.; Cho, K.-B.; Dede, Y.; Keegan, B. C.; et al. Synthesis and reactivity of a mononuclear non-haem cobalt(IV)-oxo complex. *Nat. Commun.* **2017**, *8*, 14839.

(29) Kojima, T.; Nakayama, K.; Ikemura, K.; Ogura, T.; Fukuzumi, S. Formation of a Ruthenium(IV)-Oxo Complex by Electron-Transfer Oxidation of a Coordinatively Saturated Ruthenium(II) Complex and Detection of Oxygen-Rebound Intermediates in C-H Bond Oxygenation. *J. Am. Chem. Soc.* **2011**, *133*, 11692−11700.

(30) Ray, K.; Heims, F.; Pfaff, F. F. Terminal Oxo and Imido Transition-Metal Complexes of Groups 9-11. *Eur. J. Inorg. Chem.* **2013**, *2013*, 3784−3807.

(31) Mains, G. J.; White, J. M. All-electron and relativistic effective core potential study of rhodium compounds. *J. Phys. Chem.* **1991**, *95*, 112−118.

(32) Siegbahn, P. E. M. A comparison of the bonding in the second-row transition-metal oxides and carbenes. *Chem. Phys. Lett.* **1993**, *201*, 15−23.

(33) Stevens, F.; Van Speybroeck, V.; Carmichael, I.; Callens, F.; Waroquier, M. The Rh-ligand bond: RhX (X=C, N, O, F, P and Cl) molecules. *Chem. Phys. Lett.* **2006**, *421*, 281−286.

(34) Song, P.; Guan, W.; Yao, C.; Su, Z. M.; Wu, Z. J.; Feng, J. D.; Yan, L. K. Electronic structures of 4d transition metal monoxides by density functional theory. *Theor. Chem. Acc.* **2007**, *117*, 407−415.

(35) Suo, B.; Han, H.; Lei, Y.; Zhai, G.; Wang, Y.; Wen, Z. Potential energy curves and interpretation of electronic spectrum of the rhodium monoxide. *J. Chem. Phys.* **2009**, *130*, 094304.

(36) Beltrán, M. R.; Buendía Zamudio, F.; Chauhan, V.; Sen, P.; Wang, H.; Ko, Y. J.; Bowen, K. Ab initio and anion photoelectron studies of Rhn (n = 1 − 9) clusters. *Eur. Phys. J. D* **2013**, *67*, 63.

(37) Li, X.; Wang, L.-S. The chemical bonding and electronic structure of RhC, RhN, and RhO by anion photoelectron spectroscopy. *J. Chem. Phys.* **1998**, *109*, 5264−5268.

(38) Citra, A.; Andrews, L. Reactions of Laser-Ablated Rhodium Atoms with O₂. Infrared Spectra and DFT Calculations for RhO, ORhO, (O₂)RhO₂, Rh₂O₂, Rh(O₂) and (O₂)Rh(O₂) in Solid Argon. *J. Phys. Chem. A* **1999**, *103*, 4845−4854.

(39) Heuff, R. F.; Balfour, W. J.; Adam, A. G. A Laser-Induced Fluorescence Study of the Visible Spectrum of Rhodium Monoxide. *J. Mol. Spectrosc.* **2002**, *216*, 136−150.

(40) Jensen, R. H.; Fougère, S. G.; Balfour, W. J. Laser-induced fluorescence and dispersed fluorescence spectroscopy, isotopic studies, and lifetime measurements for rhodium monoxide. *Chem. Phys. Lett.* **2003**, *370*, 106−111.

(41) Gengler, J.; Ma, T.; Adam, A. G.; Steimle, T. C. A molecular beam optical Stark study of the [15.8] and [16.0] Π1/22-XΣ−4 (0,0) band systems of rhodium monoxide, RhO. *J. Chem. Phys.* **2007**, *126*, 134304.

(42) Carsch, K. M.; Cundari, T. R. DFT modeling of a methane-to-methanol catalytic cycle via Group 6 organometallics: The role of metal in determining the mode of C-H activation. *Comput. Theor. Chem.* **2012**, *980*, 133−137.

(43) Dunning, T. H. Gaussian basis sets for use in correlated molecular calculations. I. The atoms boron through neon and hydrogen. *J. Chem. Phys.* **1989**, *90*, 1007−1023.

(44) Kendall, R. A.; Dunning, T. H.; Harrison, R. J. Electron affinities of the first-row atoms revisited. Systematic basis sets and wave functions. *J. Chem. Phys.* **1992**, *96*, 6796−6806.

(45) Peterson, K. A.; Figgen, D.; Dolg, M.; Stoll, H. Energy-consistent relativistic pseudopotentials and correlation consistent basis sets for the 4d elements Y-Pd. *J. Chem. Phys.* **2007**, *126*, 124101.

(46) Werner, H.-J.; Knizia, G.; Manby, F. R.; Schütz, M.; Celani, P.; Györffy, W.; Kats, D.; Korona, T.; Lindh, R.; Mitrushenkov, A.; Rauhut, G.; Shamasundar, K. R.; Adler, T. B.; Amos, R. D.; Bernhardsson, A.; Berning, A.; Cooper, D. L.; Deegan, M. J. O.; Dobbyn, A. J.; Eckert, F.; Goll, E.; Hampel, C.; Hesselmann, A.; Hetzer, G.; Hrenar, T.; Jansen, G.; Köppl, C.; Liu, Y.; Lloyd, A. W.; Mata, R. A.; May, A. J.; McNicholas, S. J.; Meyer, W.; Mura, M. E.; Nicklaß, A.; O'Neill, D. P.; Palmieri, P.; Peng, D.; Pflüger, K.; Pitzer, R.; Reiher, M.; Shiozaki, T.; Stoll, H.; Stone, A. J.; Tarroni, R.; Thorsteinsson, T.; Wang, M. *MOLPRO*, 2015; p 1.

(47) Yu, H. S.; He, X.; Li, S. L.; Truhlar, D. G. MN15: A Kohn-Sham global-hybrid exchange-correlation density functional with broad accuracy for multi-reference and single-reference systems and noncovalent interactions. *Chem. Sci.* **2016**, *7*, 5032−5051.

(48) Frisch, M. J.; Schlegel, H. B.; Scuseria, G. E.; Robb, M. A.; Cheeseman, J. R.; Scalmani, G.; Barone, V.; Petersson, G. A.; Nakatsuji, H.; Li, X.; Caricato, M.; Marenich, A. V.; Bloino, J.; Janesko, B. G.; Gomperts, R.; Mennucci, B.; Hratchian, H. P.; Ortiz, J. V.; Izmaylov, A. F.; Sonnenberg, J. L.; Williams-Young, D.; Ding, F.; Lipparini, F.; Egidi, F.; Goings, J.; Peng, B.; Petrone, A.; Henderson, T.; Ranasinghe, D.; Zakrzewski, V. G.; Gao, J.; Rega, N.; Zheng, G.; Liang, W.; Hada, M.; Ehara, M.; Toyota, K.; Fukuda, R.; Hasegawa, J.; Ishida, M.; Nakajima, T.; Honda, Y.; Kitao, O.; Nakai, H.; Vreven, T.; Throssell, K.; Montgomery, J. A., Jr.; Peralta, J. E.; Ogliaro, F.; Bearpark, M. J.; Heyd, J. J.; Brothers, E. N.; Kudin, K. N.; Staroverov, V. N.; Keith, T. A.; Kobayashi, R.; Normand, J.; Raghavachari, K.; Rendell, A. P.; Burant, J. C.; Iyengar, S. S.; Tomasi, J.; Cossi, M.; Millam, J. M.; Klene, M.; Adamo, C.; Cammi, R.; Ochterski, J. W.; Martin, R. L.; Morokuma, K.; Farkas, O.; Foresman, J. B.; Fox, D. J. *Gaussian 16*; Gaussian, Inc.: Wallingford CT, 2016.

(49) Rasheed, W.; Draksharapu, A.; Banerjee, S.; Young, V. G., Jr; Fan, R.; Guo, Y.; Ozerov, M.; Nehrkorn, J.; Krzystek, J.; Telser, J.; et al. Crystallographic Evidence for a Sterically Induced Ferryl Tilt in a Non-Heme Oxoiron(IV) Complex that Makes it a Better Oxidant. *Angew. Chem., Int. Ed.* **2018**, *57*, 9387−9391.

(50) Kulkarni, A. R.; Zhao, Z.-J.; Siahrostami, S.; Nørskov, J. K.; Studt, F. Cation-exchanged zeolites for the selective oxidation of methane to methanol. *Catal. Sci. Technol.* **2018**, *8*, 114−123.

(51) Ravi, M.; Ranocchiari, M.; van Bokhoven, J. A. The Direct Catalytic Oxidation of Methane to Methanol-A Critical Assessment. *Angew. Chem., Int. Ed.* **2017**, *56*, 16464−16483.

(52) Schwach, P.; Pan, X.; Bao, X. Direct Conversion of Methane to Value-Added Chemicals over Heterogeneous Catalysts: Challenges and Prospects. *Chem. Rev.* **2017**, *117*, 8497−8520.

(53) Zakaria, Z.; Kamarudin, S. K. Direct conversion technologies of methane to methanol: An overview. *Renewable Sustainable Energy Rev.* **2016**, *65*, 250−261.

(54) Sader, S.; Miliordos, E. Methane to Methanol Conversion Facilitated by Anionic Transition Metal Centers: The Case of Fe, Ni, Pd, and Pt. *J. Phys. Chem. A* **2021**, *125*, 2364−2373.

(55) Ariyarathna, I. R.; Miliordos, E. Radical abstraction vs. oxidative addition mechanisms for the activation of the S-H, O-H, and C-H bonds using early transition metal oxides. *Phys. Chem. Chem. Phys.* **2021**, *23*, 1437−1442.

Appendix B

Supporting Materials for Chapter 3

- **S. N. Khan**, and E. Miliordos, *J. Phys. Chem. A.* **2019,** *123*, 5590-5599.

Methane to Methanol Conversion Facilitated by Transition-Metal Methyl and Methoxy Units: The Cases of $FeCH_3^+$ and $FeOCH_3^+$

Shahriar N. Khan[ID] and Evangelos Miliordos*[ID]

Department of Chemistry and Biochemistry, Auburn University, Auburn, Alabama 36849-5312, United States

S *Supporting Information*

ABSTRACT: The conversion of methane to methanol (MTM) catalyzed by $FeOCH_3^+$ and $FeCH_3^+$ is investigated by means of multireference configuration interaction (MRCI), single-reference coupled clusters (CC), and density functional theory (DFT) approaches. Our dual purpose is the assessment of the applied methodologies and the performance of the proposed catalytic cycle, which involves both of the titled units. The investigated cycle aims to bypass the limitations of metal-oxide catalysts and offers an alternative promising method for efficient MTM transformation. From the technical viewpoint, we found that generally accurate electron correlation treatment is more important than accurately calculated geometries. The combination of optimal DFT geometries with MRCI and CC energetics provides a good compromise between accuracy and efficiency, although there are cases where multireference calculations must be used to obtain correct structures.
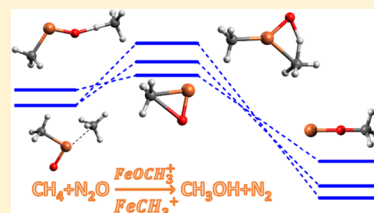
I. INTRODUCTION

Despite the considerable progress in the improvement of existing or development of new green processes over the past decades, fossil fuels continue to play a major role in the global economy and technology. Besides their high energy content, fossil fuels are hydrocarbon cocktails, which provide low-cost feedstock for the production of various platform chemicals. Methane, the smallest hydrocarbon, is abundant in natural gas, whereas its availability has recently increased because of the growth of hydraulic fracturing (fracking). From a different angle, methane is the second most abundant greenhouse gas behind CO_2 but is more potent in trapping heat having a detrimental impact in the atmosphere.[1,2] Both economic and environmental reasons have accelerated the attempts to upgrade methane by introducing functional groups with more efficient methods.

Industrially, the conversion of methane to commodity chemicals and liquid fuels goes through the synthetic gas route. It is first decomposed to $CO + H_2$ (syngas), which is then exposed to harsh conditions (15−40 atm pressure and 700−1000 °C temperature), to make methanol.[3,4] An overview of available direct methane to methanol (MTM) conversion techniques avoiding the syngas path has been given recently.[5,6] These involve gas-phase and solution-phase homogeneous catalysis, heterogeneous catalysis, photocatalysis, biocatalysts (enzymes),[7] plasma technologies, frustrated Lewis-pairs,[8,9] MOFs,[10−12] and others. Their drawbacks and limitations are discussed in ref 13. Despite the encouraging progress (see for example refs 14, 15), this task is extremely challenging,[3,16,17] and no method with reasonable yield has been discovered.[5,13,18−24]

Transition-metal oxides are the most common family of homogeneous and heterogeneous catalysts used for MTM conversion. Among them, iron-oxo complexes have attracted considerable attention by both experimental and theoretical research groups in an attempt to imitate bioenzymes selected and optimized by nature.[25−31] The activation of the C−H bond occurs in two ways, creating radical intermediates or going through a [2 + 2] addition.[32] The exact route depends on the catalytic system, and small subtle changes of the metal or ligand can switch the mechanism.[32] Two factors affect the catalytic activity of both mechanisms: (1) the activation energy barriers needed to overcome and (2) the selective activation of the C−H bonds of methane and not the more reactive ones of the produced methanol, which leads to over-oxidated products.[5,6,13,30] Recently, we investigated the role of ligands in the radical mecahnism and concluded that weak ligand field molecules in the first coordination sphere of the metal enhance the catalytic activity.[25]

More recently, Nørskov and co-workers employed a simple kinetic model to prove that when the radical mechanism of metal-oxides occurs, there is a fundamental trade-off between efficiency and selectivity for the MTM conversion.[13] Higher C−H activation efficiency translates to smaller selectivity. The authors suggested the use of collectors or solvents (such as water) to keep methanol away from the catalytic centers or the employment of different catalytic routes. The issue of radical-like mechanisms is that the relative activation barriers for methane and methanol are nearly catalyst-independent.[13] The reason is that the OH group of methanol does not approach the catalytic site, but only a hydrogen atom "talks" to the catalyst in a $M=O\cdots H-CH_2X$ (X = H or OH) fashion. Therefore, the electronic factors, which weaken the C−H bond of methanol, prevail.

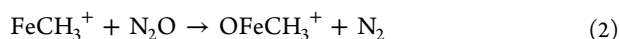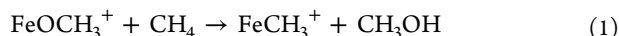The alternative of optimizing the [2 + 2] mechanism over the radical one seems an arduous task because of the sensitivity to "subtle changes" of metals and ligands.[32] Herein, we assess a completely different route avoiding the terminal metal–oxygen bond as the catalytic site. Inspired by the pioneering work of Najafian and Cundari,[33] we investigate the mediation of metal-methoxy units. These authors focused on the C–H activation step for first-row transition metals, but presently we explore the complete catalytic cycle. A mechanism facilitated by metal-methoxides was recently identified in a very efficient MTM conversion using copper-doped zeolites and water as an oxidant to reload oxygen to the catalyst.[15] The latter reaction is quite endothermic, and thus we decided to use a more potent oxidant, such as N_2O, which is often used in similar gas-phase and catalytic reactions.[34−36] Our overall catalytic cycle is based on the following three main steps

$$FeOCH_3^+ + CH_4 \rightarrow FeCH_3^+ + CH_3OH \qquad (1)$$

$$FeCH_3^+ + N_2O \rightarrow OFeCH_3^+ + N_2 \qquad (2)$$

$$OFeCH_3^+ \rightarrow FeOCH_3^+ \qquad (3)$$

The catalytic cycle can be initiated from step (2) and, thus, the catalyst can contain the more stable and easier to synthesize iron–methyl unit.[37] Below we present our results on the three steps for both the ground and low-lying excited electronic states. We also considered some side reaction pathways leading to unwanted byproducts. Throughout our analysis, we discuss the performance of the employed electronic structure methods, and we finally suggest an optimal algorithm for future calculations.

In Section II, we discuss further the mechanistic aspects of the proposed catalytic cycle. In Section III, we describe our methodologies, which include density functional theory (DFT), multireference, and coupled-cluster approaches. In Section IV, we analyze our results, and Section V summarizes our findings.

II. MECHANISTIC CONSIDERATIONS

At the first step of the cycle (see eq 1), one C–H bond of methane cleaves. The H atom binds to methoxide producing methanol, whereas the remaining methyl group coordinates to iron. This step has been studied theoretically with DFT by Najafian and Cundari for uncharged catalysts of the L_nMOCH_3 type, where M = Ti–Cu, and L_n is some tridentate ligand.[33] The second step is the oxidation of the metal center by N_2O forming a FeO bond, the terminal oxygen atom of which migrates between iron and methyl in the third step.

Figure 1 depicts the considered catalytic cycle with solid lines. The dashed lines represent some alternative unfavorable routes. Specifically, the $FeCH_3^+$ and $OFeCH_3^+$ intermediates can react with a second methane activating another C–H bond. The first path leads solely to side products. On the other hand, $OFeCH_3^+$ is expected to act as the commonly used metal-oxides leading potentially to methanol but suffering from the issues described in the introduction. The novelty of our proposed mechanism requires the elimination of the latter pathway and the deactivation of the iron-oxo chemical activity through the fast unimolecular transformation of $OFeCH_3^+$ to $FeOCH_3^+$. In agreement with our results, Fiedler et al. identified the latter structure as the global minimum.[38]

An exemplary energy landscape of the proposed catalytic cycle is shown in Figure 2. The transition states TS1, TS2, and TS3 correspond to reaction steps (1)−(3). TS4, TS5, and TS6 pertain to the initial step of the unfavorable paths of Figure 1

$$FeCH_3^+ + CH_4 \rightarrow (H_3C)_2FeH^+ \qquad (4)$$

$$OFeCH_3^+ + CH_4 \rightarrow (H_3C)_2FeOH^+ \qquad (5)$$

$$OFeCH_3^+ + CH_4 \rightarrow H_3C \cdots HOFeCH_3^+ \qquad (6)$$

The energies for these structures and the products associated with them are drawn with dashed lines in Figure 2. For consistency, the energy of the "observer" molecules is added at every step.

Ideally, TS4 must be much higher in energy than TS2 and both TS5 and TS6 much higher than TS3. It should be mentioned that both $FeCH_3^+$ and $OFeCH_3^+$ can, in principle, react with existing methanol, instead of CH_4 (steps (4)−(6)), and activate one of its C–H bonds. The results will be either a poisoned catalyst or over-oxidation products. As opposed to the radical mechanism, the proposed mechanism necessitates the close proximity of the substrate to the catalytic site. The use of molecular catalysts with proper ligands that exclude methanol from the active site can remedy this issue. The ligand effects will be explored in the near future.

Another important aspect in the theoretical study of catalytic cycles is the spin crossovers occurring along the reaction coordinate of some steps. To account properly the changes of the electronic spin, someone has to consider low-lying electronic states as well. To this end, we constructed potential energy profiles for different spin multiplicities along the reaction coordinate of each step.

III. COMPUTATIONAL DETAILS

Vogiatzis et al. recently published a critical review on the proper methodologies needed to describe properly the complex electronic structure of transition-metal compounds with a focus on catalytic applications.[39] The authors emphasized the necessity of highly accurate approaches, such as multireference methodologies. Another recent work of Nakatani and Hada (on the similar reaction $FeO^+ + CH_4$) demonstrated that static-correlation-only multireference (complete active space self-consistent field or CASSCF) calculations can be quite misleading even if a large active space is used.[40] On the other hand, density functional theory (DFT) should be subjected to careful evaluation of its ability to correctly grasp the required physical phenomena.[39,41,42] Therefore, three different types of calculations were performed to shed some additional light: CASSCF and multireference configuration interaction (MRCI), single-reference coupled clusters (CCSD-(T)), and DFT (unrestricted Kohn–Sham formulation) calculations. The MN15 functional is chosen in the latter
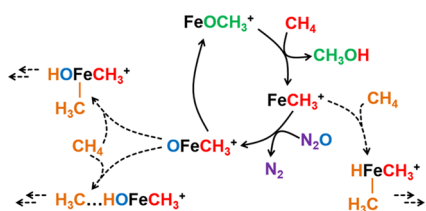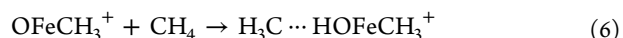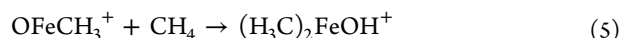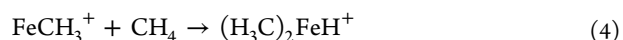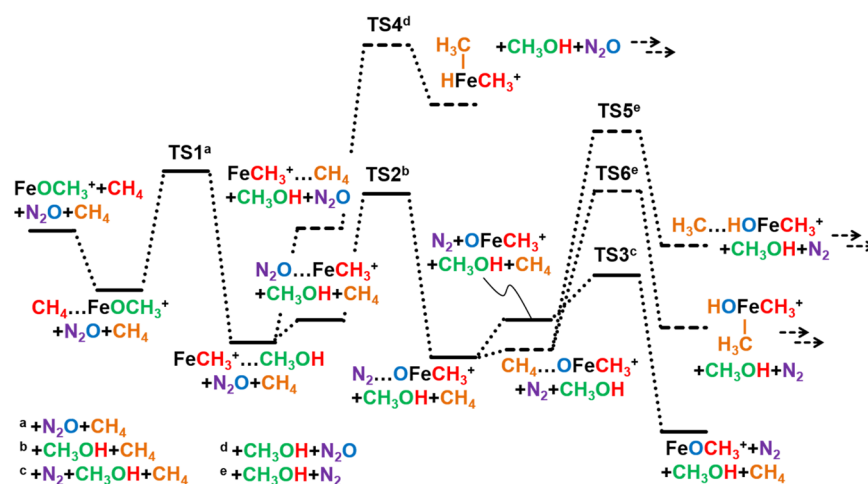

Figure 1. Solid lines show the proposed catalytic cycle, whereas dashed lines correspond to side routes, which need to be suppressed. Arrows represent all possible subsequent reaction steps.

Figure 2. Ideal energy landscape for the proposed catalytic cycle. The A⋯B notation indicates the interacting complex of molecules A and B. Arrows represent all possible subsequent reaction steps.

case since it shows good performance for transition metals and noncovalent interactions.[43]

The correlation consistent basis sets of triple-ζ (TZ) quality were employed (cc-pVTZ).[44,45] For the oxygen centers, we added a series of diffuse functions (aug-cc-pVTZ)[46] to account for the ionic nature of the iron−oxygen bonds.[47−51] In some computationally demanding cases, we used double-ζ (DZ) quality.

Optimized structures were obtained at the CASSCF/TZ, DFT/MN15/TZ, and CCSD(T)/DZ levels of theory. All of them are listed in the Supporting Information (SI). For reaction step (3), we performed optimizations at the MRCI, MRCI + Q, CASPT2, CCSD(T), and MP2 levels as well with the TZ set. Comparison of the geometries for reactants, transition state, and products is made for all of these levels of theory for step (3). This step is the unimolecular transformation of OFeCH$_3^+$ to FeOCH$_3^+$, and is selected, because it allows the direct assessment on the electronic structure description avoiding the contribution of intermolecular electrostatic and dispersion interactions. Overall, DFT/MN15/TZ gives accurate geometries but provides less accurate energetics. This is an indication that the equilibrium region of each stationary geometry (except TS2; see below) is described satisfactorily at DFT/MN15, but the energy differences among the different equilibria are less satisfactory. Thus, the calculated harmonic vibrational frequencies were obtained only at the DFT/MN15/TZ level, which is computationally less demanding. One imaginary frequency was found for every transition state and only real ones for all intermediates. The normal modes pertaining to the imaginary frequency for these first-order transition states validate that TS1 through TS6 connects the intermediates shown in Figure 2.

The multireference character of the wavefunction for all structures was estimated by the amplitude of the dominant MRCI electronic configuration (C_0) and the T1 diagnostic at the CCSD level; see SI. The wavefunction of the ground quintet state was found fairly single reference in all cases, $0.86 < C_0 < 0.99$. The T1 diagnostic ranges from 0.026 to 0.073 and although in some cases is larger than the limit of 0.05 suggested for transition-metal compounds in the literature,[52] the CCSD(T) results are consistent with the MRCI and DFT/MN15 ones.

The choice of the CASSCF active space was very challenging. Full valence space is prohibitively large, and thus a wise selection had to be made. The CASSCF active orbitals were chosen to include the valence space of iron and the orbitals relative to the bonds cleaved or formed, i.e., the σ and σ^* orbitals of the inert C−H bonds were excluded. Special attention was paid to include the same number of active orbitals and electrons at every single step. In all cases, we allocated 16 electrons in 13 orbitals. All valence electrons were correlated at the subsequent multireference configuration interaction singles and doubles (MRCI) and second-order perturbation theory (RS2C approach as implemented in the MOLPRO)[53] calculations. Excited state calculations were based on state-average CASSCF (SA-CASSCF) reference wavefunctions. The DFT calculations were done with the Gaussian 16 suite of codes[54] and all other calculations with MOLPRO2015.[53]

Finally, the energy profiles along the reaction coordinate of each step were constructed at the MRCI + Q/TZ level using the DFT/MN15/TZ geometries of an intrinsic reaction coordinate (IRC) calculation with Gaussian 16. The Davidson correction (+Q) was implemented to reduce the size-extensivity error.

IV. RESULTS AND DISCUSSION

Motivated by the work of Najafian and Cundari, we initially constructed the energy landscape for neutral FeOCH$_3$ by means of DFT/B3LYP/TZ. For all species, we found that $S = 3/2$ provides always the lowest energy spin state. The energy plot is shown with blue lines in Figure S1 of SI. We were not able to locate TS2 in this case, but the best structure we obtained is much higher than TS4, which means that the attachment of a second methane molecule to iron is preferred over the oxidation of iron. Additionally, TS5 and TS6 are lower in energy than TS3 leading to unfavorable paths, as described in the previous section. Overall, steps (2) and (3) deviate appreciably from the ideal energy diagram of Figure 2. We then switched to FeOCH$_3^+$, the energy diagram of which is closer to that of Figure 2 (compare it with Figure S1 of the SI).

The open-shell species present in the catalytic cycle are FeOCH$_3^+$, FeCH$_3^+$, OFeCH$_3^+$, (CH$_3$)$_2$FeH$^+$, (CH$_3$)$_2$FeOH$^+$, and CH$_3$FeOH$^+$⋯CH$_3$. Coordinated methoxy, methyl, and hydroxyl groups can be seen as either anionic CH$_3$O$^-$, CH$_3^-$,
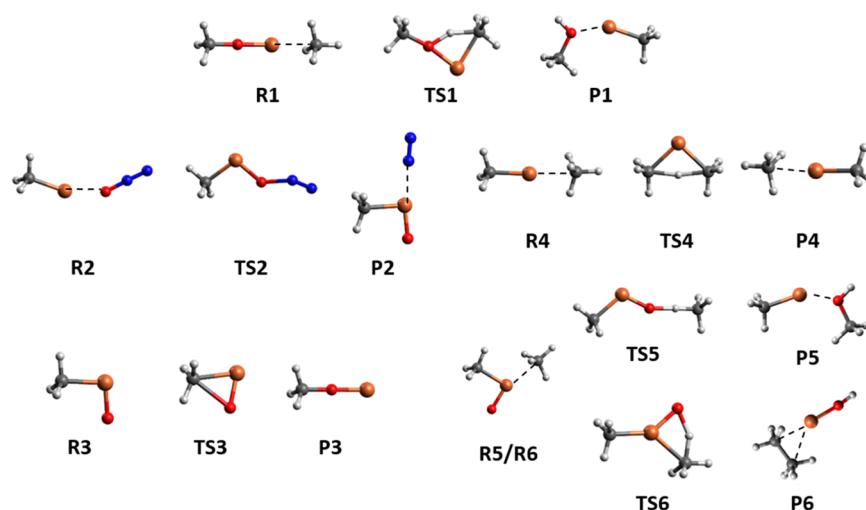
Figure 3. DFT/MN15 optimal structures of all intermediates for steps (1)−(6). R, P, and TS correspond to reactants, products, and transition states, respectively.

Table 1. Potential Energy Barrier ($\Delta E_e^{\ddagger}$ in kcal/mol), Reaction Potential Energy (ΔE_e in kcal/mol), Fe−O (R_{FeO}) and Fe−C (R_{FeC}) Bond Lengths (in Å) for the Reactants (R3), Products (P3), and Transition State (TS3) of Step (3) with Different Methodologies

quantity	MRCI[a]	MRCI + Q[a]	CCSD(T)[a]	CCSD(T)[b]	CASPT2[a]	MP2[a]	MN15[a]
				OFeCH$_3^+$ (R3)			
R_{FeO}	1.618	1.616	1.608	1.621	1.619	1.518	1.579
R_{FeC}	2.012	1.991	1.967	1.975	1.988	1.944	1.936
				TS3			
R_{FeO}	1.660	1.654	1.642	1.653	1.639	1.534	1.622
R_{FeC}	2.157	2.148	2.091	2.103	2.158	2.078	2.063
$\Delta E_e^{\ddagger}$	8.7	9.5	9.0	8.7	15.8	12.9	5.3
				FeOCH$_3^+$ (P3)			
R_{FeO}	1.707	1.704	1.699	1.706	1.679	1.697	1.685
ΔE_e	−42.7	−38.0	−46.4	−44.7	−25.7	−64.0	−54.6

[a]Basis set: cc-pVTZ (Fe, C, H), aug-cc-pVTZ (O). [b]Basis set: cc-pVDZ (Fe, C, H), aug-cc-pVDZ (O).

OH$^-$, or radical CH$_3$O$^\bullet$, CH$_3^\bullet$, OH$^\bullet$ moieties, which couple to an electron from iron. Similarly, a terminal FeO bond can be seen as either Fe^{2+}O^{2-} or Fe=O. Both pictures commit two electrons from the iron center. Based on these observations, iron should appear as in situ Fe^{2+}(d^6; ^{5}D) in the FeOCH$_3^+$ and FeCH$_3^+$ species and as Fe^{4+}(d^4; ^{5}D) in OFeCH$_3^+$, (CH$_3$)$_2$FeH$^+$, and (CH$_3$)$_2$FeOH$^+$. Therefore, all intermediates are expected to have a ground state of quintet spin multiplicity. Finally, iron in CH$_3$FeOH$^+$ has a Fe^{3+}(d^5; ^{6}S) character resulting in a sextet state for CH$_3$FeOH$^+$. This combined with CH$_3$ radical (^{2}A$_2''$) can give an overall quintet or septet spin multiplicity. Our CASSCF calculations validate the predicted electronic structure, and excited states calculations confirmed that the quintet state is the lowest one at every step.

Our discussion proceeds with the description of each step separately, and at the end, we combine all findings together to draw the final energy landscape. All intermediate and transition-state structures are collected in Figure 3. We first analyze our results on step (3), since we did a more extensive assessment of different electronic structure methodologies in this case (see Section III).

Step (3): This step involves only one molecule transforming from the metal oxide OFeCH$_3^+$ (R3) to the metal methoxide FeOCH$_3^+$ (P3) via the transition-state TS3 (see Figure 3). Among the different methodologies, the Fe−O and Fe−C

bond lengths were found more sensitive to the treatment of electron correlation. Table 1 lists these bond lengths at MRCI, MRCI + Q, CCSD(T), CASPT2, MP2, and DFT/MN15. The TZ basis set is used always, but both DZ and TZ basis sets were used for CCSD(T).

Moving from MRCI/TZ to MRCI + Q/TZ and to CCSD(T)/TZ, both bonds shorten monotonically. The average decrease is less than 0.01 Å going from MRCI/TZ to MRCI + Q/TZ and ∼0.02 Å from MRCI + Q/TZ to CCSD(T)/TZ. Interestingly, CCSD(T)/DZ agrees better with MRCI + Q/TZ with an average difference of 0.01 Å, the latter predicting longer bonds. MP2/TZ shows some large deviations in some cases of ∼0.1 Å, but CASPT2/TZ agrees very well (within ∼0.01 Å) with both MRCI + Q/TZ and CCSD(T)/TZ. DFT/MN15/TZ showed relatively large average differences from MRCI + Q/TZ and CCSD(T)/TZ of 0.045 and 0.035 Å.

It turns out that these geometrical differences affect minimally (<1 kcal/mol) the energetics. We performed single-point CCSD(T)/TZ calculations employing the optimal geometries of every method. The potential energy barriers ($\Delta E_e^{\ddagger}$) and reaction potential energies (ΔE_e) were found in the range of 8.5 ± 0.5 and −46.6 ± 0.2 kcal/mol, respectively, except for $\Delta E_e^{\ddagger}$ (CCSD(T)/TZ//MP2/TZ), which is 5.5 kcal/mol. On the other hand, both $\Delta E_e^{\ddagger}$ and ΔE_e depend

strongly on the level that the electron correlation is treated. $\Delta E_e^{\ddagger}$ can be as small as 5.3 kcal/mol (MN15/TZ) and as big as 15.8 kcal/mol (CASPT2/TZ). We believe that the value of 9.1 ± 0.4 kcal/mol representing the range for the MRCI/TZ, MRCI + Q/TZ, and CCSD(T)/TZ approaches is more accurate and is in harmony with the CCSD(T)/TZ range when different geometries are employed. The ΔE_e values cover a larger range from -25.7 kcal/mol (CASPT2/TZ) to −64.0 kcal/mol at MP2/TZ. Again, the −40 to −45 kcal/mol values of MRCI/TZ, MRCI + Q/TZ, and CCSD(T)/TZ levels should be considered more accurate. To compromise between accuracy and efficiency, we finally decided to obtain MN15/TZ- and CCSD(T)/DZ-optimized structures and perform single-point CCSD(T)/TZ calculations. This approach gives ΔE_e values of −46.4 and −46.8 kcal/mol when the CCSD(T)/DZ and MN15/TZ geometries are used. This practice is followed for the remaining reaction steps.

The agreement between multireference MRCI/MRCI + Q and single-reference CCSD(T) energetics is better for $\Delta E_e^{\ddagger}$, which relates to R3 and TS3, than ΔE_e, which relates to R3 and P3. Looking at the multireference character of the wavefunctions through the T1-diagnostics of R3, TS3, and P3, we see the order P3 (0.038) < TS3 (0.069) < R3 (0.091). Only P3 is below the threshold of 0.05 suggested in the past for reliable CCSD(T) results.[52] Therefore, we get better agreement for $\Delta E_e^{\ddagger}$, where both related diagnostics are higher than the threshold, than ΔE_e, where one diagnostic is "normal" and one is almost twice larger than the threshold. This suggests either cancelation of errors or that the threshold of 0.05 should be revisited. Looking at the coefficient of the larger electronic configuration in the CI vectors, we observe the following order P3 (0.99) > TS3 (0.89) > R3 (0.88), which is in harmony with the T1-diagnostics. The present T1-diagnostics are the largest among all of our structures (see Table S1 of the SI). Since there is a fair agreement between MRCI/MRCI + Q and CCSD(T) in this case, we believe that our CCSD(T) results are in general quite accurate, and that our conclusions on the catalytic activity are reliable.

The potential energy profiles (PEPs) along the reaction coordinate for this step are shown in Figure 4. The migration
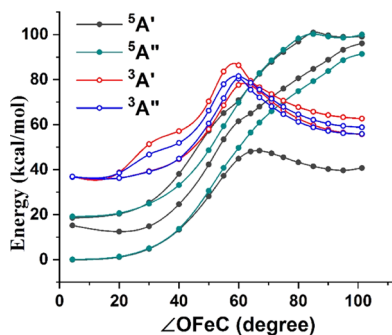
MRCI + Q/TZ calculations for several low-lying electronic states of triplet and quintet spin multiplicity.

$FeOCH_3^+$ is pseudolinear, and, therefore, its $^5A'$ ground state is nearly degenerate with a $^5A''$ state. Recall that iron is best described as $Fe^{2+}(d^6; {}^5D)$. In these two states, there are two unpaired electrons in the two $3d_\pi$ orbitals, one electron in a $d_\sigma-3d_z{}^2$ orbital and three electrons in the two $3d_\delta$ orbitals (see Figure S2 of the SI). The latter configuration makes the two states distinct but nearly degenerate $(3d_{\delta+}{}^23d_{\delta-}{}^1$ and $3d_{\delta+}{}^13d_{\delta-}{}^2)$ resembling a $^5\Delta$ state. The rest three components of $Fe^{2+}(d^6; {}^5D)$ make the next quintet states around ~20 kcal/mol higher. These split in a pseudo $^4\Pi$ and $^4\Sigma^+$ branches.

At the other side, $OFeCH_3^+$ has a $Fe^{4+}(d^4; {}^5D)$ nature, and only one out of these five components dominates. The rest four components are rather unstable sliding readily to the $FeOCH_3^+$ quintets. The reason is that now some d-orbitals participate in the formation of the additional bonds and become unavailable to host "pure-iron" electrons. That is why triplets, where d-electrons pair up, are the first excited states below the unstable quintets. The triplets of the two species are both stable and separated by large energy barriers compared to the ground $^5A'$ state (see Figure 4).

Overall, the quintet ground state is well separated from the excited states, and the barrier from the reactants to the thermodynamically more stable products is minimal.

Step (1): The first step involves the attack of methane to $FeOCH_3^+$ and the release of CH_3OH. The produced form of the catalyst, $FeCH_3^+$, has a very similar electronic structure to $FeOCH_3^+$. In both cases, iron is in a $Fe^{2+}(d^6; {}^5D)$ state. They are both quasi-linear systems, and the ^5D splits into the five pseudo-$^5\Delta$, $^5\Pi$, and $^5\Sigma^+$ states (see step (3)). The optimal geometries of the reactants (R1), transition state (TS1), and products (P1) are shown in Figure 3.

Starting from TS1, we followed the intrinsic reaction coordinate (IRC) along the two directions of the vibrational mode pertaining to the imaginary frequency. The IRC was calculated at the MN15/TZ level of theory, but selected geometries were used to perform MRCI + Q/TZ for the low-lying excited states. Figure 5 depicts the PEPs along this IRC
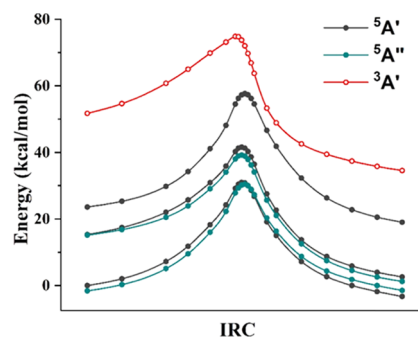

Figure 4. MRCI + Q PEPs as a function of the OFeC angle for step (3). All other geometrical parameters are optimized for every angle at the MN15 level of theory for the ground $^5A'$ state.

Figure 5. MRCI + Q PEPs for several low-lying electronic states along the reaction coordinate of step (1).

of oxygen from iron to the middle of iron and carbon is described by the OFeC angle. This is around 100° for R3 and almost 0° for P3 (see Figure 3). All other parameters are optimized at the MN15/TZ level for every angle, while the C_s symmetry is preserved. Using these geometries we performed

for the five components of $Fe^{2+}(d^6; {}^5D)$ plus the first triplet state. The similarity of the electronic structure of the reactants and products is also supported by the persistence of the near-degeneracy for the pseudo-$^5\Delta$ and $^5\Pi$ components along the IRC.

Step (2): This step involves the reload of the iron center with oxygen and induces the strongest electronic structure variations. The DFT/MN15 search for TS2 converged readily
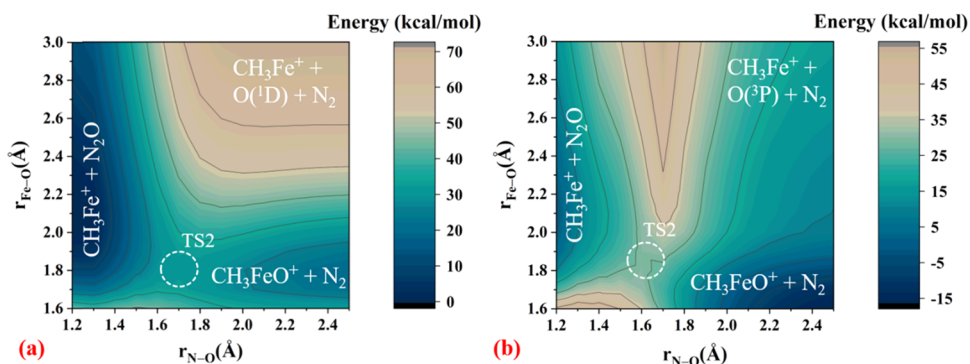
Figure 6. Two-dimensional DFT/MN15 (a) and MRCI + Q (b) PEPs for step (2) as a function of the N−O and Fe−O distances. See text for details.

to that of Figure 3. However, locating TS2 with MRCI or CCSD(T) turned out to be very challenging. The CASSCF electronic wavefunction presented convergence issues, whereas the optimization algorithm was unable to locate TS2. To identify the cause, we started from TS2 of DFT/MN15 and scanned over a wide range of the Fe−O and O−N distances. The two-dimensional PEPs are plotted in Figure 6. Long Fe−O and short O−N distances correspond to the reactants CH_3Fe^+ + ON_2, whereas short Fe−O and long O−N distances to the products CH_3FeO^+ + N_2. The DFT/MN15 distances for TS2 are 1.756 (Fe−O) and 1.631 (N−O) Å.

The 2D-PEPs of Figure 6 for DFT/MN15/TZ and MRCI/TZ are considerably different. When both distances approach the dissociation limit, DFT/MN15 converges to the CH_3Fe^+ ($^5A'$) + O ($\sim^1D$) + N_2 ($^1\Sigma_g^+$) fragments, whereas MRCI goes to the lowest energy fragments CH_3Fe^+ ($^5A'$) + O (^3P) + N_2 ($^1\Sigma_g^+$). The O ($\sim^1D$) notation indicates that the unrestricted DFT/MN15 electronic configuration places two α and two β electrons on oxygen ($2p_z^2 2p_x^1 \overline{2p_y^1}$), which is only one component of the multiconfigurational exact O(^1D) wavefunction. Both fragments create quintet spin potential energy surfaces, but the single-reference nature of DFT is unable to capture the shape at the right top corner of the 2D-PEPs (see Figure 6). Since the geometry is not optimized at each grid point, the PEPs do not lead to the optimal structures of the reactants or the products.

Recently, we studied the oxidation mechanism of ethene by iodosobenzene (C_6H_5IO), and we found that it is the involvement of O(^1D), which facilitates the transfer of oxygen from iodine to the C−C double bond (making epoxides).[55] Specifically, we showed that the closed-shell idobenzene (C_6H_5I) binds to oxygen via a single dative bond with O(^1D), rather than a double bond with O(^3P), in the following manner $C_6H_5I:\rightarrow O(^1D; 2p_z^0 2p_x^2 2p_y^2)$. At the transition state, the π-electrons of ethene compete with those of iodine to occupy the $2p_z^0$ orbital, but finally ethene wins since the $2p_x^2$ electrons of O(^1D) attack to its empty π^* orbital making a second bond.

To examine if this is the case here as well, we constructed potential energy curves for several electronic states along two slices of the 2D-PEPs of Figure 6: first, we kept fixed the Fe−O distance at 2.8 Å and varied the N−O distance (Figure 7), and second we kept the N−O distance fixed at 2.4 Å and varied the Fe−O distance (Figure 8). Figure 7 shows clearly that N_2O originates from O(^1D), exactly as iodosobenzene and in harmony with ref 56, but the spin couplings because of the CH_3Fe^+ presence generate a series of avoided crossings. On
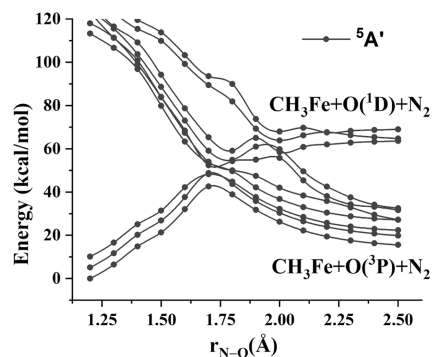

Figure 7. MRCI + Q-PEPs as a function of the N−O distance for step (2). All other parameters are kept fixed at the values of the TS2 structure obtained with MN15, except for the Fe−O distance, which is set equal to 2.8 Å.
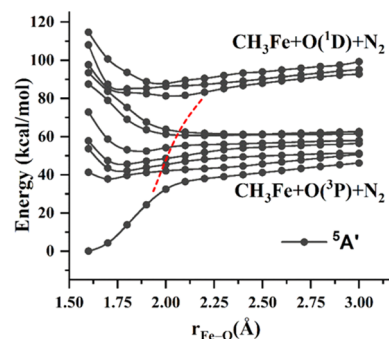

Figure 8. MRCI + Q-PEPs as a function of the Fe−O distance for step (2). All other parameters are kept fixed at the values of the TS2 structure obtained with MN15, except for the N−O distance, which is set equal to 2.4 Å.

the other hand, it is less obvious that CH_3FeO^+ stems diabatically from O(^1D) as well. Initially, the approach of CH_3Fe^+ ($^5A'$) and O (^3P) yields an attractive interaction with a constant slope up to the distance of ~2.1 Å, where the slope changes suddenly leading to the lowest minimum of Figure 8. We believe that this is because of the involvement of O (^1D) depicted with the red dashed line in Figure 8. This is also indicated by the DFT/MN15 2D-PEP, where CH_3FeO^+ goes "naturally" to the CH_3Fe^+ + O ($\sim^1D$) fragments. Conclusively, we propose a similar mechanism to that observed for the oxidation of ethene: The electron pair ($\sim 3d_\delta^2$) of the in situ $Fe^{2+}(d^6; {}^5D)$ moiety of CH_3Fe^+ is competing with an electron pair of N_2 to occupy the empty 2p-orbital of O (^1D),

$CH_3Fe^+: \rightarrow O \leftarrow :N_2$. The $3d_\delta$ orbitals are perpendicular to the Fe−CH$_3$ bond, and that explains also why C, Fe, and O atoms form an almost right angle. The remaining $2p^2$ pairs of oxygen donate only partially electronic density to available iron 3d-orbitals creating the rather ionic Fe−O bond.

The above analysis suggests that SA-CASSCF calculations are necessary to describe the TS2 region properly. Indeed, we located TS2 after averaging 10 states at the CASSCF level but asking only the first MRCI root (DZ basis set is used in this case). This TS2 is given at the SI, and the Fe−O and N−O distances are 1.903 and 1.574 Å, respectively, which are longer and shorter than DFT/MN15 by ~0.15 and ~0.05 Å, respectively. This discrepancy is in agreement with the shape of the 2D-PEPs of Figure 6. Overall, two reasons caused the convergence issues: (1) the complex shape of the energy landscape and (2) the spin dynamics due to the involvement of many states in the TS2 region making the CASSCF iterations hard to converge.

To see the effect of the clearly different geometries on the energetics, we performed MRCI(+Q) and CCSD(T) single-point calculations using the MN15/TZ and MRCI/DZ structures. Both state-averaged (SA) and state-specific (SS) CASSCF orbitals were probed. The DFT/MN15/TZ potential energy barrier is 39.0 kcal/mol, which is in perfect agreement with SA-CASSCF-MRCI + Q/TZ, SS-CASSCF-MRCI + Q/TZ, and CCSD(T)/TZ values of 40.0, 38.1, and 38.5 kcal/mol when using the DFT/MN15/TZ structure. The corresponding MRCI/TZ values are 47.0 (SA) kcal/mol and 47.6 (SS) kcal/mol. Using the MRCI/DZ geometry, the activation barrier dropped to 34.1, 34.9, and 37.0 kcal/mol at the SA-CASSCF-MRCI + Q/TZ, SS-CASSCF-MRCI + Q/TZ, and CCSD(T)/TZ levels. These values suggest a decrease of ≤5 kcal/mol for $\Delta E_e^\ddagger$ switching from the MN15 to the MRCI geometry.

Finally, we also investigated the effect of the method on ΔE_e using the DFT/MN15/TZ geometries, which should be quite accurate judging by the fairly single-reference character of R2 and P2 (see SI). The MRCI(+Q) values are −20.0 (−23.6) or (−17.0) −23.1 kcal/mol when a SA-CASSCF or SS-CASSCF is implemented. The Davidson correction brings the SA and SS results closer together. The CCSD(T)/TZ and MN15/TZ values are −23.1 and −16.7 kcal/mol, respectively. Again, the CCSD(T) energetics agree well with MRCI + Q/TZ, but MN15/TZ predicts smaller exothermicity.

Step (4): This step is competing with step (2), since and CH$_3$Fe$^+$ can, in principle, react with another C−H bond (CH$_4$ or CH$_3$OH) before being oxidized to yield insertion products. However, CH$_3$Fe$^+$ seems quite reluctant to coordinate additional units, and the addition of CH$_4$ leads to an exchange of the existing methyl group with the one of the incoming methane, instead of (CH$_3$)$_2$FeH$^+$. Figure 3 includes the related structures as R4, TS4, and P4 = R4. We also made the PEPs along the IRC for the imaginary frequency of TS4 (see Figure S3 of the SI). The inclusion of both quintet and triplet states ensures that the ground state electronic spin remains the same along the IRC.

Step (5): In this step, an iron-oxo unit (CH$_3$FeO$^+$; ^{5}A′) facilitates the conversion of methane to methanol through the radical mechanism described in the introduction. Initially, one H radical is transferred to oxygen making the intermediate I5 = CH$_3$FeOH$^+$···CH$_3$ (dots indicate weak interaction). The CH$_3$FeOH$^+$ moiety has a Fe^{3+}(d^5; ^{6}S) configuration, which couples with the ^{2}A$_2$″ of CH$_3$ to give two nearly degenerate ^{5}A′ and ^{7}A′ states. I5 is a saddle point in the ground quintet state

hyper-surface, but it is the global minimum in the septet one. The MRCI + Q PEPs along the IRC are shown in Figure 9. I5
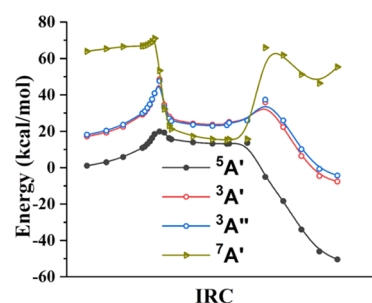

Figure 9. MRCI + Q-PEPs for several low-lying electronic states along the reaction coordinate of step (5).

finally slides to P5 without a barrier; just a slight bend of the FeOH angle allows CH$_3$ to rush toward oxygen. The PEPs of the two lowest triplets are above the quintet and cross the septet curve twice. I5 is a local minimum for the lowest triplet ^{3}A′ and ^{3}A″ states.

Step (6): Step (6) corresponds to the [2 + 2] insertion of methane to the Fe−O bond. The structures of R6, TS6, and P6 are depicted in Figure 3. Observe that the product is not (CH$_3$)$_2$FeOH$^+$, but ethane is released inherently. As in step (4), tri-coordinated complexes are not stable. Such a complex would create an in situ Fe^{4+}(d^4) center with a smaller number of "pure" iron orbitals to accommodate four unpaired electrons. Therefore, tri-coordinated complexes are expected to have a ground triplet state with an in situ Fe^{4+}(d^4; triplet) center. The lowest triplet state ^{3}P2 is 3.0 eV higher in energy.[57] Our MN15/TZ calculations confirm that the lowest state of (CH$_3$)$_2$FeOH$^+$ is triplet and lies ~4.5 eV higher than the FeOH$^+$(^{5}A′) + C$_2$H$_6$. Instead, the system prefers to eject two CH$_3$ ligands, which make ethane, and keep the quintet spin multiplicity.

The MRCI + Q/TZ PEPs along the IRC path for the lowest quintet and triplet states are given in the SI (Figure S4). It turns out that a triplet state is the lowest one in the TS6 region. Therefore, we obtained the structure of TS6 for the triplet state as well. At the MN15 level, the triplet is lower by 9.3 kcal/mol in poor agreement with the MRCI + Q value of 3.3 kcal/mol. Overall, the system starts as a quintet, changes to a triplet, and then goes back to quintet.

IV.I. Complete Catalytic Cycle. Figure 10a compares the MN15/TZ and CCSD(T)/TZ energy landscapes, and Figure 10b includes the zero-point energy (ZPE) and thermally (free energies G) corrected ones. For the latter, the CCSD(T) energetics are combined with MN15/TZ ZPE and thermal corrections. A larger version of these plots is given in the SI (Figures S5 and S6). In the case of CCSD(T)/TZ, the CCSD(T)/DZ geometries are used for all species except for TS2, R5 = R6, TS5, TS6, P5, P6, where the MN15/TZ ones are used since we were not able to locate optimal CCSD(T)/DZ structures. Additionally, the TS2 energy in both cases has been reduced by 4.4 kcal/mol to account for the multi-reference character of the system; see the discussion on step (2) above. This value is the SA-CASSCF-MRCI + Q/TZ energy difference when the MN15/TZ or the MRCI/DZ optimal geometries are used.

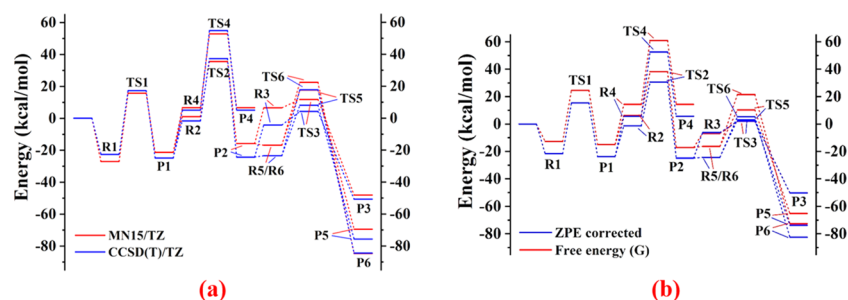The MN15/TZ and CCSD(T)/TZ energy diagrams are generally in good agreement, but there are cases with ~10

Figure 10. (a) Potential energy landscape for the complete MTM conversion catalytic cycle via steps (1)−(3). The intermediates and transition states of the competing steps (4)−(6) are also included. (b) ZPE-corrected and free-energy landscapes at the CCSD(T)/TZ//MN15/TZ level combined with MN15/TZ ZPE and thermal corrections (298 K and 1 atm).

kcal/mol discrepancies. To investigate if this is due to geometry differences or the different treatment of electron correlation, we constructed the CCSD(T)/TZ energy landscape using the MN15/TZ geometries (Figure S7 of SI), and we saw that the two plots fall on the top of each other. Therefore, the practice of optimizing the geometries at the low-cost MN15/TZ level and refining the energetics at CCSD(T)/TZ or other high ab initio level provides a perfect compromise between accuracy and efficiency.

The construction of an energy landscape at the MRCI, MRCI + Q, CASPT2 or other non-size-extensive method is trickier. Adding the energies of the observer molecules to the intermediates of each step is an erroneous task, and someone has to perform calculations where the observer molecules are present in the calculation at long distances (supermolecule approach). This increases rapidly the number of correlated electrons rendering the calculations extremely demanding. Therefore, although the MRCI(+Q) energetics are very accurate at each step, the exact energy position of the products of one step relative to the reactants of the next step requires prohibitive supermolecule calculations. This is an issue not discussed in the literature often.

Note that free energies give always less stable intermediates and higher activation barriers than zero-point-corrected energies at standard conditions of temperature and pressure (298 K and 1 atm). The reason is that the zero of the scale is set to the infinitely separated reactants (ISR) FeOCH$_3^+$ + CH$_4$, which has larger entropic terms than every other intermediate structure. Focusing on the ΔG values, the first step is exothermic with respect to both ISR and the interacting complex R1 by 24 and 2 kcal/mol, respectively. The energy barrier is less than 30 kcal/mol with respect to ISR. Steps (2) and (4) compete each other with the oxidation step providing a lower activation energy. TS2 is the highest energy structure of the cycle lying about 40 kcal/mol higher than ISR.

Finally, the products of step (2) can follow three different pathways dictated by TS3, TS5, and TS6. Recall that TS3 leads to the regeneration of the catalyst and the completion of the cycle, while TS5 and TS6 direct to unfavorable paths. Zero-point energies place TS3 only slightly lower than TS5 and TS6, as opposed to the free-energy values (298 K), which favor clearly TS3, again for entropic reasons: CH$_4$ is an observer molecule in the TS3 case and, therefore, there are two separated molecules as opposed to supermolecular the interacting complex of TS5 and TS6. Therefore, higher temperature values will favor step (3) over the unwanted steps (5) and (6). On the other hand, P5 and P6 products are significantly lower than P3, and, therefore, thermodynamics

tends to favor steps (5) and (6). From a different perspective, step (3) is a highly exothermic intramolecular transformation of the first coordination sphere of the metal. Consequently, it can happen relatively fast before any substrates approach the metal center.

To compare the CCSD(T)/DZ and MN15/TZ geometries, we calculated the minimum root-mean-square deviation (RMSD) of the two sets of structures for all species in common (see Table S1 of the SI) employing the procedure described in ref 58. In some cases, RMSD is as small as 0.02 Å (R3, TS3, P3) and in some cases is as large as 0.38 Å (P1 = P6). Generally, the larger differences are observed in electrostatically bound systems. As mentioned above, these geometry differences do not affect the energetics of the cycle. Again, locating accurate geometries is less important than describing accurately the dynamic electron correlation. Finally, CASSCF/TZ generally predicts longer bond lengths by ~0.03 Å compared to the CCSD(T)/DZ.

Overall, the investigated cycle shows some promise in developing more efficient MTM catalysts but certainly needs further optimization. More metals have to be considered, and the inclusion of ligands is indispensable to create a "hostile" environment to methanol. Homogeneous catalysis is the suggested route, since it offers great flexibility on the catalytic structure and properties.[59]

V. CONCLUSIONS

The conversion of methane to methanol catalyzed by the FeOCH$_3^+$ transition-metal methoxide was investigated by means of high-level electronic structure calculations. The goal of the present work was dual. First, we assessed the computational efficiency of different quantum chemical methodologies, and second, we explored the energy landscape of the studied catalytic cycle.

We found that a combined DFT and ab initio theoretical work provides a low computational cost, relatively fast, and quite accurate investigation. DFT/MN15/TZ- and CCSD(T)/DZ-optimized structures were used to get CCSD(T)/TZ energetics, whereas DFT/MN15/TZ frequencies were employed to evaluate ZPE and thermal corrections. MRCI + Q calculations were also invoked to construct PEPs along the reaction coordinate of each step. This work demonstrates that despite the tremendous improvement on the technical part of the existing methodologies, none of them can serve as an accurate standalone method for the study of catalytic systems as small as the present one. An important finding is that the accuracy in geometry plays a small role compared to the level of the electron correlation treatment.

From the chemical viewpoint, the employed catalytic cycle is promising, and the key steps that need further optimization are revealed. Specifically, future investigations should pay attention to (1) stabilizing further TS3 over TS5 and TS6 and at the same time destabilizing P5 and P6 over P3, (2) preventing methanol from the catalytic cycle, and (3) reducing the activation barrier of the oxidation step. This can be achieved by probing more metals, exploring the ligand effects, and using more potent oxidants. We hope that the large number of options for these three degrees of freedom will finally help us disclose a new family of MTM catalysts. Since the earth-abundant iron demonstrates good features, our near future work will focus on the effects of the ligands for this system. This work will act as a benchmark for our future theoretical work.

■ ASSOCIATED CONTENT

Ⓢ Supporting Information

The Supporting Information is available free of charge on the ACS Publications website at DOI: 10.1021/acs.jpca.9b04005.

> Cartesian coordinates and harmonic vibrational frequencies are given for the optimal geometries of all intermediate structures; Potential energy profiles are reported for steps (4), (6), and additional energy landscapes of the complete catalytic cycle are compared for different methodologies; Finally, the exact energy values for the various energy landscapes are tabulated (PDF)

■ AUTHOR INFORMATION

Corresponding Author

*E-mail: emiliord@auburn.edu.

ORCID Ⓞ

Shahriar N. Khan: 0000-0002-8913-8430

Evangelos Miliordos: 0000-0003-3471-7133

Notes

The authors declare no competing financial interest.

■ ACKNOWLEDGMENTS

■ REFERENCES

(1) Reddy, P. V. L.; Kim, K.-H.; Song, H. Emerging Green Chemical Technologies for the Conversion of CH_4 to Value Added Products. *Renewable Sustainable Energy Rev.* **2013**, 578−585.

(2) Yin, J.; Su, S.; Yu, X. X.; Weng, Y. Thermodynamic Characteristics of a Low Concentration Methane Catalytic Combustion Gas Turbine. *Appl. Energy* **2010**, 87, 2102−2108.

(3) Gesser, H. D.; Hunter, N. R.; Prakash, C. B. The Direct Conversion of Methane to Methanol by Controlled Oxidation. *Chem. Rev.* **1985**, 85, 235−244.

(4) Khokhar, M. D.; Shukla, R. S.; Jasra, R. V. Selective Oxidation of Methane by Molecular Oxygen Catalyzed by a Bridged Binuclear Ruthenium Complex at Moderate Pressures and Ambient Temperature. *J. Mol. Catal. A: Chem.* **2009**, 299, 108−116.

(5) Zakaria, Z.; Kamarudin, S. K. Direct Conversion Technologies of Methane to Methanol: An Overview. *Renewable Sustainable Energy Rev.* **2016**, 65, 250−261.

(6) da Silva, M. J. Synthesis of Methanol from Methane: Challenges and Advances on the Multi-Step (syngas) and One-Step Routes (DMTM). *Fuel Process Technol.* **2016**, 145, 42−61.

(7) Soussan, L.; Pen, N.; Belleville, M.-P.; Marcano, J. S.; Paolucci-Jeanjean, D. Alkane Biohydroxylation: Interests, Constraints and Future Developments. *J. Biotechnol.* **2016**, 222, 117−142.

(8) Ménard, G.; Hatnean, J. A.; Cowley, H. J.; Lough, A. J.; Rawson, J. M.; Stephan, D. W. C−H Bond Activation by Radical Ion Pairs Derived from R3P/Al(C6F5)3 Frustrated Lewis Pairs and N_2O. *J. Am. Chem. Soc.* **2013**, 135, 6446−6449.

(9) Ménard, G.; Stephan, D. W. C▢H Activation of Isobutylene Using Frustrated Lewis Pairs: Aluminum and Boron σ-Allyl Complexes. *Angew. Chem., Int. Ed.* **2012**, 51, 4409−4412.

(10) Ikuno, T.; Zheng, J.; Vjunov, A.; Sanchez-Sanchez, M.; Ortuño, M. A.; Pahls, D. R.; Fulton, J. L.; Camaioni, D. M.; Li, Z.; Ray, D.; et al. Methane Oxidation to Methanol Catalyzed by Cu-Oxo Clusters Stabilized in NU-1000 Metal−Organic Framework. *J. Am. Chem. Soc.* **2017**, 139, 10294−10301.

(11) Szécsényi, Á.; Li, G.; Gascon, J.; Pidko, E. A. Unraveling Reaction Networks Behind the Catalytic Oxidation of Methane with H_2O_2 Over a Mixed-Metal MIL-53(Al,Fe) MOF Catalyst. *Chem. Sci.* **2018**, 9, 6765−6773.

(12) Vitillo, J. G.; Bhan, A.; Cramer, C. J.; Lu, C. C.; Gagliardi, L. Quantum Chemical Characterization of Structural Single Fe(II) Sites in MIL-Type Metal−Organic Frameworks for the Oxidation of Methane to Methanol and Ethane to Ethanol. *ACS Catal.* **2019**, 2870−2879.

(13) Latimer, A. A.; Kakekhani, A.; Kulkarni, A. R.; Nørskov, J. K. Direct Methane to Methanol: The Selectivity−Conversion Limit and Design Strategies. *ACS Catal.* **2018**, 8, 6894−6907.

(14) Shan, J.; Li, M.; Allard, L. F.; Lee, S.; Flytzani-Stephanopoulos, M. Mild Oxidation of Methane to Methanol or Acetic acid on Supported Isolated Rhodium Catalysts. *Nature* **2017**, 551, 605.

(15) Sushkevich, V. L.; Palagin, D.; Ranocchiari, M.; van Bokhoven, J. A. Selective Anaerobic Oxidation of Methane Enables Direct Synthesis of Methanol. *Science* **2017**, 356, 523.

(16) Palkovits, R.; Antonietti, M.; Kuhn, P.; Thomas, A.; Schüth, F. Solid Catalysts for the Selective Low-Temperature Oxidation of Methane to Methanol. *Angew. Chem., Int. Ed.* **2009**, 48, 6909−6912.

(17) Muehlhofer, M.; Strassner, T.; Herrmann, W. A. New Catalyst Systems for the Catalytic Conversion of Methane into Methanol. *Angew. Chem., Int. Ed.* **2002**, 41, 1745−1747.

(18) Crabtree, R. H. Aspects of Methane Chemistry. *Chem. Rev.* **1995**, 95, 987−1007.

(19) Labinger, J. A.; Bercaw, J. E. Understanding and Exploiting C−H bond Activation. *Nature* **2002**, 417, 507.

(20) Periana, R. A.; Bhalla, G.; Tenn, W. J.; Young, K. J. H.; Liu, X. Y.; Mironov, O.; Jones, C. J.; Ziatdinov, V. R. Perspectives on Some Challenges and Approaches for Developing the Next Generation of Selective, Low Temperature, Oxidation Catalysts for Alkane Hydroxylation Based on the CH Activation Reaction. *J. Mol. Catal. A: Chem.* **2004**, 220, 7−25.

(21) Conley, B. L.; Tenn, W. J.; Young, K. J. H.; Ganesh, S. K.; Meier, S. K.; Ziatdinov, V. R.; Mironov, O.; Oxgaard, J.; Gonzales, J.; Goddard, W. A.; et al. Design and Study of Homogeneous Catalysts for the Selective, Low Temperature Oxidation of Hydrocarbons. *J. Mol. Catal. A: Chem.* **2006**, 251, 8−23.

(22) Holmen, A. Direct Conversion of Methane to Fuels and Chemicals. *Catal. Today* **2009**, 142, 2−8.

(23) Hartwig, J. F. Evolution of C−H Bond Functionalization from Methane to Methodology. *J. Am. Chem. Soc.* **2016**, 138, 2−24.

(24) Hashiguchi, B. G.; Bischof, S. M.; Konnick, M. M.; Periana, R. A. Designing Catalysts for Functionalization of Unactivated C−H Bonds Based on the CH Activation Reaction. *Acc. Chem. Res.* **2012**, 45, 885−898.

(25) Kirkland, J. K.; Khan, S. N.; Casale, B.; Miliordos, E.; Vogiatzis, K. D. Ligand Field Effects on the Ground and Excited States of Reactive FeO^{2+} Species. *Phys. Chem. Chem. Phys.* **2018**, 20, 28786−28795.

(26) Que, L. The Road to Non-Heme Oxoferryls and Beyond. *Acc. Chem. Res.* **2007**, 40, 493−500.

(27) Nam, W. High-Valent Iron(IV)−Oxo Complexes of Heme and Non-Heme Ligands in Oxygenation Reactions. *Acc. Chem. Res.* **2007**, *40*, 522−531.

(28) Nam, W. Synthetic Mononuclear Nonheme Iron−Oxygen Intermediates. *Acc. Chem. Res.* **2015**, *48*, 2415−2423.

(29) Oloo, W. N.; Que, L. Bioinspired Nonheme Iron Catalysts for C−H and C═C Bond Oxidation: Insights into the Nature of the Metal-Based Oxidants. *Acc. Chem. Res.* **2015**, *48*, 2612−2621.

(30) Khirsariya, P.; Mewada, R. K. Single Step Oxidation of Methane to Methanol−Towards Better Understanding. *Procedia Eng.* **2013**, *51*, 409−415.

(31) Donald, W. A.; McKenzie, C. J.; O'Hair, R. A. J. C-H Bond Activation of Methanol and Ethanol by a High-Spin Fe^{IV}O Biomimetic Complex. *Angew. Chem.* **2011**, *123*, 8529−8533.

(32) Carsch, K. M.; Cundari, T. R. DFT Modeling of a Methane-to-Methanol Catalytic Cycle via Group 6 Organometallics: The Role of Metal in Determining the Mode of C−H Activation. *Comput. Theor. Chem.* **2012**, *980*, 133−137.

(33) Najafian, A.; Cundari, T. R. Methane C−H Activation via 3d Metal Methoxide Complexes with Potentially Redox-Noninnocent Pincer Ligands: A Density Functional Theory Study. *Inorg. Chem.* **2017**, *56*, 12282−12290.

(34) Cunningham, E. M.; Gentleman, A. S.; Beardsmore, P. W.; Mackenzie, S. R. Infrared Spectroscopy of Closed s-Shell Gas-Phase M+(N$_2$O)$_n$ (M = Li, Al) Ion-Molecule Complexes. *Mol. Phys.* **2019**, 1−11.

(35) Marzouk, A.; Alikhani, M. E.; Madebène, B.; Tremblay, B.; Perchard, J.-P. Vibrational Spectra and Structures of Ti−N$_2$O and OTi−N$_2$: A Combined IR Matrix Isolation and Theoretical Study. *J. Phys. Chem. A* **2013**, *117*, 1697−1705.

(36) Xiao, D. J.; Bloch, E. D.; Mason, J. A.; Queen, W. L.; Hudson, M. R.; Planas, N.; Borycz, J.; Dzubak, A. L.; Verma, P.; Lee, K.; et al. Oxidation of Ethane to Ethanol by N$_2$O in a Metal−Organic Framework with Coordinatively Unsaturated Iron(II) Sites. *Nat. Chem.* **2014**, *6*, 590.

(37) Campos, J.; López-Serrano, J.; Peloso, R.; Carmona, E. Methyl Complexes of the Transition Metals. *Chem. - Eur. J.* **2016**, *22*, 6432−6457.

(38) Fiedler, A.; Schröder, D.; Schwarz, H.; Tjelta, B. L.; Armentrout, P. B. "Bare" Iron Methoxide Cation: A Simple Model To Probe the Mechanism of β-Hydrogen Transfer in Organometallic Compounds. *J. Am. Chem. Soc.* **1996**, *118*, 5047−5055.

(39) Vogiatzis, K. D.; Polynski, M. V.; Kirkland, J. K.; Townsend, J.; Hashemi, A.; Liu, C.; Pidko, E. A. Computational Approach to Molecular Catalysis by 3d Transition Metals: Challenges and Opportunities. *Chem. Rev.* **2018**, 2453−2523.

(40) Nakatani, N.; Hada, M. Can Large Active-Space CASSCF Calculation Make Sense to the Reaction Analysis of Iron Complex? A Benchmark Study of Methane Oxidation Reaction by FeO$^+$. *J. Comput. Chem.* **2019**, *40*, 414−420.

(41) Tekarli, S. M.; Drummond, M. L.; Williams, T. G.; Cundari, T. R.; Wilson, A. K. Performance of Density Functional Theory for 3d Transition Metal-Containing Complexes: Utilization of the Correlation Consistent Basis Sets. *J. Phys. Chem. A* **2009**, *113*, 8607−8614.

(42) Trogolo, D.; Arey, J. S.; Tentscher, P. R. Gas-Phase Ozone Reactions with a Structurally Diverse Set of Molecules: Barrier Heights and Reaction Energies Evaluated by Coupled Cluster and Density Functional Theory Calculations. *J. Phys. Chem. A* **2019**, *123*, 517−536.

(43) Yu, H. S.; He, X.; Li, S. L.; Truhlar, D. G. MN15: A Kohn−Sham Global-Hybrid Exchange−Correlation Density Functional with Broad Accuracy for Multi-Reference and Single-Reference Systems and Noncovalent Interactions. *Chem. Sci.* **2016**, *7*, 5032−5051.

(44) Balabanov, N. B.; Peterson, K. A. Systematically Convergent Basis Sets for Transition Metals. I. All-electron Correlation Consistent Basis Sets for the 3d Elements Sc-Zn. *J. Chem. Phys.* **2005**, *123*, No. 064107.

(45) Dunning, T. H. Gaussian-Basis Sets for Use In Correlated Molecular Calculations .1. The Atoms Boron Through Neon and Hydrogen. *J. Chem. Phys.* **1989**, *90*, 1007−1023.

(46) Kendall, R. A.; Dunning, T. H.; Harrison, R. J. Electron-Affinities of the 1st-Row Atoms Revisited - Systematic Basis-Sets and Wave-Functions. *J. Chem. Phys.* **1992**, *96*, 6796−6806.

(47) Miliordos, E.; Harrison, J. F.; Hunt, K. L. C. Ab Initio Investigation of Titanium Hydroxide Isomers and their Cations, TiOH$^{0,+}$ and HTiO$^{0,+}$. *J. Chem. Phys.* **2011**, *135*, No. 144111.

(48) Miliordos, E.; Harrison, J. F.; Hunt, K. L. C. Ground and Excited States of Vanadium Hydroxide Isomers and their Cations, VOH$^{0,+}$ and HVO$^{0,+}$. *J. Chem. Phys.* **2013**, *138*, No. 114305.

(49) Miliordos, E.; Mavridis, A. Electronic Structure of Vanadium Oxide. Neutral and Charged Species, VO$^{0,\pm}$. *J. Phys. Chem. A* **2007**, *111*, 1953−1965.

(50) Miliordos, E.; Mavridis, A. Electronic Structure and Bonding of the Early 3d-Transition Metal Diatomic Oxides and Their Ions: ScO$^{0,\pm}$, TiO$^{0,\pm}$, CrO$^{0,\pm}$, and MnO$^{0,\pm}$. *J. Phys. Chem. A* **2010**, *114*, 8536−8572.

(51) Sakellaris, C. N.; Miliordos, E.; Mavridis, A. First Principles Study of the Ground and Excited States of FeO, FeO$^+$, and FeO$^-$. *J. Chem. Phys.* **2011**, *134*, No. 234308.

(52) Jiang, W.; DeYonker, N. J.; Wilson, A. K. Multireference Character for 3d Transition-Metal-Containing Molecules. *J. Chem. Theory Comput.* **2012**, *8*, 460−468.

(53) Werner, H.-J.; Knowles, P. J.; Knizia, G.; Manby, F. R.; Schütz, M.; Celani, P.; Györffy, W.; Kats, D.; Korona, T.; Lindh, R. et al. *MOLPRO*, 2015.

(54) Frisch, M. J.; Trucks, G. W.; Schlegel, H. B.; Scuseria, G. E.; Robb, M. A.; Cheeseman, J. R.; Scalmani, G.; Barone, V.; Petersson, G. A.; Nakatsuji, H. et al. *Gaussian 16*; Gaussian, Inc.: Wallingford CT, 2016.

(55) Khan, S. N.; Miliordos, E. The Role of O(^{1}D) in the Oxidation Mechanism of Ethylene by Iodosobenzene and Other Hypervalent Molecules. *Phys. Chem. Chem. Phys.* **2017**, *19*, 18152−18155.

(56) Kalemos, A.; Ariyarathna, I. R.; Khan, S. N.; Miliordos, E.; Mavridis, A. "Hypervalency" and the Chemical Bond. *Comput. Theor. Chem.* **2019**, *1153*, 65−74.

(57) Kramida, A.; Ralchenko, Y.; Reader, J. *NIST Atomic Spectra Database (version 5.6.1)*; National Institute of Standards and Technology: Gaithersburg, MD. https://physics.nist.gov/asd, 2018.

(58) Coutsias, E. A.; Seok, C.; Dill, K. A. Using Quaternions to Calculate RMSD. *J. Comput. Chem.* **2004**, *25*, 1849−1857.

(59) Cornils, B.; Herrmann, W. A. Concepts in Homogeneous Catalysis: The Industrial View. *J. Catal.* **2003**, *216*, 23−31.